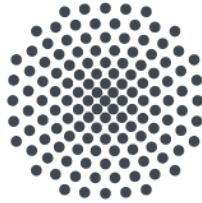


JULIAN KARST

**FUNCTIONAL & ACTIVE  
PLASMONIC SYSTEMS AND METASURFACES**





## Functional & Active Plasmonic Systems and Metasurfaces

Von der Fakultät Mathematik und Physik der Universität Stuttgart  
zur Erlangung der Würde eines Doktors der  
Naturwissenschaften (Dr. rer. nat.) genehmigte Abhandlung

vorgelegt von

**Julian Karst**

aus Stuttgart

Hauptberichter: Prof. Dr. Harald Giessen  
Mitberichterin: Prof. Dr. Laura Na Liu  
Externer Mitberichter: Prof. Dr. Thomas Zentgraf  
Prüfungsvorsitzende: Prof. Dr. Maria Daghofer

Tag der mündlichen Prüfung: 28.09.2022

4. Physikalisches Institut der Universität Stuttgart  
2022



## ABSTRACT

---

Functional and active plasmonic nanostructures and metasurfaces are at the heart of emerging and novel optical technologies as they allow to confine and actively manipulate light on very small length scales. Ultimately, they will contribute to the miniaturization of existing and novel optical devices necessary in a great variety of different fields. They include but are not limited to new display and projection technologies for augmented and virtual reality, dynamic 3D holography devices, miniaturized LiDAR (Light Detection and Ranging) approaches, or ultra-sensitive nanooptical sensing devices for explosive and toxic gases or (chiral) chemical substances. Overall, this thesis introduces and gives an in-depth analysis of novel approaches for such functional and active plasmonic systems and metasurfaces.

Firstly, we establish metallic polymers in the field of active plasmonics. Such polymers are well known since the 1980s, yet, have mostly been used and optimized for transparent conducting electrodes. We show that nanostructuring such polymers into nanoantennas allows to electrically switch their plasmonic properties ON or OFF. This concept is based on an electrically-driven metal-to-insulator transition of the polymer which is triggered by CMOS compatible voltages of only  $\pm 1$  V. The switching frequencies reach 33 Hz, which makes the polymer nanoantennas usable in future display technologies. Additionally, we find a long-term stability over several hundred switching cycles. As applications, we use the metallic polymer nanoantennas for high-contrast metasurfaces. We demonstrate active beam steering with 100% contrast ratio in transmission. Furthermore, the nanoantennas are used for novel metalenses-on-demand. We realize an entire non-volatile metaobjective from metallic polymer metasurfaces with unique functionalities including a state with two foci.

Besides an applied voltage, the optical properties of plasmonic nanoantennas can also be altered, e.g., with gases. We will investigate active plasmonic systems based on hydrogen-sensitive metals, as they find applications in active metasurfaces as well as plasmonic hydrogen sensing. Frequently-used materials over the last years are, e.g., palladium, yttrium, or magnesium. Here, magnesium is the most promising for active optical applications. On the one hand, the reason lies with its comparably large hydrogen storage capacity. On the other hand, the optical properties of magnesium nanoantennas can be changed significantly upon hydrogen exposure. However, the hydrogenation of magnesium nanoantennas typically takes place on very long time-

scales with a comparably high material degradation. Thus, we use scattering-type scanning near-field optical microscopy (sSNOM) to watch and examine the hydrogen diffusion mechanism in magnesium on the nanometer scale. We find the hydrogen diffusion is strongly influenced by the intrinsic poly-crystalline structure and volume expansion of magnesium. What is more, we demonstrate that not only hydrogen gas but also liquid alcohol can hydrogenate hydrogen-sensitive metals, which provides a new possibility to alter the optical properties of plasmonic nanoantennas. We actively control the plasmonic resonances of yttrium nanoantennas by immersing them in an alcohol bath. By doing so, the nanoantennas are used as local nanooptical indicators to optically visualize this alcohol deprotonation process.

Furthermore, in many different fields, it is important to sense the chirality or handedness of chemical substances. Chirality is one of the most prominent principles in nature and can determine, *e.g.*, whether a drug acts as intended or becomes toxic to the human body. Apart from distinct molecular interactions between handed molecules, chirality can also manifest itself optically and can be measured with sophisticated optical sensing schemes. Here, plasmonic nanoparticles can contribute to significantly decrease the sensing volumes and consequently boost the achievable sensitivity. Thus, we finally analyze the optical responses of single chiral plasmonic nanoparticles with an automated chiral scatterometry technique. We show that their chiroptical responses are greatly influenced by and correlate with the particle morphology. The investigated chiral helicoids show tremendous optical activity on the single particle level. Consequently, they can show great potential for functional chiral sensing platforms, as they will allow to push the sensitivity of nanooptical chiral sensors to entirely new dimensions. In combination with the switchable plasmonic materials, even actively controllable chiral sensors become feasible.

## ZUSAMMENFASSUNG

---

Funktionelle und aktive plasmonische Nanostrukturen und Metaoberflächen sind das Herzstück von einer Vielzahl an neuartigen optischen Technologien. Sie ermöglichen es Licht auf sehr kleinen Längenskalen zu bündeln und aktiv zu manipulieren. Insbesondere werden sie zur Miniaturisierung von elektro-optischen Bauteilen beitragen, welche für die Realisierung von zukunftsweisenden Technologien in verschiedensten Bereichen vonnöten sind. Hierzu zählen unter anderem Technologien aus den Bereichen virtuelle Realität (VR: *engl.*: virtual reality) und erweiterte Realität (AR: *engl.*: augmented reality), dynamische drei-dimensionale Holografie, miniaturisiertes LiDAR (*engl.*: Light Detection and Ranging), sowie nano-optische Sensoren für explosive und giftige Gase oder für (händige) chemische Substanzen.

Die vorliegende Arbeit befasst sich mit mehreren Ansätzen für funktionelle und aktive plasmonische Systeme und Metaoberflächen. Hierbei analysieren wir insbesondere deren Funktionalitäten als auch die zugrundeliegenden Schaltmechanismen. Wir führen zunächst metallische Polymere für schaltbare plasmonische Systeme ein. Diese Polymere sind zwar seit den 1980er Jahren bekannt, wurden jedoch hauptsächlich für transparente und leitfähige Elektroden verwendet sowie optimiert. Wir zeigen, dass die Nanostrukturierung solcher Polymere es ermöglicht, Nanoantennen mit elektrisch schaltbaren optischen Eigenschaften herzustellen. Deren plasmonische Resonanzen lassen sich hierbei elektrisch ein- oder ausschalten. Unser Konzept basiert auf einem elektrisch-schaltbaren Metall-zu-Isolator-Übergang des Polymers, der durch CMOS-kompatible Spannungen von lediglich  $\pm 1$  V kontrolliert werden kann. Schaltzeiten erreichen Displayfrequenzen von 33 Hz, was es unseren Nanoantennen ermöglicht, Anwendung in zukünftigen Display-Technologien zu finden. Zudem demonstrieren wir Langzeit-Stabilität über mehrere Hundert Zyklen. Durch gezielte periodische Anordnung unserer metallischen Polymer-Nanoantennen erschaffen wir ultra-dünne Metaoberflächen zur aktiven Laserstrahlableitung sowie zur aktiv-steuerbaren Lichtfokussierung mit sehr hohem Kontrast. Wir realisieren zudem ein Metaobjektiv aus metallischem Polymer, welches neuartige Funktionalitäten, wie z.B. einen bifokalen Zustand, aufweist.

Als Nächstes untersuchen wir aktive plasmonische Systeme auf Basis von wasserstoffsensitiven Metallen. Solche schaltbaren plasmonischen Antennen finden Anwendung in aktiven Metaoberflächen sowie in plasmonischen Wasserstoffsensoren. Häufig

verwendete Materialien sind hierbei Palladium, Yttrium, oder Magnesium. Letzteres bietet hierbei den Vorteil, dass es ein exzellenter Wasserstoffspeicher ist. Zudem können die optischen Eigenschaften von plasmonischen Nanoantennen aus Magnesium mit Hilfe von Wasserstoff sehr stark beeinflusst werden. Jedoch sind die damit einhergehenden Schaltzeiten häufig sehr lang und die Degradierung von Magnesium während der Schaltvorgänge sehr hoch. Um die hierbei limitierenden Faktoren herauszufinden, vermessen wir Magnesium während der Hydrogenisierung mittels auf Streuung basierender optischer Rasternahfeldmikroskopie. Hiermit können wir die Wasserstoff-Diffusionsprozesse in Magnesium auf der Nanometer-Skala detailliert untersuchen. Es lässt sich dabei feststellen, dass diese Diffusionsprozesse stark von der polykristallinen Morphologie von Magnesium sowie durch dessen Volumenausdehnung beeinflusst werden. Darüber hinaus zeigen wir, dass nicht nur Wasserstoff in Form von Gas, sondern auch Alkohole in der Lage sind Metalle zu hydrogenisieren. Am Beispiel von Yttrium demonstrieren wir, dass sich die optischen Eigenschaften von plasmonischen Nanoantennen durch deren Eintauchen in Alkohol verändern lassen. Dabei fungieren die Nanoantennen als lokale nanooptische Indikatoren, um diesen flüssigen Hydrogenisierungsprozess optisch zu visualisieren.

In verschiedensten Bereichen ist es zudem nötig die optische Aktivität/Chiralität bzw. Händigkeit einer chemischen Substanz zu ermitteln. So entscheidet, z.B., die Händigkeit einer Substanz darüber, ob sie als Medikament eingesetzt werden kann oder giftig für den menschlichen Körper ist. Diese Chiralität kann optisch detektiert und gemessen werden. Hierbei können plasmonische Nanoantennen die Sensitivität entscheidend verbessern. Deshalb analysieren wir zuletzt die spektrale Antwort einzelner chiraler Nanopartikel. Hierzu verwenden wir unsere automatisierte Messmethode, mit welcher sich die chiralen Streuspektren der Einzelpartikel detailliert untersuchen lassen. Dabei zeigen wir, dass die chiralen Einzelpartikelspektren stark von der jeweiligen Morphologie des Partikels abhängen. Unsere untersuchten Partikel weisen im Allgemeinen eine spiralförmige Struktur auf, welche zu einer enormen optischen Aktivität führt. Folglich können diese chiralen plasmonischen Nanopartikel in verschiedensten Sensorplattformen vielversprechende Anwendungen finden. Unter anderem könnte mit deren Verwendung die Sensitivität bzw. Empfindlichkeit von nanooptischen Sensoren für chirale Moleküle bzw. Flüssigkeiten enorm gesteigert werden. In Kombination mit schaltbaren plasmonischen Materialien rücken sogar aktiv steuerbare chirale Sensoren in greifbare Nähe.



## PUBLICATIONS

---

### FULL LIST OF PUBLICATIONS

*In scientific journals (first author):*

1. **J. Karst**, N. Strohfeldt, M. Schäferling, H. Giessen, and M. Hentschel  
*Single Plasmonic Oligomer Chiral Spectroscopy*  
Advanced Optical Materials **6**, 1800087 (2018).
2. **J. Karst**, N. H. Cho, H. Kim, H.-E. Lee, K. T. Nam, H. Giessen, and M. Hentschel  
*Chiral Scatterometry on Chemically Synthesized Single Plasmonic Nanoparticles*  
ACS Nano **13**, 8659 (2019).  
This publication was selected as Editor's Pick, highlighted with an "In Nano" write-up.
3. **J. Karst**, M. Hentschel, F. Sterl, H. Linnenbank, M. Ubl, and H. Giessen  
*Optimizing Magnesium Thin Films for Optical Switching Applications: Rules and Recipes*  
Optical Materials Express **5**, 1346 (2020).
4. **J. Karst**, F. Sterl, H. Linnenbank, T. Weiss, M. Hentschel, and H. Giessen  
*Watching In-Situ the Hydrogen Diffusion Dynamics in Magnesium on the Nanoscale*  
Science Advances **6**, eaaz0566 (2020).
5. **J. Karst**, M. Hentschel, F. Sterl, and H. Giessen  
*Liquid Hydrogenation of Plasmonic Nanoantennas via Alcohol Deprotonation*  
ACS Photonics **8**, 1810 (2021).  
This publication was featured on the cover of the issue June 2021 of ACS Photonics.
6. **J. Karst**, M. Floess, M. Ubl, C. Dingler, C. Malacrida, T. Steinle, S. Ludwigs, M. Hentschel, and H. Giessen  
*Electrically Switchable Metallic Polymer Nanoantennas*  
Science **374**, 612 (2021).
7. **J. Karst**, Y. Lee, M. Floess, M. Ubl, S. Ludwigs, M. Hentschel, and H. Giessen  
*Electro-Active Metaobjective from Metalenses-On-Demand*  
Nature Communications, accepted (2022).

8. D. De Jong\*, **J. Karst\***, M. Hentschel, D. Ludescher, M. Floess, K. Dirnberger, P. Braun, S. Ludwigs, and H. Giessen  
*All Solid-State Electrically Switchable Metasurface Device*  
in preparation (2022).  
\*These authors contributed equally.

*In scientific journals (co-author):*

9. V. Drechsler, J. Krauth, **J. Karst**, H. Giessen, and M. Hentschel  
*Switchable Optical Nonlinearity at the Metal to Insulator Transition in Magnesium Thin Films*  
ACS Photonics **7**, 1560 (2020).
10. M. Hentschel, **J. Karst**, and H. Giessen  
*Tailored optical functionality by combining electron-beam and focused gold-ion beam lithography for solid and inverse coupled plasmonic nanostructures*  
Advanced Optical Materials **8**, 2000879 (2020).
11. J. Ratzsch, **J. Karst**, J. Fu, M. Ubl, T. Pohl, F. Sterl, C. Malacrida, M. Wieland, B. Reineke, T. Zentgraf, S. Ludwigs, M. Hentschel, and H. Giessen  
*Electrically switchable metasurface for beam steering using PEDOT polymers*  
Journal of Optics **22**, 124001 (2020).  
Special issue on switchable metasurfaces.
12. E.H. Waller, **J. Karst**, and G. von Freymann  
*Photosensitive Material Enabling Direct Fabrication of Filigree 3D Silver Microstructures via Laser-Induced Photoreduction*  
Light: Advanced Manufacturing **2**, 1 (2021).
13. D. Pfezer, **J. Karst**, M. Hentschel, and H. Giessen  
*Predicting Concentrations of Mixed Sugar Solutions with a Combination of Resonant Plasmon-Enhanced SEIRA and Principal Component Analysis*  
Sensors **22**, 5567 (2022).
14. M. Hentschel, K. Koshelev, F. Sterl, S. Both, **J. Karst**, T. Weiss, Y. Kivshar, and H. Giessen  
*Dielectric Mie Voids: Confining Light to Air*  
Light: Science & Applications, accepted (2022).

15. Y. Lee, **J. Karst**, M. Ubl, P. Flad, M. Hentschel, and H. Giessen  
*Ultracompact LiDAR Platform using Electrically Switchable Metallic Polymer Nanogratings*  
in preparation (2022).

*Patents:*

16. **J. Karst**, M. Hentschel, and H. Giessen (BW-Stiftung)  
Applied for international patent (PCT): PCT/EP2021/069202

*Book chapters:*

17. **J. Karst**, M. Hentschel, N. H. Cho, H. Kim, K. T. Nam, and H. Giessen  
*Plasmonic Materials and Metastructures: Fundamentals, Current Status, and Perspectives*  
Chapter: Chiral Plasmonics  
Edited by S. Gwo, A. Alù, Y.-J. Lu, X. Li, and C.-K. Shih  
Elsevier, expected publication date: 2023

*Own contributions:*

1. **J. Karst**, N. Strohfeltd, M. Hentschel, H. Giessen, and N. Liu  
*Circular Dichroism Spectroscopy on Individual Plasmonic Nanoparticles*  
Conference Talk, DPG Spring Meeting 2016  
Regensburg (Germany)
2. **J. Karst**, M. Hentschel, N. Strohfeltd, M. Schäferling, and H. Giessen  
*Circular Dichroism Spectroscopy on Individual Plasmonic Nanoparticles*  
Invited Talk, Workshop on Chiral Sensing EU COST MP1302, November 2017  
Stuttgart (Germany)
3. **J. Karst**, M. Hentschel, N. Strohfeltd, M. Schäferling, and H. Giessen  
*Single Plasmonic Oligomer Chiral Spectroscopy*  
Conference Talk, DPG Spring Meeting 2018  
Berlin (Germany)
4. **J. Karst**, N. Strohfeltd, M. Schäferling, H. Giessen, and M. Hentschel  
*Single Plasmonic Oligomer Chiral Spectroscopy*  
Invited Talk, Gordon Research Seminar on Plasmonics and Nanophotonics 2018  
Newry, ME (USA)
5. **J. Karst**, N. Strohfeltd, M. Schäferling, H. Giessen, and M. Hentschel  
*Single Plasmonic Oligomer Chiral Spectroscopy*  
Poster Presentation, Gordon Research Seminar on Plasmonics and Nanophotonics 2018  
Newry, ME (USA)
6. **J. Karst**, F. Sterl, H. Linnenbank, M. Hentschel and H. Giessen  
*Magnesium Thin Film Nanoscale Hydrogenography*  
Poster Presentation, Gordon Research Conference on Plasmonics and Nanophotonics 2018  
Newry, ME (USA)
7. **J. Karst**, N. Strohfeltd, M. Schäferling, H. Giessen, and M. Hentschel  
*Single Plasmonic Oligomer Chiral Spectroscopy*  
Colloquium Talk, Seminar of Prof. Dr. David Norris, ETH Zuerich, October 2018  
Zurich (Switzerland)

8. **J. Karst** and H. Giessen  
*Discussion on "Chiral Sensing"*  
Invited Talk, NanoMeta 2019  
Seefeld (Austria)
9. **J. Karst**, F. Sterl, H. Linnenbank, M. Hentschel and H. Giessen  
*In-Situ Magnesium Thin Film Nanoscale Hydrogenography*  
Conference Talk, NanoMeta 2019  
Seefeld (Austria)
10. **J. Karst**, F. Sterl, H. Linnenbank, M. Hentschel and H. Giessen  
*In-Situ Magnesium Thin Film Nanoscale Hydrogenography*  
Conference Talk, DPG Spring Meeting 2019  
Regensburg (Germany)
11. **J. Karst**, F. Sterl, H. Linnenbank, M. Hentschel, and H. Giessen  
*Watching In-Situ the Hydrogen Diffusion Dynamics in Magnesium on the Nanoscale*  
Invited Talk, Nanoscale Analytics Workshop 2019, neaspec GmbH  
Munich (Germany)  
Appeared as lecture in neaWEBINARs of neaspec GmbH on June 24, 2019  
<https://www.neaspec.com/education/webinars/>
12. **J. Karst** and H. Giessen  
*Chiral Spectroscopy of 3D Plasmonic Nanostructures*  
Invited Talk, 17th International Conference on Chiroptical Spectroscopy 2019  
Pisa (Italy)
13. **J. Karst**, N. Strohfeldt, M. Schäferling, N. H. Cho, H. Kim, H.-E. Lee, K. T. Nam,  
H. Giessen, and M. Hentschel  
*Chiral Scatterometry on Individual Plasmonic Nanoparticles*  
Invited Talk, Workshop on Nanoscale Optical Activity 2019  
Pisa (Italy)
14. **J. Karst**, F. Sterl, H. Linnenbank, M. Hentschel and H. Giessen  
*Watching In-Situ the Hydrogen Diffusion Dynamics in Magnesium on the Nanoscale*  
Talk, Gordon Research Seminar on Hydrogen-Metal Systems 2019  
Castelldefels (Spain)
15. **J. Karst**, F. Sterl, H. Linnenbank, M. Hentschel, and H. Giessen  
*Nanoscale Hydrogenography Using the Optical Near-Field*

Invited Talk, Gordon Research Conference on Hydrogen-Metal Systems 2019  
Castelldefels (Spain)

16. **J. Karst**, N. H. Cho, H. Kim, H.-E. Lee, K. T. Nam, H. Giessen, and M. Hentschel  
*Chiral Scatterometry on Chemically Synthesized Single Plasmonic Nanoparticles*  
Conference Talk, DPG Spring Meeting 2020  
Dresden (Germany)
17. **J. Karst**, S. Maier, O. Mitrofanov, P. Klarskov Pedersen, and H. Giessen  
*Panel Discussion: Infrared Nano-Optics*  
Mini-Symposium, DPG Spring Meeting 2021  
Dresden (Germany)
18. **J. Karst**, J. Ratzsch, J. Fu, M. Ubl, T. Pohl, F. Sterl, C. Malacrida, M. Wieland, B. Reineke, T. Zentgraf, S. Ludwigs, M. Hentschel, and H. Giessen  
*Electrically Switchable Metasurface for Beam Steering Using PEDOT Polymers*  
Conference Talk, CLEO 2021 (Online)  
San Jose (USA)
19. **J. Karst**, F. Sterl, H. Linnenbank, T. Weiss, M. Hentschel, and H. Giessen  
*Watching In Situ the Hydrogen Diffusion Dynamics in Magnesium on the Nanoscale*  
Conference Talk, CLEO 2021 (Online)  
San Jose (USA)
20. **J. Karst**, M. Floess, M. Ubl, C. Dingler, C. Malacrida, T. Steinle, S. Ludwigs, M. Hentschel, and H. Giessen  
*Electrically Switchable Metallic Polymer Nanoantennas and Metasurfaces*  
Breakthrough Talk, NanoMeta 2022  
Seefeld (Austria)
21. **J. Karst**, M. Hentschel, and H. Giessen  
*Electrically switchable plasmonic nanoantennas: Active metasurfaces for beam steering and metalensing*  
Invited Talk, SPIE Photonics West 2022  
San Francisco (USA)

*Other contributions:*

22. •V. Drechsler, J. Krauth, M. Hentschel, **J. Karst**, and H. Giessen  
*Wavelength-dependent Third Harmonic Generation in Metallic Thin Films*  
Conference Talk, DPG Spring Meeting 2019  
Regensburg (Germany)
23. •H. Giessen, H. Linnenbank, F. Sterl, and **J. Karst**  
*Local dynamics of switching plasmonic systems on the nanometer scale*  
Invited Talk, DINAMO 2019  
Galápagos (Ecuador)
24. •V. Drechsler, J. Krauth, M. Hentschel, **J. Karst**, H. Linnenbank, and H. Giessen  
*Third Harmonic Generation in Magnesium near the Metal-to-Insulator Phase Transition*  
Invited Talk, ICMAT 2019  
Singapore
25. **J. Karst**, N. H. Cho, H. Kim, H.-E. Lee, K. T. Nam, J. Krauth, T. Schumacher, J. Defrance, B. Metzger, M. Lippitz, T. Weiss, H. Giessen, and •M. Hentschel  
*Chirality and Nonlinearities in Bottom-Up and Top-Down Plasmonic Nanostructures: The Influence of Asymmetries*  
Invited Talk, Sino-German Symposium on Nanophotonics and Optoelectronics Integration 2019  
Changsa (China)
26. •H. Giessen, **J. Karst**, H. Linnenbank, F. Sterl, and M. Hentschel  
*In-Situ Thin Film Nanoscale Hydrogenography in Magnesium Plasmonics*  
Keynote, METANANO 2019  
St. Petersburg (Russia)
27. V. Drechsler, J. Krauth, **J. Karst**, M. Hentschel, and •H. Giessen  
*Third Harmonic Generation in Magnesium Near the Metal-to-Insulator Phase Transition*  
Invited Talk, Symposium on the topic of Emerging Material Platforms and Approaches for Plasmonics 2019  
Boston (USA)
28. •H. Giessen, **J. Karst**, F. Sterl, H. Linnenbank, and M. Hentschel  
*In-Situ Thin Film Nanoscale Hydrogenography in Magnesium Plasmonics*

Conference Talk, DPG Spring Meeting 2021  
Online

29. D. Pfezer, **J. Karst**, L. Kühner, M. Hentschel, and ●H. Giessen  
*SEIRA Sensing of Different Sugars at Physiological Concentrations*  
Conference Talk, CLEO 2021 (Online)  
San Jose (USA)
  30. ●H. Giessen, **J. Karst**, and M. Hentschel  
*Electrically Switchable Plasmonic Nanoantennas - Active Metasurfaces for Beam Steering and Metalensing*  
Invited Talk, MRS Fall 2021  
Boston (USA)
  31. ●H. Giessen, M. Hentschel, and **J. Karst**  
*Electrically switchable plasmonic nanoantennas: active metasurfaces for metalensing*  
Invited Talk, SPIE Photonics West 2022  
San Francisco (USA)
  32. ●Y. Lee, **J. Karst**, M. Ubl, P. Flad, M. Hentschel, and H. Giessen  
*Ultracompact LiDAR Platform using Electrically Switchable Metallic Polymer Nanogratings*  
Talk, NanoMeta 2022  
Seefeld (Austria)
  33. ●M. Hentschel, K. Koshelev, F. Sterl, S. Both, **J. Karst**, T. Weiss, Y. Kivshar, and H. Giessen  
*Dielectric Mie Voids: Confining Light in Air*  
Talk, NanoMeta 2022  
Seefeld (Austria)
  34. ●H. Giessen, **J. Karst**, and M. Hentschel  
*Electrically switchable metallic polymer nanoantennas, metasurfaces, and metalenses*  
Talk, SPIE Optics & Photonics Symposium 2022  
San Diego (USA)
- Presenting author



# CONTENTS

---

ABSTRACT	v
ZUSAMMENFASSUNG	vii
PUBLICATIONS	ix
1 INTRODUCTION	1
2 ELECTRO-ACTIVE METALLIC POLYMER NANOANTENNAS AND METASURFACES	5
2.1 Introduction	5
2.2 Theoretical Background	7
2.2.1 MAXWELL's Equations	7
2.2.2 DRUDE Model	9
2.2.3 LORENTZ Model	12
2.2.4 Localized Surface Plasmons	13
2.2.5 Metallic Polymers	17
2.3 Instrumentation	19
2.3.1 Fabrication Routine	19
2.3.2 Electrochemical Setup	20
2.4 Electrically Switchable Metallic Polymer Nanoantennas	21
2.4.1 Concept	21
2.4.2 Resonance Tuning	23
2.4.3 Electrical Switching of Plasmonic Resonances	25
2.4.4 Switching Speed	29
2.5 Metallic Polymer Metasurface for Dynamic Beam Steering	32
2.6 Electro-Active Metaobjective from Metalenses-On-Demand	38
2.6.1 Concept	38
2.6.2 Static Metallic Polymer Metalens	40
2.6.3 Metalens-On-Demand	44
2.6.4 Electro-Active Metaobjective	46
2.7 Conclusions & Outlook	49
3 HYROGEN-SENSITIVE METALS FOR ACTIVE PLASMONICS	51
3.1 Introduction	51

3.2	Theoretical Background . . . . .	53
3.2.1	sSNOM Working Principle . . . . .	53
3.2.2	Finite Dipole Model . . . . .	54
3.2.3	Pseudoheterodyne Detection . . . . .	59
3.2.4	Magnesium and Hydrogen . . . . .	61
3.3	Watching Hydrogen Diffusion in Magnesium . . . . .	66
3.3.1	Concept & Measurement Technique . . . . .	67
3.3.2	Near-Field Appearance of Phase Transition . . . . .	70
3.3.3	Time-Resolved Hydrogen Diffusion . . . . .	77
3.3.4	Vertical Expansion . . . . .	82
3.4	Liquid Hydrogenation of Yttrium Nanoantennas . . . . .	90
3.4.1	Concept . . . . .	91
3.4.2	Material Investigation via Thin Films . . . . .	92
3.4.3	Temporal Investigation via Thin Films . . . . .	96
3.4.4	Nanooptical Indicator for Deprotonation . . . . .	97
3.5	Conclusions & Outlook . . . . .	102
4	SINGLE CHIRAL PLASMONICS . . . . .	105
4.1	Introduction . . . . .	105
4.2	Instrumentation: Chiral Scatterometry . . . . .	108
4.3	Chiral Scatterometry on Single Helicoid Nanoparticles . . . . .	111
4.3.1	Single Helicoid Nanoparticles . . . . .	111
4.3.2	Scattering and Differential Scattering . . . . .	113
4.3.3	Single vs. Ensemble . . . . .	118
4.3.4	Correlation with Morphology . . . . .	121
4.3.5	Evolution of Chirality . . . . .	124
4.4	Conclusions & Outlook . . . . .	128
	SYMBOLS . . . . .	131
	ACRONYMS . . . . .	133
	LIST OF FIGURES . . . . .	135
	BIBLIOGRAPHY . . . . .	139

## INTRODUCTION

---

Structuring metallic materials to sizes below the wavelength of the impinging electromagnetic wave will give rise to unique optical phenomena. In these so-called plasmonic nanoparticles/-structures the quasi-free conduction electrons will start to oscillate collectively resulting in very strong local electric fields in the vicinity of these nanoparticles (so-called "hot spots"). By changing their size, distance, material, or surrounding material, one can control their resonance frequency and thus the amount, efficiency, wavelength etc. of light being absorbed and re-emitted by the particles. This means that one can tailor specific optical properties necessary for a desired application.

Consequently, the plasmonic nanoparticles have gained significant interest in several different fields of research over the last couple of years. First studies on plasmonic nanoparticles were introduced for particles made from noble metals such as gold. These nanoparticles possess static optical properties, i.e., their plasmonic resonances are fixed at a specific wavelength/frequency. By exploiting their hot spots, one can for example detect molecular species in liquid mixtures. In addition, the nanoparticles can be even made highly sensitive to circularly polarized light and thus to chiral substances by, e.g., imprinting chiral features in the particle morphology. In that sense, researchers all over the world are on the quest to find chiral nanoparticles or arrangements with the highest optical chirality and thus optical asymmetry. Proposed are ultra-small sensing volumes and thus ultra-high sensitivities for chemical (chiral) molecules and substances.

Additionally, by controlling the relative orientation, angle, height, etc. of the sub-wavelength nanoparticles in a periodic arrangement, so called metasurfaces with unique optical properties and functionalities can be created. The applications of these artificial sheet "materials" range from metasurfaces for lensing, sensing, beam steering, ultra-thin waveplates all the way to metasurfaces for future 3D holography displays. Via the individual geometrical nanoantenna arrangement, any arbitrary phase profile and thus functionality of the metasurface can be achieved. Most importantly, metasurfaces will allow to further miniaturize such optical systems as it is inevitable to realize, e.g., emerging and future displaying technologies where ultra-small pixel sizes are

necessary. Furthermore, the technologies will benefit from a dynamic spatiotemporal control of the nanoantenna material. This means that the functionality of metasurfaces can be actively controlled by an external stimulus. Consequently, significant research is devoted to finding sophisticated switching mechanisms to dynamically change the optical properties of plasmonic nanoparticles. Among others, such stimuli can be gases, chemicals, temperature, or an applied voltage, with the latter being the most suitable for electro-optical devices.

There are mainly two possibilities to realize such active plasmonic nanoparticles or metasurfaces. Firstly, indirect approaches use static plasmonic nanoparticles, typically fabricated from, e.g., gold or aluminum. Hereby, the only possibility to tune the resonance frequency is, e.g., by changing the refractive index of the surrounding material. Secondly, tremendous efforts have been undertaken to not only change the surrounding but rather directly switch the plasmonic nanoparticle material itself. Typically, this approach utilizes materials with metal-to-insulator transitions to switch between a plasmonic metallic state and an insulating state of the nanoparticles. A widely used material is magnesium (Mg), as this allows to reversibly switch the plasmonic resonances of nanoparticles via a hydrogen exposure. However, the metal-to-insulator transition in Mg is typically very slow and comes with strong degradation of the material.

The work presented in this thesis will mainly tackle three different topics. First, we demonstrate directly and electrically switchable plasmonic nanoparticles. Instead of using noble metals, we use a metallic polymer with an electrically-driven metal-to-insulator transition allowing for high-contrast active plasmonics and metasurfaces. We will demonstrate several superior properties of our metallic polymer nanoantennas in comparison to previous approaches. This includes high switching speeds at display frequencies, long-term stability, high switching contrasts, CMOS compatible switching voltages of only  $\pm 1$  V, as well as operation in transmission. Applications of dynamic beam steering and metalenses-on-demand are demonstrated. Second, we investigate hydrogen-sensitive plasmonic systems, e.g., made from Mg or yttrium (Y). We give detailed insights into the exact switching mechanism of magnesium upon hydrogen-exposure. We find that the nanoscale crystallinity and morphology limits the diffusion time and causes very slow transition times. Furthermore, we propose an alternative switching scheme based on a liquid hydrogenation with alcohols. Last, we shift towards non-ensemble investigations of single particle chirality. We investigate static highly asymmetric chiral nanoparticles and use chiral scatterometry to analyze the optical activity of these helicoid gold nanoparticles on the single particle level. As

mentioned above, this will, e.g., aid the improvement of the sensitivity of (chiral) optical plasmonic sensors.

#### THESIS OUTLINE

The thesis is structured into three main chapters covering the topics mentioned above. Due to the rather different nature, each chapter will feature its own INTRODUCTION, CONCLUSIONS & OUTLOOK, and, where ever needed, specific THEORETICAL BACKGROUND. The outline is as follows:

- Chapter 2 will introduce the concept of using metallic polymers for electrically switchable plasmonic nanoantennas and metasurfaces. The theoretical background on general optical properties of metals and dielectrics will be introduced as well as theory on localized surface plasmons and optical properties of metallic polymers. The chapter continues with an experimental part on the fabrication technique of metallic polymer nanoantennas and the electrochemical setup. This is followed by a detailed analysis and experimental investigation of the electrically switchable metallic polymer nanoantennas. It includes the overall concept, the optical resonance tuning, as well as the investigation of switching contrast and switching speed. It is shown that the plasmonic resonance of these nanoantennas can be switched entirely OFF and back ON at display frequencies. Subsequently, the metallic polymers will be structured into metasurfaces for electro-active beam steering and into metalenses-on-demand. This concept of metalenses which can be turned ON and OFF *on demand* is used to demonstrate an entire metaobjective. A detailed analysis of the achieved optical states is given including a novel state with two foci.
- Chapter 3 is based on hydrogen-sensitive metals and will tackle the in-depth understanding of the hydrogen diffusion in magnesium as well as the liquid hydrogenation of yttrium. We will first discuss the theoretical background of scattering-type scanning nearfield optical microscopy (sSNOM) as well as phonon vibrations and optical properties in magnesium. This is followed by a section where we experimentally watch the hydrogen diffusion in magnesium on the nanoscale. We use in-situ sSNOM as a measurement technique and will answer the question what is limiting the rather slow hydrogen-triggered metal-to-insulator transition from Mg to magnesium hydride ( $\text{MgH}_2$ ). Hereby, we will discuss that, in fact, the material crystalline morphology has a tremendous influence on the hydrogen diffusion properties. Furthermore, we will propose in this chapter a liquid hydrogenation scheme for plasmonic nanoantennas based on al-

cohol deprotonation. It will be shown that Y nanoantennas can be hydrogenated to yttrium dihydride ( $\text{YH}_2$ ) and thus switch their optical plasmonic properties upon exposure to, e.g., ethanol. This way a nanooptical indicator platform to detect alcohol deprotonation is demonstrated.

- Chapter 4 shifts gears by analyzing the optical properties of single chiral plasmonic gold nanoparticles via chiral scatterometry. First, the home-built and fully automated measurement technique of chiral scatterometry is explained. Subsequently, it is used to investigate large sets of helicoid single nanoparticles. We unravel that these helicoids possess very large optical activity. Thus, they show tremendous potential for being used in chiral sensing platforms to further decrease sensing volumes. We will give a detailed comparison between a single nanoparticle response and the response from nanoparticles in ensemble. Furthermore, we explain the exact influence of particle morphology on the chiroptical responses. The chapter will finish with an investigation on the evolution of the nanoparticle chirality by measurements of the chiroptical responses at different steps of the helicoid nanoparticle synthesis.

## ELECTRO-ACTIVE METALLIC POLYMER NANOANTENNAS AND METASURFACES

---

This chapter is based on the following published work:

- **J. Karst**, M. Floess, M. Ubl, C. Dingler, C. Malacrida, T. Steinle, S. Ludwigs, M. Hentschel, and H. Giessen  
*Electrically Switchable Metallic Polymer Nanoantennas*  
*Science* **374**, 612 (2021).
- **J. Karst**, Y. Lee, M. Floess, M. Ubl, S. Ludwigs, M. Hentschel, and H. Giessen  
*Electro-Active Metaobjective from Metalenses On-Demand*  
*Nature Communications*, under review (2022).

### 2.1 INTRODUCTION

Miniaturizing optical components is key to achieve ultimate spatiotemporal control of light. This will allow for the realization and improvement of emerging and critical optical technologies such as augmented reality (AR) and virtual reality (VR), dynamic holography, light detection and ranging (LiDAR), or high-resolution wavefront and polarization shapers.

Subwavelength nanoantennas have proven to be a prime candidate to achieve this goal [1–5]. Due to their resonant nature, they allow a highly efficient local interaction with light. Further, the nanostructures can locally enhance the manipulation, detection, or modulation of light on ultra-small subwavelength scales. The advent of metasurfaces has given us tools to realize first plasmon-based spatially dependent static light control on nanometer scales [6–9]. This includes ultrathin optical elements with functionalities ranging from beam steering devices for LiDAR [1, 4, 10–12], to dynamic metalenses [13–22], metasurfaces for VR and AR applications [3, 23–28], or photonic spatial light modulators [4, 29, 30]. They are typically made from metals but also from dielectrics in order to achieve generalized amplitude and phase control [31–37]. Besides these tremendous achievements it is obvious that for the integration

into dynamic electro-optical components, an active spatiotemporal light control with nanoantennas is necessary [38–40]. This requires a dynamic change of the optical properties upon an external stimulus. One possibility is to operate nanoantennas close to a phase transition which can result in switchable plasmonic resonances and active metasurfaces with high contrast ratios [28, 41–43]. Such direct modifications rely on structural or chemical material transitions that were stimulated, until now, by chemical reactions [41, 44], gas exposure [45–48], or temperature [49, 50]. They usually exhibit slow transitions, incomplete reversibility, or switching schemes which are complicated to integrate into electro-optical devices. One alternative is an indirect alteration of the optical properties typically via an electrically- or temperature-driven change of the surrounding medium [11, 12, 17, 23, 25, 29, 51–56]. This results, however, only in a tuning of the resonance intensity, position, and linewidth, thus limiting the achievable contrast in active metasurface applications. Yet, to date, a directly electrically switchable nanoantenna with the possibility to turn the nanoantenna resonance fully ON and OFF at high frequencies has not been realized.

In this chapter we introduce such electrically switchable nanoantennas, made from a metallic polymer with an electrochemically driven metal-to-insulator transition in the near-infrared spectral range caused by a variation of the charge carrier density. Our polymer nanoantennas possess a full ON- and OFF-state in their metallic and insulating optical state, respectively, and are switchable at video-rate frequencies of up to 30 Hz by applying voltages of only  $\pm 1$  V. Based on this concept, we realize a purely electrically switchable metasurface for active beam steering with 100% contrast ratio in the diffracted beam. Furthermore, we demonstrate active metalenses-on-demand and a multi-functional metaobjective composed of electrically switchable metallic polymer nanoantennas.



## 2.2 THEORETICAL BACKGROUND

Metallic materials and plasmonic nanoparticles can interact with electromagnetic fields. It is important to predict, alter and understand their optical responses. For frequencies up to the visible part of the electromagnetic spectrum, metals typically show a high reflectivity. That means, they limit electromagnetic fields to be absorbed, scattered, or transmitted. Yet, at higher frequencies the response of metals and nanoparticles can be more complicated. In the following, we will thus give a short introduction into theoretical background to understand especially plasmonic phenomena in metals, especially in metallic polymers, in more detail.<sup>1</sup>

## 2.2.1 MAXWELL'S Equations

The fundamental MAXWELL'S equations are the starting point for the explanation of lots of electrodynamic phenomena. For light-matter interaction the MAXWELL equations are given as

$$\nabla \cdot \mathbf{D} = \rho_{\text{ext}}, \quad (2.1a)$$

$$\nabla \cdot \mathbf{B} = 0, \quad (2.1b)$$

$$\nabla \times \mathbf{E} = -\frac{\partial \mathbf{B}}{\partial t}, \quad (2.1c)$$

$$\nabla \times \mathbf{H} = \mathbf{j}_{\text{ext}} + \frac{\partial \mathbf{D}}{\partial t}, \quad (2.1d)$$

representing relations between the dielectric displacement  $\mathbf{D}$ , electric field  $\mathbf{E}$ , magnetic flux density  $\mathbf{B}$ , the magnetic field  $\mathbf{H}$ , the external charge  $\rho_{\text{ext}}$  and the external current density  $\mathbf{j}_{\text{ext}}$ . These four macroscopic fields are linked with each other via the magnetization  $\mathbf{M}$  and the polarization  $\mathbf{P}$  by

$$\mathbf{D} = \varepsilon_0 \mathbf{E} + \mathbf{P}, \quad (2.2a)$$

$$\mathbf{H} = \frac{1}{\mu_0} \mathbf{B} - \mathbf{M}, \quad (2.2b)$$

where  $\varepsilon_0$  is the electric permittivity<sup>2</sup> and  $\mu_0$  is the magnetic permeability<sup>3</sup> of vacuum.

Furthermore, one can define for linear and isotropic media

$$\mathbf{D} = \varepsilon_0 \varepsilon \mathbf{E}, \quad (2.3a)$$

$$\mathbf{B} = \mu_0 \mu \mathbf{H}. \quad (2.3b)$$

<sup>1</sup> Please note that sections 2.2.1 to 2.2.4 are based on [57], which follows the notation of [58].

<sup>2</sup>  $\varepsilon_0 = 8.854 \cdot 10^{-12}$  F/m

<sup>3</sup>  $\mu_0 = 1.257 \cdot 10^{-6}$  H/m

The relative permittivity  $\varepsilon$  and the relative permeability  $\mu$  are material-dependent. For a non-magnetic material (all materials in this thesis)  $\mu$  can be set to  $\mu = 1$ .

An important relation, especially for the quantum mechanical treatments of the optical response [59], is

$$\mathbf{P} = \varepsilon_0 \chi \mathbf{E}, \quad (2.4)$$

where  $\chi = \varepsilon - 1$  denotes the dielectric susceptibility. One can find a linear relationship between the current density  $\mathbf{j}$  and  $\mathbf{E}$  as

$$\mathbf{j} = \sigma \mathbf{E}. \quad (2.5)$$

The optical conductivity  $\sigma(\mathbf{k}, \omega)$ , as a function of the wave vector  $\mathbf{k}$  and the angular frequency  $\omega$ , can be correlated with  $\varepsilon$  by means of the fundamental equation

$$\varepsilon(\mathbf{k}, \omega) = 1 + \frac{i\sigma(\mathbf{k}, \omega)}{\varepsilon_0 \omega}. \quad (2.6)$$

In general,

$$\varepsilon(\omega) = \varepsilon_1(\omega) + i\varepsilon_2(\omega), \quad (2.7a)$$

$$\sigma(\omega) = \sigma_1(\omega) + i\sigma_2(\omega) \quad (2.7b)$$

are complex variables, where  $\mathbf{k} = 0$  in the limit of a spatially local response (the wavelength  $\lambda$  in matter is significantly longer than the size of the unit cell and the mean free path of the electrons).

The complex refractive index of a medium  $\hat{n} = n + i\kappa$  is linked to  $\varepsilon(\omega)$  via

$$\hat{n} = \sqrt{\varepsilon}, \quad (2.8a)$$

$$\rightarrow \varepsilon_1 = n^2 - \kappa^2, \quad (2.8b)$$

$$\rightarrow \varepsilon_2 = 2n\kappa, \quad (2.8c)$$

resulting in relations between the real and imaginary part of  $\varepsilon$  and the real part  $n$  (normal refractive index) and the imaginary part  $\kappa$  (extinction coefficient) of  $\hat{n}$ . These equations (eqs. 2.8b and 2.8c) lead to the assumption that the change of the phase velocity  $c_n$  in a medium is mostly determined by  $\varepsilon_1$  and the absorption by  $\varepsilon_2$ .

The extinction coefficient  $\kappa$

$$\kappa = \frac{c\alpha}{2\omega} \quad (2.9)$$

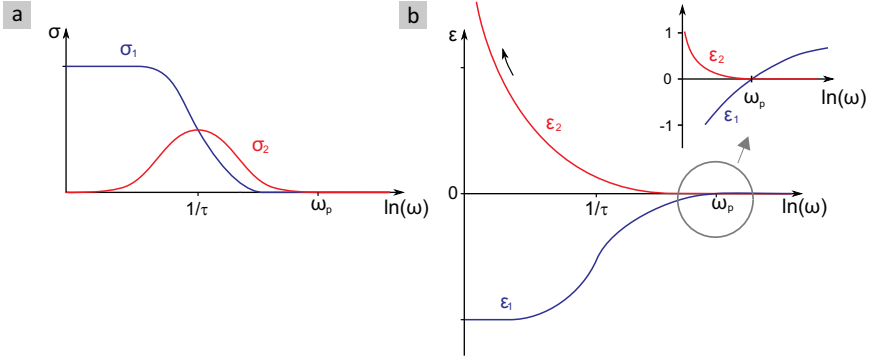


FIGURE 2.1. **Theoretical dispersion in Drude model.** Qualitative progression of the real part (blue) and the imaginary part (red) of the frequency dependent (a) conductivity  $\sigma$  and (b) dielectric function  $\varepsilon$  for the free electron gas described via the DRUDE model.

is directly related to the optical absorption of electromagnetic waves travelling through a medium, which is expressed by the absorption coefficient  $\alpha$  of BELL'S law. It describes the exponential attenuation  $I(x) = I_0 e^{-\alpha x}$  of a wave propagating through the medium. The appropriate wave equations for electromagnetic waves in matter are consequently given as

$$\Delta \mathbf{E} = \mu_0 \mu \sigma \frac{\partial \mathbf{E}}{\partial t} + \frac{1}{c^2} \mu \varepsilon \frac{\partial^2 \mathbf{E}}{\partial t^2}, \quad (2.10a)$$

$$\Delta \mathbf{H} = \mu_0 \mu \sigma \frac{\partial \mathbf{H}}{\partial t} + \frac{1}{c^2} \mu \varepsilon \frac{\partial^2 \mathbf{H}}{\partial t^2}. \quad (2.10b)$$

### 2.2.2 DRUDE Model

The easiest way to explain the optical properties of metals at high frequencies around the plasma frequency  $\omega_p$  is via the DRUDE model. It describes the electrons in a metal as a free electrons gas which oscillates in response to an external field  $\mathbf{E} = \mathbf{E}_0 e^{-i\omega t}$ . The equation of motion for such an electron in the electron gas is given by

$$m\ddot{\mathbf{x}} + m\gamma\dot{\mathbf{x}} = -e\mathbf{E}, \quad (2.11)$$

where  $\gamma = 1/\tau$  is now representing the characteristic collision frequency. In this context,  $\tau$  is the relaxation time of the free electron gas.

Again, one uses the assumption  $\mathbf{x}(t) = \mathbf{x}_0 e^{-i\omega t}$  to determine an expression for the displacement  $\mathbf{x}$  as

$$\mathbf{x} = \frac{e}{m(\omega^2 + i\gamma\omega)} \mathbf{E}. \quad (2.12)$$

Similar to the LORENTZ model, the electrons account for the macroscopic polarization  $\mathbf{P} = -Nex$ . By inserting  $\mathbf{P}$  into equation (eq. 2.2a) one maintains the dielectric function of the free electron gas/metal

$$\varepsilon(\omega) = 1 - \frac{\omega_p^2}{\omega^2 + i\gamma\omega} \quad (2.13a)$$

$$= 1 - \underbrace{\frac{\omega_p^2 \tau^2}{1 + \omega^2 \tau^2}}_{\text{real part } \varepsilon_1} + i \underbrace{\frac{\omega_p^2 \tau}{\omega(1 + \omega^2 \tau^2)}}_{\text{imaginary part } \varepsilon_2}. \quad (2.13b)$$

The conductivity can be calculated with equation (eq. 2.6). The plasma frequency (in units Hz) is given as

$$\omega_p = \sqrt{\frac{n_p e^2}{\varepsilon_0 m^*}}, \quad (2.14)$$

where  $n_p$  denotes the charge carrier density,  $e$  the elemental charge, and  $m^*$  the effective mass of an electron.  $\omega_p$  defines the frequency or wavelength, where the real part of the dielectric function  $\varepsilon_1$  becomes zero. Here, the material transitions from a metal  $\varepsilon_1 < 0$  for  $\omega < \omega_p$  to a dielectric  $\varepsilon_1 > 0$  for  $\omega > \omega_p$ . This can be seen in the qualitative progression of  $\varepsilon$  and  $\sigma$  in Figure 2.1.

For frequencies near  $\omega_p$ , the damping is negligible and the dielectric function contains only a real part

$$\varepsilon(\omega) = 1 - \frac{\omega_p^2}{\omega^2}, \quad (2.15)$$

which can be dedicated to the undamped free electron gas. This simplification is only valid for metals which show no interband transition.

As mentioned, for frequencies higher than the plasma frequency  $\omega > \omega_p$ , metals lose their metallic character and become dielectric with  $\varepsilon_1 > 0$ . Actually, the dielectric constant  $\varepsilon(\omega)$  shows a limit value of  $\varepsilon = 1$  for  $\omega \rightarrow \infty$ . For the most noble metals one has to take into account the influence of  $\varepsilon_\infty$ , because the filled d-band close to

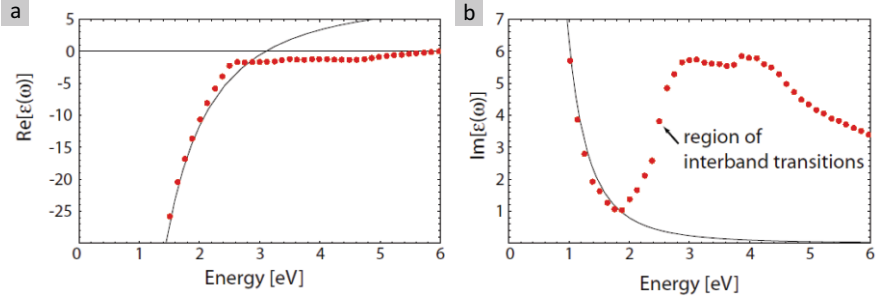


FIGURE 2.2. **Drude model on experimental data.** (a) Real part and (b) imaginary part of the dielectric function of the DRUDE model fitted to the measured data of Johnson and Christy [60]. The plots are taken from [58].

the Fermi surface causes a highly polarized environment. One rewrites equation (eq. 2.13a) as

$$\epsilon(\omega) = \epsilon_{\infty} - \frac{\omega_p^2}{\omega^2 + i\gamma\omega}. \quad (2.16)$$

In Figure 2.2 one can see the limits of the DRUDE model. It shows the curves for the real and imaginary part of  $\epsilon$  to the measured data of gold [60]. The model breaks down for visible frequencies due to the interband transitions of gold.

The free electron gas model can be linked to the classical DRUDE model [61]. DRUDE made the assumption that electrons with the momentum  $\mathbf{p}$  hit other particles after a characteristic relaxation time  $\tau$ . In doing so they lose their momentum  $\mathbf{p}$ . One can easily identify DRUDE's equation of motion

$$\dot{\mathbf{p}} = -\frac{\mathbf{p}}{\tau} - e\mathbf{E} \quad (2.17)$$

with equation (eq. 2.11) by using  $\mathbf{p} = m\dot{\mathbf{x}}$ . The result of this equation of motion is an expression for the optical AC conductivity

$$\sigma(\omega) = \frac{\sigma_0}{1 - i\omega\tau} \quad (2.18)$$

with the DC conductivity

$$\sigma_0 = \frac{Ne^2\tau}{m}. \quad (2.19)$$

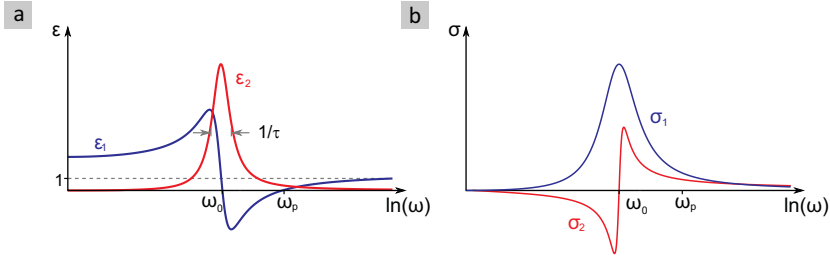


FIGURE 2.3. **Theoretical dispersion in Lorentz model.** (a) Qualitative progression of the real part (blue) and the imaginary part (red) of the frequency dependent dielectric function  $\epsilon$  in (a) and the conductivity  $\sigma$  in (b) for the LORENTZ model.

### 2.2.3 LORENTZ Model

The more complex LORENTZ model is typically used to describe the optical properties of materials around a resonance  $\omega_0$ . Such resonances can be infrared (IR) vibrations of molecules, optical phonon resonances, or localized nanoparticle plasmons. The LORENTZ model treats molecules as a damped harmonic oscillator. The electrons with the charge  $e$  and mass  $m$  are linked to the atomic core and oscillate with the frequency  $\omega$ . This damped harmonic oscillator has a resonance frequency  $\omega_0$  and a damping constant  $\gamma$ . The equation of motion of such an oscillator with the displacement  $\mathbf{x}$  from its zero point in an external electric field  $\mathbf{E} = \mathbf{E}_0 e^{-i\omega t}$  is given by

$$m\ddot{\mathbf{x}} + m\gamma\dot{\mathbf{x}} + m\omega_0^2 \mathbf{x} = e\mathbf{E}. \quad (2.20)$$

With the assumption for the displacement  $\mathbf{x}(t) = \mathbf{x}_0 e^{-i\omega t}$ , one obtains

$$\mathbf{x} = -\frac{e}{m} \frac{1}{\omega_0^2 - \omega^2 - i\gamma\omega} \mathbf{E}. \quad (2.21)$$

The displacement is linked to the dielectric function  $\epsilon$  via the polarization  $\mathbf{P} = -Nex = N\hat{\alpha}\mathbf{E}$  ( $N$  atoms per unit cell) and the corresponding polarizability  $\hat{\alpha}$

$$\epsilon = 1 + \frac{N}{\epsilon_0} \hat{\alpha} = 1 + \frac{N}{\epsilon_0} \frac{e\mathbf{x}}{\mathbf{E}}. \quad (2.22)$$

This leads to the complex dielectric function of the LORENTZ model

$$\epsilon(\omega) = 1 + \omega_p^2 \frac{1}{\omega_0^2 - \omega^2 - i\gamma\omega} \quad (2.23)$$

with the known plasma frequency  $\omega_p$  from (eq. 2.14).

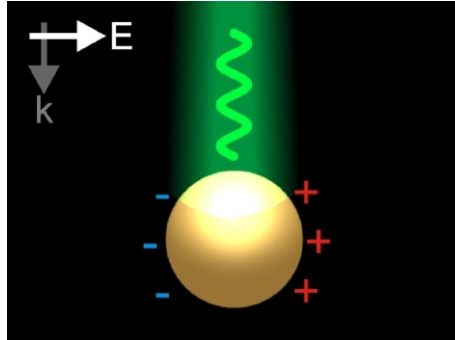


FIGURE 2.4. **Excitation of localized surface plasmon in a metallic nanoparticle.** An external light field (green) propagating in direction  $\mathbf{k}$  with electric field  $\mathbf{E}$  is incident on a metallic particle. Hereby, collective oscillations of the quasi-free conduction electrons can be excited. This excitation causes a periodic displacement of the electron cloud (with respect to the ionic background) leading to strong local electric fields in the vicinity of the nanoparticle.

As we know from above, the dielectric function  $\epsilon$  is linked to the conductivity  $\sigma$  via (eq. 2.6). The qualitative progression of real and imaginary part of  $\epsilon$  and  $\sigma$  can be found in Figure 2.3.

#### 2.2.4 Localized Surface Plasmons

In general, there are three different types of plasmons in existence: volume plasmons, surface plasmons, and localized surface plasmons (LSPs). Hereby, the LSPs are the only ones directly excitable with light and are the basis for all plasmonic nanoparticle resonances in this thesis. These non-propagating excitations of the conduction electrons of metallic nanostructures can be directly coupled to the electromagnetic field (see Figure 2.4). Mandatory is that the nanoparticles are smaller than the wavelength of the incident light.

Depending on the size and shape of the nanoparticle, a resonance wavelength due to collective oscillations of the quasi-free conduction electrons is observed. To understand the physics behind this phenomenon, one starts from the simple model of a homogeneous, isotropic sphere. As mentioned, this calculation follows the notation of [58]. A sketch of this sphere with the radius  $a \ll \lambda$  and the dielectric function  $\epsilon(\omega)$  can be seen in Figure 2.5. It is placed at the origin of a uniform, electrostatic field

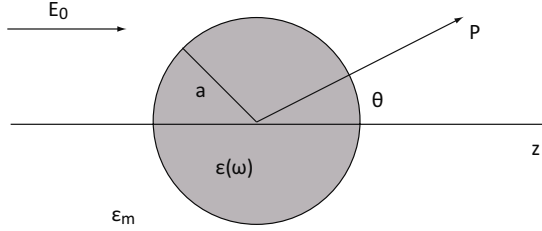


FIGURE 2.5. **Sketch of a homogeneous sphere** with dielectric function  $\varepsilon(\omega)$  and radius  $a$ , which is placed in the origin of a uniform, electrostatic field. It is surrounded by a medium with dielectric constant  $\varepsilon_m$ . Sketch reproduced from [58]

$\mathbf{E} = E_0 \hat{\mathbf{z}}$ . The sphere is surrounded by an isotropic, non-absorbing medium with the dielectric constant  $\varepsilon_m$ .

The following calculation is aimed at a solution  $\mathbf{E} = -\nabla\Phi$  for the Laplace equation

$$\nabla^2\Phi = 0. \quad (2.24)$$

Due to the azimuthal symmetry of the problem, the general solution is of the form

$$\Phi(r, \theta) \sum_{l=0}^{\infty} \left[ A_l r^l + B_l r^{-(l+1)} \right] P_l(\cos \theta), \quad (2.25)$$

where  $P_l(\cos \theta)$  are the LEGENDRE Polynomials of the order  $l$  and  $\theta$  is the angle between vector  $\mathbf{r}$  at point  $P$  and the  $z$ -axis. The coefficients  $A_l$  and  $B_l$  are determined by boundary conditions at the surface of the sphere with  $r = a$  and at  $r \rightarrow \infty$ . After separating the potential  $\Phi$  into a potential inside and a potential outside the sphere, one can determine the coefficients and obtains the solutions for  $\Phi_{\text{in}}$  and  $\Phi_{\text{out}}$  as

$$\Phi_{\text{in}} = -\frac{3\varepsilon_m}{\varepsilon + 2\varepsilon_m} E_0 r \cos \theta, \quad (2.26a)$$

$$\Phi_{\text{out}} = -E_0 r \cos \theta + \frac{\varepsilon - \varepsilon_m}{\varepsilon + 2\varepsilon_m} E_0 a^3 \frac{\cos \theta}{r^2}. \quad (2.26b)$$

By having a closer look at the potential outside the sphere, one can take  $\Phi_{\text{out}}$  as a sum of the field of a dipole (dipole moment  $\mathbf{p}$  located at the particle center) and the applied field. Equation (eq. 2.26b) can be rewritten as

$$\Phi_{\text{out}} = -E_0 r \cos \theta + \frac{\mathbf{p} \cdot \mathbf{r}}{4\pi\varepsilon_0} \varepsilon_m r^3, \quad (2.27a)$$

$$\rightarrow \mathbf{p} = 4\pi\varepsilon_0 \varepsilon_m a^3 \frac{\varepsilon - \varepsilon_m}{\varepsilon + 2\varepsilon_m} \mathbf{E}_0, \quad (2.27b)$$



which means that the external field induces a dipole moment inside the sphere.

By using the equation

$$\mathbf{p} = \varepsilon_0 \varepsilon_m \hat{\alpha} \mathbf{E}_0, \quad (2.28)$$

one arrives at an expression for the polarizability

$$\hat{\alpha} = 4\pi a^3 \frac{\varepsilon - \varepsilon_m}{\varepsilon + 2\varepsilon_m}. \quad (2.29)$$

This equation for  $\hat{\alpha}$  is the most important result of this calculation. The polarizability shows a resonant enhancement for  $|\varepsilon + 2\varepsilon_m|$  being a minimum. Around the resonance, if  $\text{Im}[\varepsilon]$  is small, the resonance condition simplifies to

$$\text{Re}[\varepsilon] = -2\varepsilon_m. \quad (2.30)$$

This relation is called the Fröhlich condition for a dipole surface plasmon of the nanoparticle. A DRUDE metal in air fulfills this Fröhlich criterion for a frequency of

$$\omega_{\text{LSP}} = \frac{\omega_p}{\sqrt{3}}. \quad (2.31)$$

The resonance wavelength/frequency shows a strong dependence on the surrounding media/dielectric, which means that the resonance red-shifts as  $\varepsilon_m$  is increased.

Furthermore, one can determine the electric field  $\mathbf{E} = -\nabla\Phi$  with the calculated potentials (eqs. 2.26a and 2.26b):

$$\mathbf{E}_{\text{in}} = \frac{3\varepsilon_m}{\varepsilon + 2\varepsilon_m} \mathbf{E}_0, \quad (2.32a)$$

$$\mathbf{E}_{\text{out}} = \mathbf{E}_0 + \frac{3\mathbf{n}(\mathbf{n} \cdot \mathbf{p}) - \mathbf{p}}{4\pi\varepsilon_0\varepsilon_m} \cdot \frac{1}{r^3}. \quad (2.32b)$$

Fulfilling the condition (eq. 2.30), the electric field inside and outside of the spherical nanoparticle becomes resonantly enhanced.

If one has a look on the scattering and absorption cross sections of a nanoparticle, one asserts that they are also dependent on the polarizability  $\hat{\alpha}$ , which means that they are also resonantly enhanced. This result can be transferred to darkfield spectroscopy. Thus, it is possible to see nanoparticles which are smaller than the wavelength of visible light using e.g. a darkfield microscope. The resonance contribution leads to an enhancement in the efficiency with which a nanoparticle absorbs and scatters light.

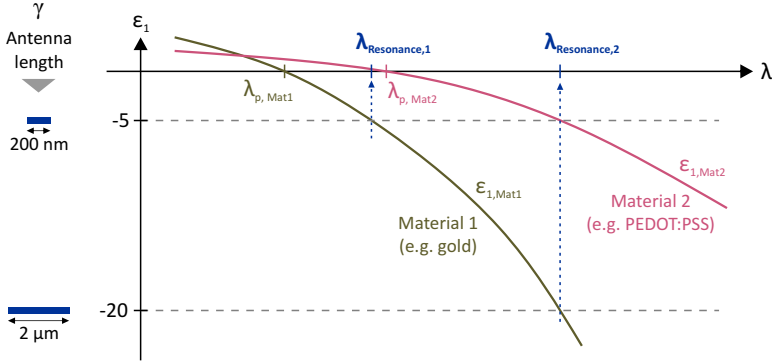


**FIGURE 2.6. Influence of dielectric function on resonance position of plasmonic nanoantennas.** Relative permittivity  $\epsilon_1$  as a function of wavelength for two different materials. Material 1 (olive, e.g. gold) possesses a shorter plasma wavelength  $\lambda_p$ / higher plasma frequency  $\omega_p$  than material 2 (red, e.g. poly(3,4-ethylenedioxythiophene):polystyrene sulfonate (PEDOT:PSS)). Additionally,  $\epsilon_{1,Mat1}(\lambda)$  has a steeper slope in comparison to  $\epsilon_{1,Mat2}$ , strongly influencing the resonance position  $\lambda_{Resonance}$  of a nanoantenna with Eigenvalue  $\gamma$ . Each value of  $\epsilon_1$  requires a specific Eigenvalue  $\gamma$  (translating into a specific nanoantenna length), to fulfill the resonance condition eq. 2.33. The wavelength where material 1 or 2 matches this value of  $\epsilon_1$  defines the resonance wavelength  $\lambda_{Resonance}$  of the nanoantenna.

This whole theory is based on a homogeneous, isotropic sphere. Of course this is just a model. But it gives a basic understanding of the excitation of localized surface plasmons. For different shapes, it is very challenging to calculate the electric fields or the resonance positions analytically. The most of them need a numerical calculation method. Moreover, one can calculate the resonances of a sphere more accurate. Therefore, one has to consider for example the oscillating time-dependent electromagnetic field which interacts with the nanoparticle. Especially for nanoparticles with a size near to the wavelength of visible light, it is important to consider this fact. Therefore, one can use theories such as the Mie theory. In the book “*Absorption and Scattering of Light by Small Particles*” by Bohren & Huffman one can have a closer look at profound calculations [62]. The conclusion of the upper calculations, especially the strong dependence of the electric field on the surrounding dielectric  $\epsilon_m$ , is very important when it comes to understanding the resonances of plasmonic nanoparticles and metasurfaces.

Besides the dielectric function of the surrounding medium, also the dielectric function (relative permittivity) of the nanoparticle material  $\varepsilon_{1,\text{NP}}$  influences the nanoparticle resonance. In general, one finds a resonance condition [63]

$$\gamma[\varepsilon_{1,\text{NP}}(\omega) + \varepsilon_m] = \varepsilon_{1,\text{NP}}(\omega) - \varepsilon_m, \quad (2.33)$$

where the Eigenvalue  $\gamma$  is defined by the nanoparticle geometry. This concept is illustrated in Figure 2.6. We plot the relative permittivity  $\varepsilon_1$  as a function of wavelength  $\lambda$  for two different nanoparticle materials. Material 1 (for example gold) is plotted in olive, whereas material 2 (for example metallic polymer PEDOT:PSS) is plotted in red. Material 1 has a short plasma wavelength  $\lambda_{\text{p,Mat1}}$  in comparison to  $\lambda_{\text{p,Mat2}}$  of material 2. Furthermore, the overall slope of  $\varepsilon_{1,\text{Mat1}}$  is larger compared to  $\varepsilon_{1,\text{Mat2}}$ . In this qualitative comparison, each value of  $\varepsilon_1$  defines an Eigenvalue  $\gamma$ , translating into a specific nanoantenna length, as it is illustrated on the y-axis in Figure 2.6. We now assume nanoantennas with a length of 200 nm (corresponding to  $\varepsilon_1 = -5$ ) once made from material 1 (gold) and once from material 2 (PEDOT:PSS). The resonance condition eq. 2.33 states that we will find the gold nanoantennas with a length of 200 nm to resonate at resonance wavelength  $\lambda_{\text{Resonance,1}}$ , whereas identical nanoantennas from PEDOT:PSS will resonate at a higher wavelength  $\lambda_{\text{Resonance,2}}$ . Vice versa, in order to obtain a gold nanoantenna with a plasmonic resonance at  $\lambda_{\text{Resonance,2}}$ , its length needs to be increase to 2  $\mu\text{m}$ , as it is marked in Figure 2.6. In conclusion, the course of  $\varepsilon_{1,\text{NP}}(\omega)$  of the nanoparticles strongly influences the resonance position. Hereby, not only the plasma frequency  $\omega_p$  / plasma wavelength  $\lambda_p$ , but also the slope of  $\varepsilon_{1,\text{NP}}(\omega)$  plays an important role.

### 2.2.5 *Metallic Polymers*

This chapter uses no standard metals such as gold or aluminum for plasmonic nanoantennas. Rather, we use polymers, which become metallic in a certain spectral range. As explained in section 2.2.2, this spectral range is given wherever the real part  $\varepsilon_1(\omega)$  of the dielectric function  $\varepsilon(\omega) = \varepsilon_1(\omega) + i\varepsilon_2(\omega)$  becomes negative and thus the material becomes *optically* metallic. An example of a dielectric function for such a metallic polymer (PEDOT:PSS) has been shown in Figure 2.6 (red curve). Plasmonic nanoantennas from such a metallic polymer can consequently show a plasmonic resonance for  $\omega < \omega_p$ , respectively  $\lambda > \lambda_p$ . A plasmonic high-frequency and collective oscillation optimization problem is in stark contrast to the common quest in polymer material science to improve and enhance the DC (direct current) conductivity of conductive polymers. Here, the general charge carrier transfer mechanism (e.g., hopping transfer) over large distances has a much bigger influence on the DC conductivity than it has on

the plasma frequency at very high AC (alternating current) frequencies in small scale plasmonic systems. Consequently, an increase/decrease of the DC conductivity of an optically metallic polymer does not directly coincide with an increase/decrease of its plasma frequency. Rather, as seen from eq. 2.14, a change of  $\omega_p$  is mostly influenced by a change in the local charge carrier density  $n_\rho$  of the metallic polymer. This becomes even more clear by roughly estimating the periodic displacement  $\Delta s$  of the electron cloud (with respect to the ionic background) in a plasmonic nanoantenna when illuminated with an optical high-frequency electro-magnetic wave. The displacement in such a plasmonic system can be estimated with

$$\Delta s = v * t = v_F * \tau, \quad (2.34)$$

where  $v_F$  is the FERMI-velocity and  $\tau$  is the period of the impinging electromagnetic wave. We assume an illumination wavelength of  $\lambda = 600$  nm, corresponding to an optical frequency of 500 THz which is equivalent to a period  $\tau = 2$  fs. Furthermore, we assume a typical FERMI-velocity for metallic materials in the range of  $v_F = 10^6$  m/s. Consequently, the maximum displacement of the electron cloud during one collective oscillation period is found to be only

$$\Delta s \approx 2 \text{ nm}. \quad (2.35)$$

On such small length scales the long-range order as well as conductivity and mobility of charge carriers over multiple polymer chains become negligible. Rather, the short-range order and local charge carrier density determines the optical properties of the metallic polymer. Further theoretical background on metallic polymers will be discussed directly in section 2.4. A more detailed discussion on the chemical and physical properties of metallic/conductive polymers can be found in [64].

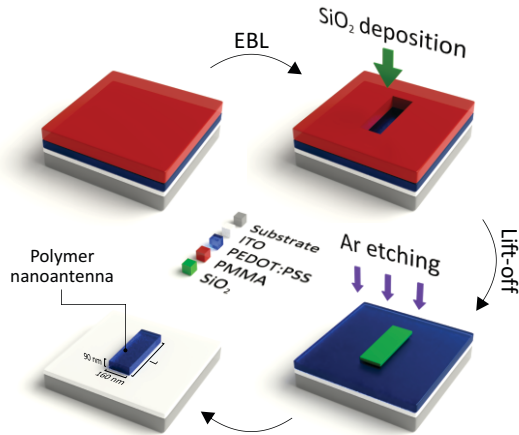


**FIGURE 2.7. Fabrication of plasmonic nanoantennas made from metallic polymer.** PEDOT:PSS is used as metallic polymer. It is spin-coated with no pre- or post-treatment onto 20 nm indium-tin-oxide (ITO) (for electrical contact) on glass substrates. The PEDOT:PSS is overcoated with poly(methyl methacrylate) (PMMA) as positive tone-resist for electron beam lithography (EBL). After development a 30 nm  $\text{SiO}_2$  etch mask is deposited via electron-gun evaporation, followed by a standard lift-off in acetone. After a subsequent argon (Ar) etching to remove uncovered polymer a nanoantenna from PEDOT:PSS on ITO is obtained.

## 2.3 INSTRUMENTATION

### 2.3.1 Fabrication Routine

As mentioned, we use in the following work metallic polymers to obtain electrically switchable plasmonic nanoantennas. As material of choice we use the metallic polymer PEDOT:PSS. Structuring PEDOT:PSS is remarkably straightforward, underpinning the broad applicability of the material for plasmonic nanoantennas and metasurfaces (Figure 2.7). Commercially available PEDOT:PSS (Heraeus Clevious PH1000, Ossila) is spin-coated from an aqueous dispersion onto ITO-coated glass substrates with 2500 RPM (5 s) followed by 3000 RPM (55 s) using a  $0.45 \mu\text{m}$  syringe filter. Drying is performed at  $120^\circ \text{C}$  for 15 min. We explicitly use no pre- or posttreatment as this can drastically influence the plasmonic properties of the polymer [65]. This results in smooth 90 nm thick metallic polymer films, well suited for the subsequent EBL process. For EBL we use a two-layered PMMA positive tone-resist (Allresist AR-P 642.06 200k

+ Allresist AR-P 672.02 950k) allowing for high-resolution nanoantenna structures. After development in methylisobutylketone (MIBK), a 30 nm silicon-dioxide ( $\text{SiO}_2$ ) layer is deposited via electron-gun evaporation followed by a lift-off in acetone. This dielectric  $\text{SiO}_2$  layer is used as etch-mask for the subsequent Ar etching process to remove uncovered PEDOT:PSS. Consequently, this leads to a polymer nanoantenna from PEDOT:PSS on ITO. There is the possibility that part of the  $\text{SiO}_2$  mask might remain on the nanoantennas. Consequently, the electrolyte might not have access to the entire antenna, which can reduce switching/diffusion times.

### 2.3.2 *Electrochemical Setup*

We use a home-built electrochemical cell (optical thickness: 1.5 mm) for the electrical switching of the polymer nanoantennas with a three-electrode setup. Our cell is sealed on the top and bottom with thin glass windows for the optical access in transmission experiments. The sides have fittings for in- and out-flow of the electrolyte, as well as fittings for the reference and counter electrode. We use 0.1 mol/l TBAPF<sub>6</sub> in Acetonitrile as electrolyte. The PEDOT:PSS nanoantennas on ITO serve as the working electrode. The ITO is connected outside of the electrochemical cell. A platinum wire is used as counter electrode, silver/silverchloride (Ag/AgCl) is used as reference electrode. All electrodes are connected to a potentiostat (BioLogic SP-200) which controls the voltage applied to the polymer nanoantennas. Please note that the exact arrangement of samples inside the electrochemical cell varies throughout this chapter. This is why we will give details on the individual measurement procedure and setup in necessary sections.

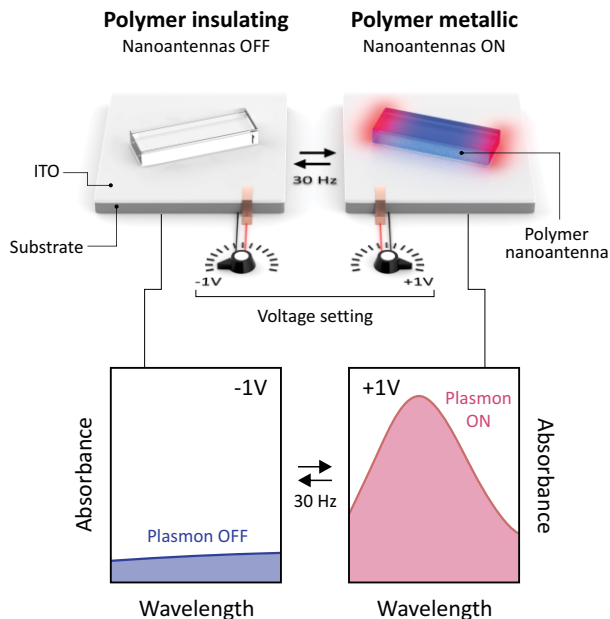


FIGURE 2.8. **Concept of electrically switchable nanoantennas.** Illustration of the electrical switching of an individual plasmonic nanoantenna made from metallic polymers with metal-to-insulator transition. Right: An applied voltage of +1 V turns the polymer nanoantenna ON into the metallic plasmonic state, exhibiting a plasmonic resonance as illustrated below. Left: This plasmonic property/resonance is turned off when a voltage of -1 V is applied as the polymer becomes insulating. The switching between the two states reaches video-rate frequencies of 30 Hz. ITO on glass substrates is used for the electrical contact.

## 2.4 ELECTRICALLY SWITCHABLE METALLIC POLYMER NANOANTENNAS

### 2.4.1 Concept

The main concept of our electrically switchable plasmonic system made from metallic polymers is illustrated in Figure 2.8. Nanoantennas made from the metallic polymer can be electrically switched via the applied voltage. When we apply a voltage of +1 V (Figure 2.8, right), the polymer is electrochemically doped and is fully oxidized with a high carrier density, leading to metallic optical properties. The polymer nanoantenna is turned ON, and a strong plasmonic nanoantenna resonance can be observed. In

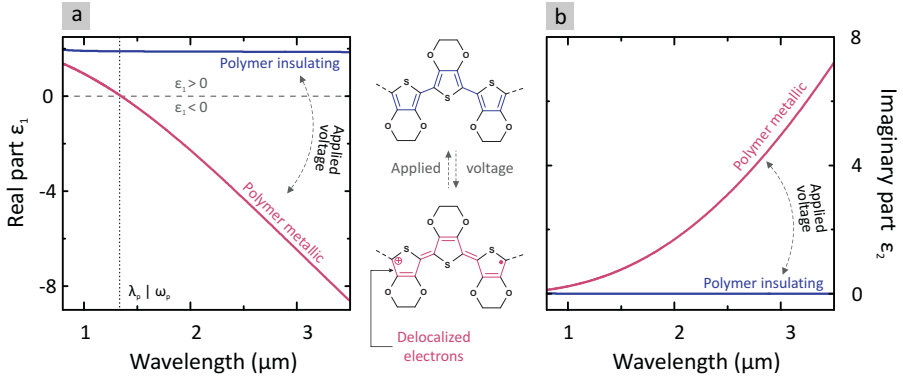


FIGURE 2.9. **Dielectric function of PEDOT:PSS upon electrical switching.** (a) Real part  $\epsilon_1$  and (b) imaginary part  $\epsilon_2$  of the dielectric function  $\epsilon = \epsilon_1 + i\epsilon_2$  of PEDOT:PSS thin films in the metallic (red) and insulating state (blue). A metallic polymer with  $\epsilon_1 < 0$  is obtained in the near-infrared (NIR) and mid-infrared (MIR) for wavelengths  $\lambda > 1.3 \mu\text{m}$ . Via the applied voltage, the polymer can be switched into an insulating state with  $\epsilon_1 > 0$  in the entire wavelength range. The inset shows the structural conversion of the metal-to-insulator transition.

contrast, when the applied voltage is changed to -1 V (Figure 2.8, left), the optical properties of the polymer become insulating as the carrier density is drastically reduced. This leads to a nanoantenna with no plasmonic properties and resonances - the plasmonic nanoantenna is turned OFF. The electrical switching between ON and OFF state occurs very fast and allows for switching speeds at video-rate frequencies of 30 Hz - this is significantly faster than any state-of-the-art directly switchable plasmonic nanoantenna made from phase change materials.

Our fundamental building block for our electrically switchable plasmonic nanoantennas is an electrochemically driven metal-to-insulator transition of our used polymer PEDOT:PSS. It has excellent electrical and optical properties as shown in Figure 2.9, where the real part  $\epsilon_1$  (a) and imaginary part  $\epsilon_2$  (b) of the dielectric function  $\epsilon = \epsilon_1 + i\epsilon_2$  of PEDOT:PSS are depicted. The metallic and insulating state are illustrated in red and blue, respectively. The inset in the middle of Figure 2.9 illustrates the redox reaction occurring when PEDOT:PSS changes from its neutral (insulating) state to its oxidized polaronic/bipolaronic (metallic) state. In detail, PEDOT:PSS is alternately oxidized and reduced, as common in electrochemistry. Thus, applying the respective voltages of +1 V and -1 V (vs. a reference electrode) causes a doping and dedoping of the polymer altering the charge carrier density. Higher voltages (outside our electrochemical po-



tential window) will cause an over-doping and degradation of the material.

We find that PEDOT:PSS is switchable between metallic ( $\epsilon_1 < 0$ ) and insulating ( $\epsilon_1 > 0$ ) for wavelengths larger than  $1.3 \mu\text{m}$  via the applied voltage. The crossing  $\epsilon_1 = 0$  defines the plasma frequency  $\omega_p$  of our polymer. As explained in section 2.2.2, the plasma frequency gives direct feedback where a material turns optically metallic allowing for localized plasmonic resonances. From the expression of the plasma frequency (eq. 2.14)

$$\omega_p = \sqrt{\frac{n_\rho e^2}{\epsilon_0 m^*}} \quad (2.36)$$

it becomes apparent that a change of  $\omega_p$  for metallic polymers is possible via a variation of the (semi-)free charge carrier density  $n_\rho$ . The plasma frequency of our metallic polymer ( $\lambda_p = 1.3 \mu\text{m} \rightarrow \omega_p = 230.6 \text{ THz}$ ) corresponds to a charge carrier density of

$$n_\rho = 1.67 \times 10^{19} \text{ cm}^{-3}. \quad (2.37)$$

Thus, a further increase of  $n_\rho$  by utilizing, e.g., ultra-high doping levels in metallic polymers will allow, in the future, to push the plasma frequency of metallic polymers even into the visible wavelength range. One benefit of using PEDOT:PSS as commercially available polymer is that the dielectric function of the pristine spin-coated material is nearly identical to the fully oxidized metallic state. Thus, even without any applied voltage, the plasmonic properties of the metallic polymer are fully accessible.

#### 2.4.2 Resonance Tuning

The polymer nanoantennas from the metallic polymer are obtained via the fabrication route explained in section 2.3.1. SEM images and plasmonic resonances of the resulting well-defined metallic polymer nanoantennas are shown in Figure 2.10 on the right. The spectral characterization of the polymer nanoantennas is carried out in transmission with a Fourier-transform infrared (FTIR) spectroscopy system (Bruker Vertex 80 with Hyperion 3000 microscope). We use bare glass substrates covered with 20 nm of ITO as reference. The pristine polymer nanostructures show well-modulated plasmonic resonances. Figure 2.10a and b illustrate the resonances for excitation with TM and TE polarized light, respectively. The TM peak wavelength is tunable in the NIR and MIR spectral range via a length variation. While a nanoantenna length of  $L = 180 \text{ nm}$  leads to a TM plasmonic resonance around  $\lambda = 1.9 \mu\text{m}$ , an increase to  $L = 380 \text{ nm}$  shifts the mode to  $\lambda = 2.6 \mu\text{m}$  with a significant modulation of close to 40% in transmission. In

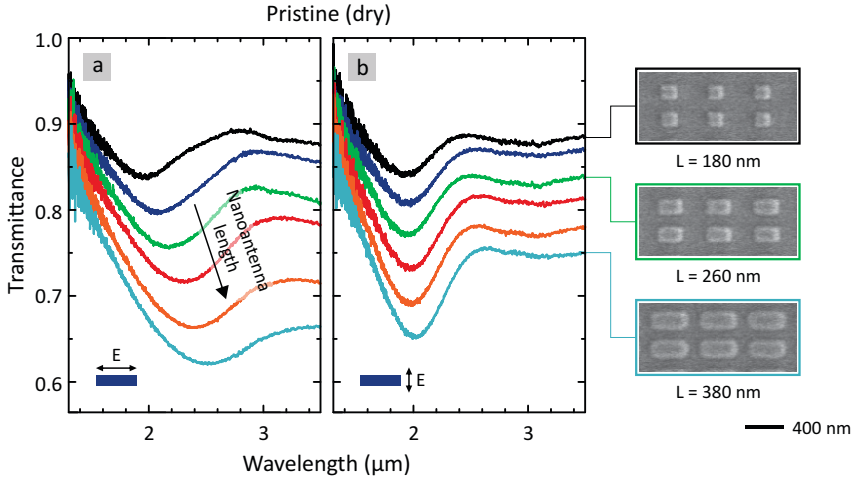


**FIGURE 2.10. Optical tunability of plasmonic nanoantennas made from metallic polymers.** Plasmonic resonances as well as a selection of scanning electron microscopy (SEM) images of pristine (dry) polymer nanoantennas. We obtain close to 40% modulation in transmittance. (a) The plasmonic resonances (transverse magnetic (TM) modes) are tunable from a peak wavelength of  $1.9 \mu\text{m}$  to  $2.6 \mu\text{m}$  when varying the length of the nanoantennas from  $L = 180 \text{ nm}$  to  $L = 380 \text{ nm}$ . The width is  $180 \text{ nm}$ , the height is  $90 \text{ nm}$ , the periodicity in  $x$  and  $y$  is  $500 \text{ nm}$  and  $300 \text{ nm}$ , respectively. (b) The transverse electric (TE) plasmonic resonances does not shift notably in resonance position, yet, the modulation depth increases strongly.

contrast, the TE plasmonic resonance peaks at  $\lambda = 2.0 \mu\text{m}$  (Figure 2.10b) and does not shift notably in wavelength with an increase of the nanoantenna length. The modulation depth increases from 5% to more than 30% as the width of the antennas is kept constant.

For comparison we use CST Microwave Studio to simulate the spectral response of the metallic polymer nanoantennas. The results for TM and TE polarization are depicted in Figure 2.11. We use the dielectric function of PEDOT:PSS shown in Figure 2.9. The simulation agrees qualitatively very well with the experiment in Figure 2.10, yet the modulation depth is over-estimated by a factor of 1.5 to 2.0. While the simulation predicts a modulation depth of approximately 60% for metallic polymer nanoantennas with a length of  $380 \text{ nm}$ , the experiment shows only 40%. In addition, also the overall TM resonance shift for a length variation is larger in the simulation in

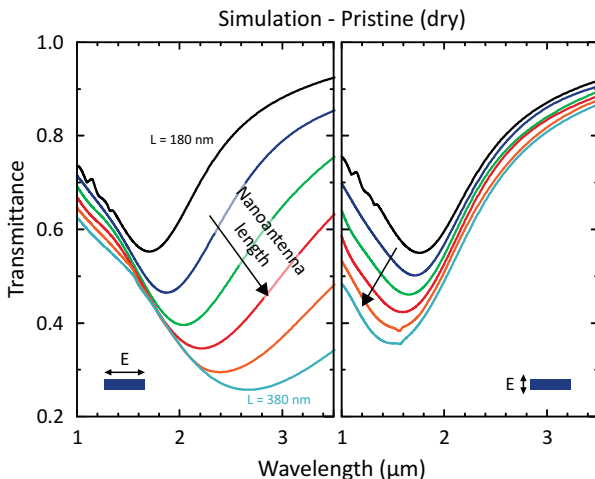


FIGURE 2.11. **Simulation of pristine plasmonic nanoantennas from metallic polymer.** Plasmonic resonances of simulated metallic polymer nanoantennas illuminated with a (a) TM and (b) TE polarized electromagnetic wave. Simulation is performed with CST Microwave Studio. The TM plasmonic resonances are tunable from a peak wavelength of  $1.8 \mu\text{m}$  to  $2.8 \mu\text{m}$  when varying the length of the nanoantennas from  $L = 180 \text{ nm}$  to  $L = 380 \text{ nm}$ . The width is  $180 \text{ nm}$ , the height is  $90 \text{ nm}$ , the periodicity in  $x$  and  $y$  is  $500 \text{ nm}$  and  $300 \text{ nm}$ , respectively.

comparison to the experiment.

Overall, we have demonstrated so far very good plasmonic properties of polymer nanoantennas with a tunability of the plasmonic resonances in the NIR and MIR spectral range while achieving remarkable resonance modulation comparable to nanoantennas made from commonly used plasmonic metals such as gold or aluminum. However, the key advantage is the electrical switchability of our plasmonic polymer nanoantennas which we will discuss in the following.

### 2.4.3 Electrical Switching of Plasmonic Resonances

As explained in section 2.3.2, the electrical switching is carried out in a liquid environment using an electrochemical cell with a three-electrode setup as sketched in Figure 2.12. ITO (for electrical contact) and the polymer nanoantennas serve directly as the working electrode, whereas the counter electrode (platinum wire) and the reference electrode (silver/silver-chloride, Ag/AgCl) are in contact with the electrolyte

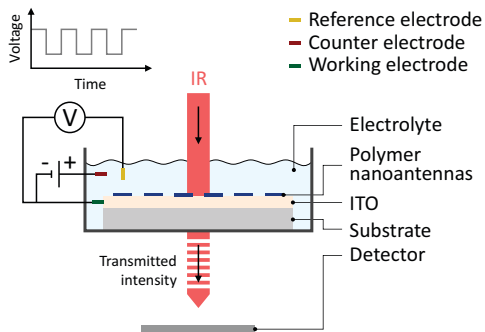


FIGURE 2.12. **Electrochemical switching principle.** Schematic drawing of the electrochemical cell and optical measurement setup where the optical properties of the polymer nanoantennas are electrically controlled and investigated. We use a three-electrode setup with potentiostat to apply the corresponding voltages to the polymer nanoantennas.

(0.1 mol/l TBAPF<sub>6</sub> in Acetonitrile). A potentiostat is used to control the individual voltage over time. The voltage is given versus reference potential, i.e. PEDOT:PSS is in its oxidized state at +1 V and in the neutral (reduced) state at -1 V vs. Ag/AgCl. It must be noted that upon electrochemical doping counterions are incorporated in the active nanoantennas for charge balancing reasons. The electrochemical window is chosen such that no overdoping takes place. For the full spectral characterization of the polymer nanoantennas we use an FTIR spectrometer. The temporal and switching behavior is investigated with a narrow band IR laser and a photodiode, as discussed later below.

The spectral response of an array of polymer nanoantennas with length  $L = 300$  nm for different applied voltages is depicted in Figure 2.13. The pristine spectral response (referred to as dry state without electrolyte) as well as the response for +1 V are shown in grey and red, respectively. For the chosen nanoantennas ( $L = 300$  nm, SEM image on the right in Figure 2.13), we find in the dry state a plasmonic resonance around a wavelength of approximately  $2.4 \mu\text{m}$ . The PEDOT:PSS is in an almost completely oxidized state, causing a well-modulated plasmonic resonance. An applied voltage of +1 V triggers a full oxidation of PEDOT:PSS with a maximum doping level and charge carrier density of the polymer due to the existence of polarons/bipolarons [66, 67]. This results in the plasmon in Figure 2.13 to be fully turned ON with the highest possible modulation. The peak wavelength shifts slightly blue with a peak wavelength of approximately  $2.2 \mu\text{m}$ . Remarkably, applying a negative potential of -1 V (Figure 2.13,

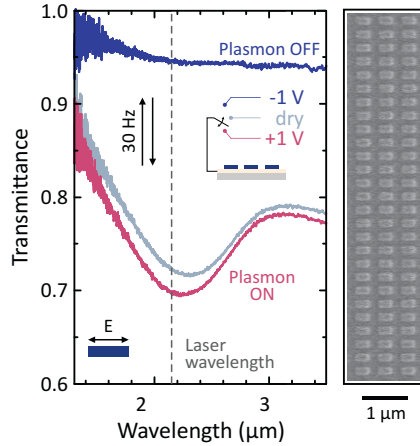


FIGURE 2.13. **Electrical switching of plasmonic resonance.** Spectral response of polymer nanoantennas ( $L = 300$  nm) for different states. Dry state (grey, pristine without electrolyte): The plasmonic resonance is almost completely turned ON with a peak wavelength of  $2.4 \mu\text{m}$ .  $+1$  V (red): The plasmonic resonance is completely turned ON with the highest possible modulation and is slightly blue-shifted to  $2.2 \mu\text{m}$  as the polymer is in its fully metallic state.  $-1$  V (blue): The plasmonic resonance is completely turned OFF as the polymer turned insulating. All voltages are measured against Ag/AgCl. Right panel: A SEM image shows the nanoantennas with a length of  $300$  nm. The laser wavelength for the experiments in Figures 2.15 to 2.17 is marked in grey (dashed line).

blue curve) turns the plasmon in the polymer nanoantennas completely OFF with no remaining plasmonic modulation - PEDOT:PSS is completely reduced, i.e. in the neutral state and hence dielectric in the IR spectral range of interest.

Furthermore, we plot in Figure 2.14 an entire data set of spectral responses from polymer nanoantennas with different lengths. Here, we vary the length from  $160$  nm to  $380$  nm. The length step size is  $20$  nm. The width at  $160$  nm, the periodicity in  $x$  at  $500$  nm, and the periodicity in  $y$  at  $300$  nm are kept constant for all lengths. Figure 2.14 includes a detailed investigation of the plasmonic resonances for TM and TE polarization as well as for the following three different states: dry (pristine),  $+1$  V,  $-1$  V. It is observed that the plasmonic resonances of all arrays of polymer nanoantennas can be completely switched off (TM and TE resonances) which proves the great tunability and switchability of our metallic polymer nanoantennas.

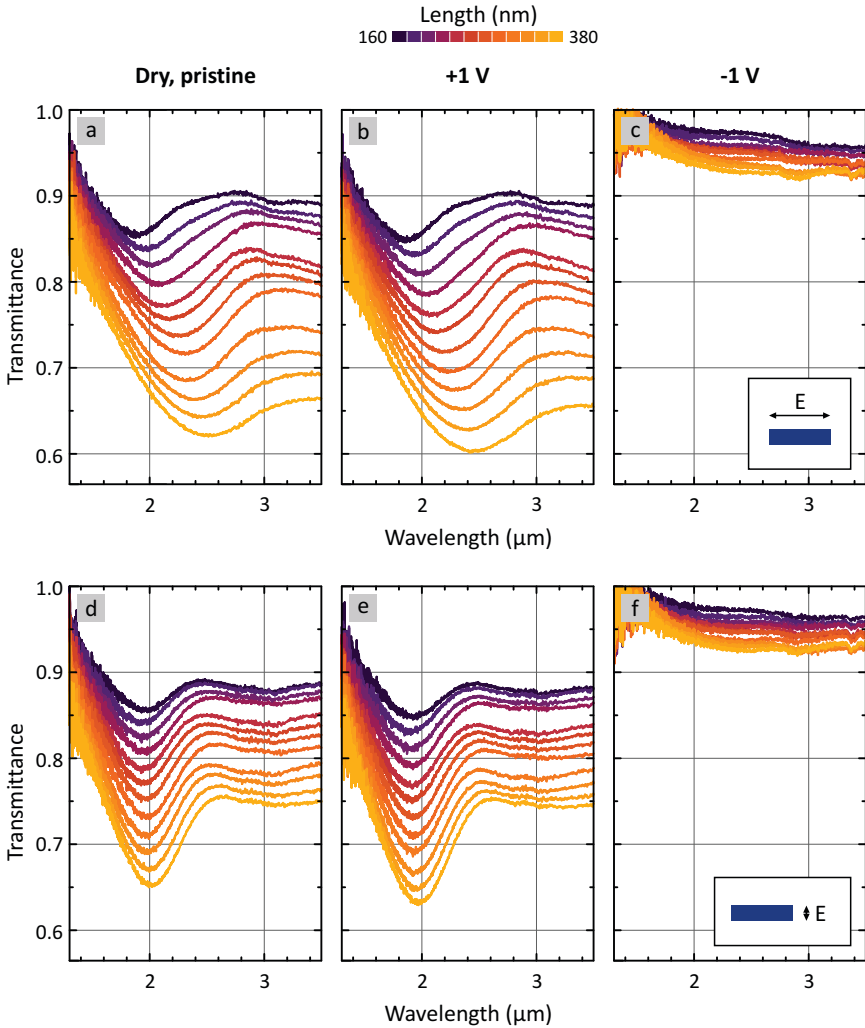


FIGURE 2.14. **Entire spectral data of electrically switchable plasmonic nanoantennas made from metallic polymers.** Length variation (160 nm - 380 nm) for different polymer states (dry state, +1 V, -1 V) and different incident linear polarization. **TM-polarized:** (a) dry, (b) +1 V, (c) -1 V. **TE-polarized:** (d) dry, (e) +1 V, (f) -1 V. The width of the plasmonic nanoantennas is 160 nm, the periodicity is 500 nm along the long axis and 300 nm along the short axis. The plasmonic resonances for all lengths can be further enhanced at an applied voltage of +1 V and can be completely switched off at -1 V. This results in a maximum switching difference of approximately 35% in transmittance (compare (b) and (c)).

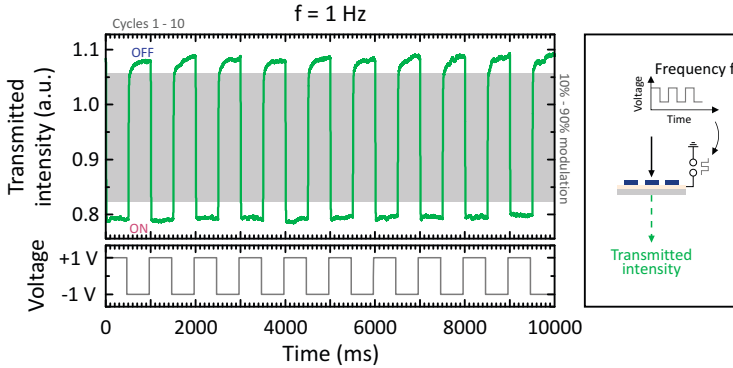


FIGURE 2.15. **Electrical switching with 1 Hz frequency.** Transmitted intensity at  $\lambda = 2.15 \mu\text{m}$  through the polymer nanoantennas while the applied voltage is switched, as sketched on the right. The intensity of the transmitted beam is modulated according to the state the polymer nanoantennas are set to with the applied voltage. The lower graphs show the set voltage switching between +1 V and -1 V. The top graphs depict the transmitted intensity (green curve) cycling between the ON and OFF state as well as the 10% - 90% modulation (grey areas). We plot the cycles 1-10 where the polymer nanoantennas are switched with a frequency of  $f = 1 \text{ Hz}$ .

#### 2.4.4 Switching Speed

As a next step we investigate the switching speed of our metallic polymer nanoantennas. We present in Figure 2.15 the transmitted intensity through the metallic polymer nanoantennas while the antennas are switched between ON and OFF states at applied voltages of +1 V and -1 V, respectively. This causes the intensity of the transmitted laser beam - fixed to a wavelength of  $2.15 \mu\text{m}$  - to be modulated, as sketched on the right in Figure 2.15. The lower graphs (grey curves) show the voltage applied to the polymer nanoantennas cycling between +1 V and -1 V. The corresponding transmitted intensity through the polymer nanoantennas is depicted in the top graphs (green curves). The first ten cycles of the electrical polymer nanoantenna switching with a frequency of  $f = 1 \text{ Hz}$  are shown. We find full transitions between the ON and OFF states without any noticeable degradation.

This allows for the extraction of the 0% and 100% modulation level, meaning the intensity values reached in the saturated ON and OFF state, respectively, as it is depicted in Figure 2.16 on the left. It shows the rise and fall curve of the first cycle of electrical switching with 1 Hz. The rise curve (upper graph) defines the 100% level

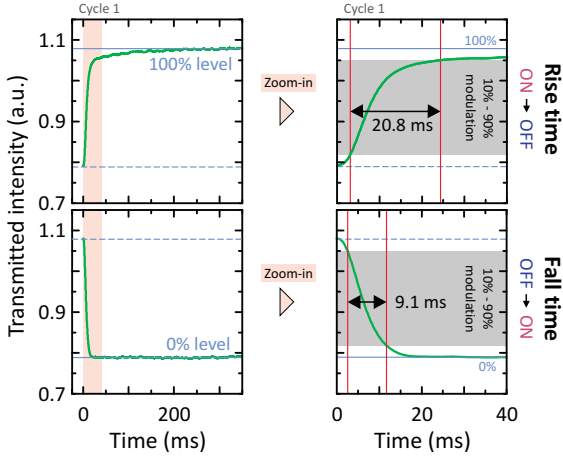


FIGURE 2.16. **Extraction of switching time.** Detailed analysis of rise (ON  $\rightarrow$  OFF) and fall (OFF  $\rightarrow$  ON) time. Left: Determination of 0% and 100% level of switching cycles. Rise and fall curve of first cycle of electrical switching of plasmonic nanoantennas shown in Figure 2.15. We determine the 100% level (top) and 0% level (bottom) from the rise and fall curve, respectively, when saturation is achieved. Right: Zoom-in on the first 40 ms (orange area) of the first switching cycle of the respective rise and fall curve. The grey area marks the 10% - 90% modulation to determine the rise/fall time. We obtain a rise time (from 10% to 90%) of  $\tau_{\text{rise}} = 20.8$  ms and a fall time (from 90% to 10%) of  $\tau_{\text{fall}} = 9.1$  ms as marked in red.

after the intensity has saturated, as marked in blue. The 0% is defined by the fall curve after saturation (lower graph). Consequently, we can define and calculate the 10% - 90% modulation window (marked as grey area). For this purpose, a zoom-in on the first 40 ms (orange area) of the rise / fall curve is displayed in Figure 2.16 on the right. We analyze the rise time (ON  $\rightarrow$  OFF) in the top graph as well as the fall time (OFF  $\rightarrow$  ON) in the lower graph. The rise time is commonly defined as the time step in which the intensity rises from 10% to 90%. Equivalently, the fall time is defined as the time step in which the intensity falls from 90% to 10%. The respective time span is marked in red. We obtain a rise time of  $\tau_{\text{rise}} = 20.8$  ms and a fall time of  $\tau_{\text{fall}} = 9.1$  ms. This results in a total time for one duty cycle of  $\tau = 29.9$  ms, equivalent to a maximum switching frequency of  $f = 33$  Hz.

30 cycles of an electrical switching of our plasmonic polymer nanoantennas with video-rate frequency of  $f = 30$  Hz is depicted in Figure 2.17. Again, the 10% - 90%



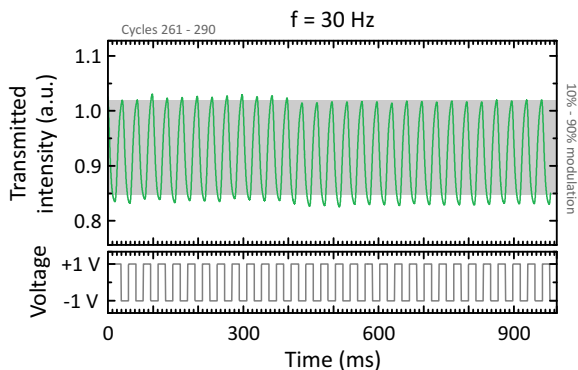


FIGURE 2.17. **Electrical switching with video-rate frequency.** Transmitted intensity at  $\lambda = 2.15 \mu\text{m}$  through the polymer nanoantennas while the applied voltage is switched with a frequency of  $f = 30 \text{ Hz}$ . The lower graphs show the set voltage switching between +1 V and -1 V. The top graphs depict the transmitted intensity (green curve) cycling between the ON and OFF state as well as the 10% - 90% modulation (grey areas, taking degradation into account). We plot the cycles 261-290 where the polymer nanoantennas are switched with a frequency of  $f = 30 \text{ Hz}$ . We reach more than a 10% - 90% modulation even at these video-rate switching frequencies.

modulation window is marked as grey area, which takes degradation of the nanoantennas after a total of 260 cycles into account. We find that indeed electrical switching at such high video-rate frequencies is possible as the transmitted intensity reaches a modulation larger than 10% - 90%. Overall, the degradation after 290 switching cycles is on the order of only 25%, which means that the overall modulation (comparison of grey marked areas in Figures 2.15 and 2.17) is reduced by 25%. For switching at 1 Hz, we find little to no degradation within the first 20 cycles. Possible sources for degradation might be the volume expansion of the polymer during switching (causing nanoantennas to become porous), or irreversible reactions during the electrochemical oxidation and reduction. However, future material development can even improve the long-term stability.

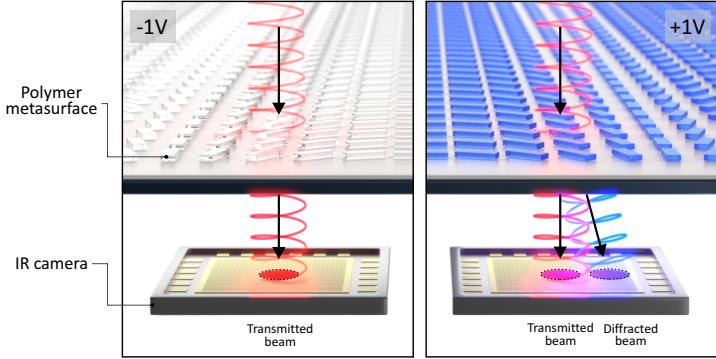


FIGURE 2.18. **Concept of metallic polymer plasmonic metasurface for high-efficiency active beam steering.** A plasmonic metasurface made from metallic polymer is switchable between an insulating (left) and metallic state (right) by applying a voltage of  $-1$  V and  $+1$  V, respectively. This turns the polymer metasurface from an OFF- into an ON-state and allows beam steering (using incident circularly polarized light) with 100% contrast ratio in the diffracted beam. The polymer metasurface consists of an array of individually rotated plasmonic nanoantennas.

## 2.5 METALLIC POLYMER METASURFACE FOR DYNAMIC BEAM STEERING

Our novel concept greatly boosts the integrability of plasmonic systems into, e.g., commercial smart and small-scale electro-optical devices, as we have demonstrated that it possesses several favorable properties: It has a very high switching modulation efficiency with a full ON- and OFF-state, it is electrically switchable, it requires comparably low voltages/electric potentials, and it is switchable at video-rate frequencies. One archetype integration of plasmonics into devices is performed via plasmonic metasurfaces. State-of-the-art nanofabrication offers full control over spatial arrangement and orientation of the subwavelength nanoresonators and thus allows to design metasurfaces with amplitude and phase manipulation as well as control of light nearly at will. Thus, as a proof of concept, we demonstrate an electrically switchable metallic polymer metasurface for ultra-high-contrast active beam steering, that is, a metasurface with the ability to actively control the routing of incident light into a fixed angular range. The basic working principle is illustrated in Figure 2.18: The metasurface is illuminated with a circularly polarized light beam. Depending on the state of the polymer nanoantennas, part of the incident light is diffracted, showing opposite hand-

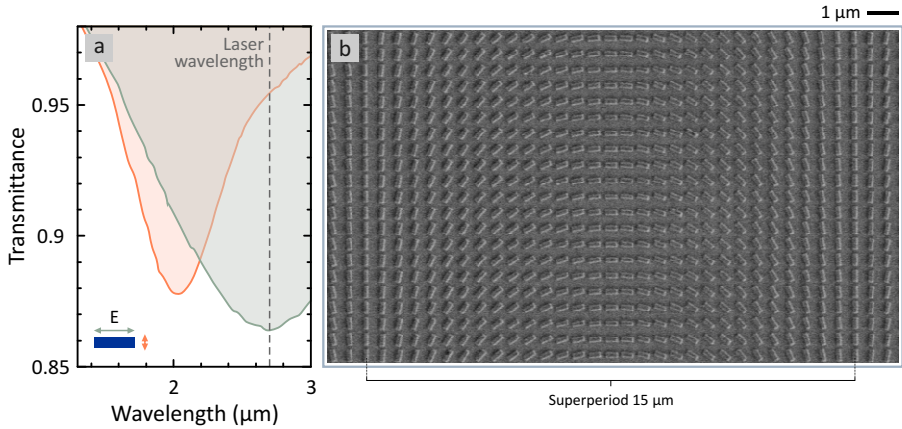


FIGURE 2.19. **Spectra and SEM image of the metallic polymer beam steering metasurface.** (a) The TM plasmonic resonance (dark green) has a peak wavelength at  $2.65 \mu\text{m}$  which is used as illumination wavelength in Figure 2.20. The TE resonance (orange) is shifted to  $2.0 \mu\text{m}$ , to realize sufficient spectral contrast between TE and TM resonance at the operating wavelength of  $2.65 \mu\text{m}$ . The superperiod of the polymer metasurface is  $15 \mu\text{m}$  leading to a diffraction angle of  $\varphi = 10.2^\circ$ .

edness. The transmitted and diffracted beams are imaged with an IR camera. The key feature of our metallic polymer metasurface is the ability to fully switch it ON and OFF. Consequently, the contrast ratio, defined as the ratio of the diffracted intensities in the metasurface ON and OFF states, reaches an unprecedented 100%.

The TM (dark green) and TE (orange) resonance spectra of the metallic polymer nanoantennas, building blocks of the metasurface, are depicted in Figure 2.19a. The peak wavelength of the TM plasmonic resonance is at  $2.65 \mu\text{m}$ , whereas the TE peaks at  $2.0 \mu\text{m}$ . It results in sufficient spectral contrast between TE and TM polarization. This is necessary for the geometric rotation to cause a geometric  $\pi$ -phase shift (Pancharatnam-Berry-phase) after  $180^\circ$  nanoantenna rotation, when the metasurface is illuminated with circularly polarized light. This causes nanoantennas spaced by the superperiod to oscillate and scatter light efficiently in phase with opposite handedness of the circular polarization [7]. The length of the individual nanoantennas is  $380 \text{ nm}$ , the width is  $160 \text{ nm}$ , and the height is  $90 \text{ nm}$ . Incremental rotation angles of  $6^\circ$  with a periodicity of  $500 \text{ nm}$  in  $x$  and  $y$  direction result in a superperiod of  $15 \mu\text{m}$ , as illustrated in the SEM image of the polymer metasurface in Figure 2.19b. It comprises a total of 30 individual

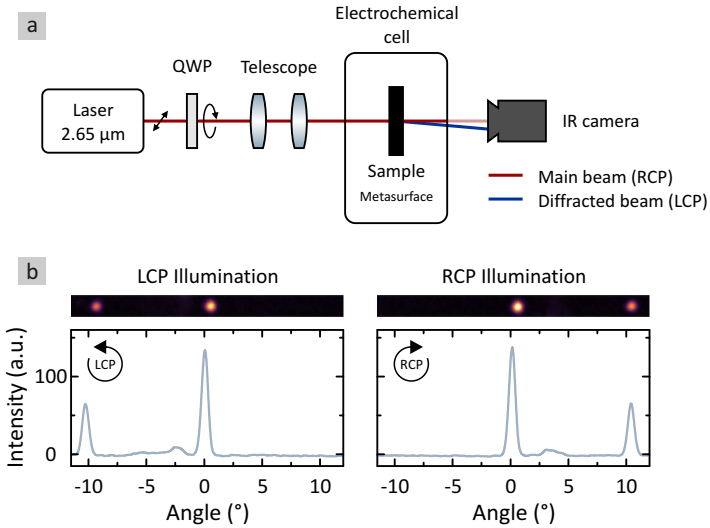


FIGURE 2.20. **Pristine beam diffraction with polymer metasurface.** (a) Experimental setup to measure and image beam steering with the electrically switchable metallic polymer metasurface. (b) IR camera image and intensity profiles for an illumination with left-circularly polarized (LCP) (left) and right-circularly polarized (RCP) (right) light. The primary beam at  $0^\circ$  remains for both circular polarized states, whereas the diffracted beam appears at  $-10.2^\circ$  for LCP and at  $+10.2^\circ$  for RCP illumination.

polymer nanoantennas, leading to a diffraction angle of  $\varphi = 10.2^\circ$ .

In order to measure and image the diffraction of the beam steering metasurface, we use a home-built setup as sketched in Figure 2.20. We use a tunable parametric frequency converter system (Alpha-HP, Stuttgart Instruments) for the laser illumination tuned to  $\lambda = 2.65 \mu\text{m}$ . As the laser is linearly polarized, a subsequent quarter wave plate (QWP) is used to obtain circularly polarized light. A telescope, comprising two lenses, is used to adjust the beam diameter. We illuminate with a collimated light beam. The polymer metasurface is placed inside the electrochemical cell for electrical switching and causes the incident beam (red) to be diffracted (blue) when the metasurface is in its metallic state. Both beams are detected and imaged using an IR camera (Pyrocam III, Ophir Photonics).

The functionality of the polymer metasurface in its pristine state is depicted in Figure 2.20b. For these measurements, there is no voltage applied to the metallic

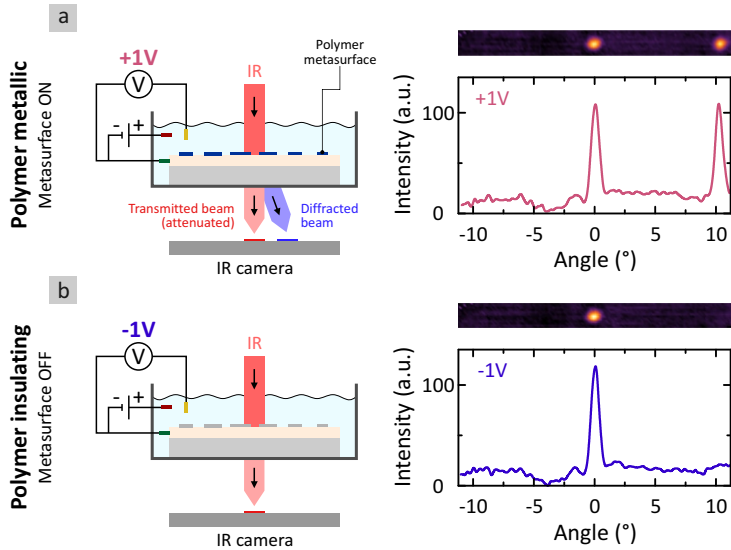


FIGURE 2.21. **High contrast beam steering with metallic polymer metasurface.** Left: Schematic drawing of the measurement setup and beam steering concept of the polymer metasurface. The metasurface is turned ON and OFF via the applied voltage (three-electrode setup) in the electrochemical cell, while the transmitted and diffracted beams are recorded using an IR camera. Right: IR camera images and intensity profiles in the (a) ON- and (b) OFF-state for illumination with RCP light. The diffracted beam (right peak) at  $+10.2^\circ$  vanishes completely when a voltage of  $-1$  V is applied.

polymer nanoantennas. The top images illustrate the IR camera images for LCP (left) and RCP illumination (the primary transmitted beam is attenuated to prevent saturation of the IR camera). The bottom graphs show the averaged intensity versus the diffraction angle. The primary (non-diffracted) transmitted beam at an angle of  $0^\circ$  has similar intensities for both illumination polarizations. For illumination with LCP light, we observe a diffracted spot at  $-10.2^\circ$ . As expected, when inverting the polarization to RCP, the incident laser beam is diffracted in opposite direction and appears at  $+10.2^\circ$ . The diffraction efficiency is 1.1%. So far, the spectral contrast of the beam-steering metasurface in its ON-state accounts to roughly 86:100 percent transmission (see Figure 2.19a, TM mode, dark green curve). This contrast is currently limiting the diffraction efficiency. Increasing the modulation depth by optimizing material, geometry, and doping levels will enhance the diffraction efficiency.

The electrical switching of the metallic polymer metasurface is carried out analogously to Figure 2.12 in the electrochemical cell. As mentioned, the laser is set to an illumination wavelength of  $2.65 \mu\text{m}$  and the IR camera is used to image the transmitted and diffracted intensities. The incident light beam is RCP. The experimental scheme is sketched in Figure 2.21a and b on the left. The measured IR camera images and intensity profiles for an applied voltage of +1 V and -1 V are displayed on the right (please note that the primary transmitted beam is again attenuated to prevent saturation of the IR camera). A voltage of +1 V turns the metasurface ON. The polymer is fully oxidized leading to the known metallic plasmonic properties. We observe diffraction by the plasmonic polymer metasurface. In contrast, the applied voltage of -1 V turns the metasurface completely OFF as the polymer nanoantennas switch into the insulating state. As seen in Figure 2.21b on the right, the diffracted beam at  $+10.2^\circ$  vanishes completely as the plasmonic properties of the individual polymer nanoantennas are switched OFF.

The metallic polymer nanoantennas possess another intriguing property: A successive electrochemical doping allows to realize intermediate states between ON and OFF and thus a modification of the intensity of the diffracted beam at will. This is depicted in Figure 2.22a. We show selected IR camera images of a total of three cycles of this active beam steering process, where the voltage is cycled between  $\pm 1$  V. The scan rate is 20 mV/s. Typical cyclic voltammograms are depicted in Figure 2.22b. While the primary beam (a) remains almost constant for all voltages, the intensity of the diffracted beam can be gradually varied until a full turn OFF and ON is achieved.

The images illustrate another important aspect of our material: There is a hysteresis present, both in the cyclic voltammogram (Figure 2.22b) as well as in the optical signal (diffracted intensity as a function of applied voltage, Figure 2.22c). This has an important and extremely useful consequence: At voltage zero, depending on the direction of the scan (either going from +1 V to 0 V or going from -1 V to 0 V), the diffracted optical signal will be different. Thus, non-volatile operation is possible, which means that for future holographic and display applications the diffraction of the nanoantennas of the metasurface can be set ON or OFF in a powerless operation. This concept will be used in the next section to realize an entire non-volatile metaobjective from metallic polymer metalenses-on-demand.

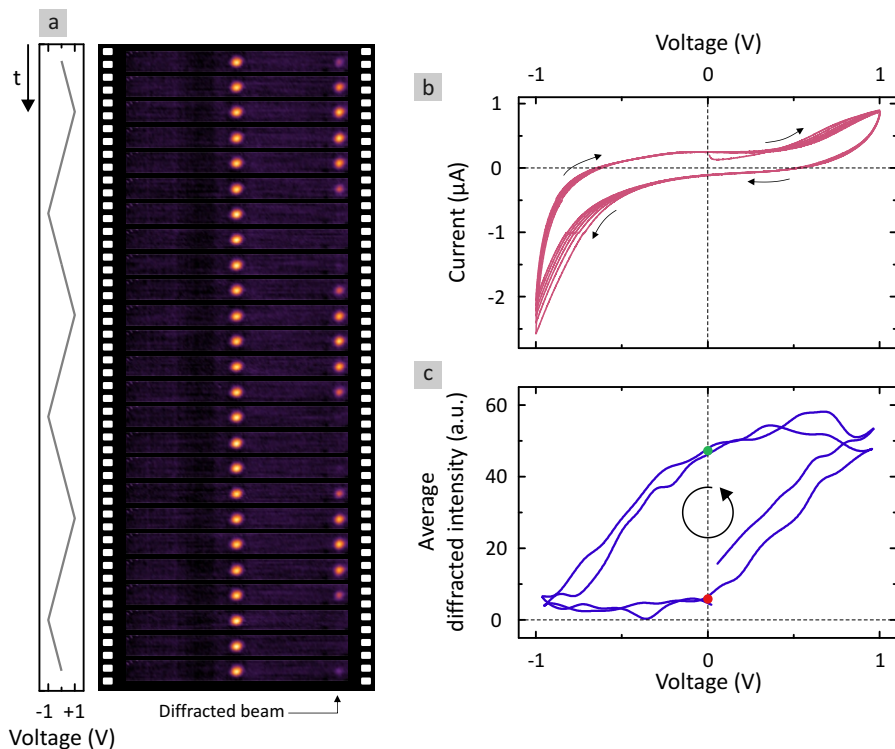


FIGURE 2.22. **Continuous active beam steering with metallic polymer metasurface.** (a) Chosen subsequent IR camera images showing three cycles of active beam steering when the applied voltage is cycled in-situ between -1 V and +1 V. The intensity of the diffracted beam (right spots) can be continuously varied depending on the applied voltage. (b) Cyclic voltammograms for metallic polymer metasurface from PEDOT:PSS during electrochemical switching. Measured current against applied voltage (vs. Ag/AgCl) for six cycles of electrical switching of the metasurface. The arrows indicate the scanning direction. (c) Average diffracted intensity vs. applied voltage of the metasurface switching shown in (b). We find a hysteresis of the optical signal. Depending on the direction of the voltametric scan, we can hold the metasurface in different states in a powerless operation at 0 V. A scan from +1 V to 0 V results in an ON-state of the metasurface with a high diffracted intensity (green dot). A scan from -1 V to 0 V results in an OFF-state with no diffraction (red dot). The scan direction is again indicated with the arrow.

## 2.6 ELECTRO-ACTIVE METAOBJECTIVE FROM METALENSES-ON-DEMAND

Switchable and active metalenses are of interest for the miniaturization and for extending the functionality of complex and integrated on-chip imaging systems. Typically, bulky lenses or mechanically adjustable zoom-objectives are necessary, while active metalenses allow similar adjustments to, e.g., the focal length on ultra-small length scales without any required mechanical adjustment. In detail, the active switching of metalenses relies on the change of the optical properties of the used materials upon an external stimulus. Most prominent, these transitions are either driven by temperature [16, 17, 43], chemically [41, 42, 44–47], or electrically [10, 18, 49–51, 54, 56, 68], with the latter being the most desirable for electro-optical devices.

However, most current electro-active approaches of active metalenses do not switch the nanoantenna material itself. In fact, its surrounding material is dynamically altered, thus limiting the achievable switching contrast, functionality, and overall design freedom [18, 20, 21, 69]. In contrast, using nanoantennas from smart functional materials with electrically-driven metal-to-insulator transitions would allow to turn a metalens and thus its functionality fully ON or OFF on demand. In this section, we will demonstrate active metalenses-on-demand and a multi-functional metaobjective composed of electrically switchable metallic polymer nanoantennas. The plasmonic metalenses are switchable between fully ON- and OFF-states via an applied voltage of only  $\pm 1$  V.

### 2.6.1 *Concept*

A schematic of our metallic polymer metalenses and metaobjective is illustrated in Figure 2.23. The objective consists of two independent electrically switchable metalenses (polymer metalens 1 and 2), placed on an ITO coated substrate and separated by an electrolyte. Each metalens comprises plasmonic polymer nanoantennas which are switchable between a metallic and insulating state via applied voltages of +1 V and -1 V, respectively. This is illustrated in the lower part of Figure 2.23. As discussed in the previous sections, the plasmonic resonance of the nanoantennas can be switched fully ON or OFF electrically. The underlying mechanism is again the electrochemically-driven optical metal-to-insulator transition in the metallic polymer PEDOT:PSS. Consequently, an applied voltage of +1 V turns the nanoantenna building blocks into the metallic state and thus the individual metalens into the ON state - the refractive power of the lens is switched ON. A voltage of -1 V turns the metalens and



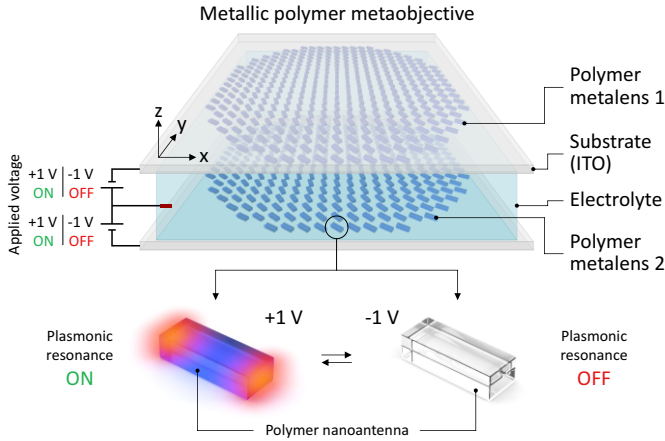


FIGURE 2.23. **Schematics of electro-active metaobjective from metalenses-on-demand.**

Top: Illustration of a metaobjective comprising two electrically switchable metalenses on ITO-covered substrates. The metalenses consist of electrically switchable metallic polymer nanoantennas. An electrolyte is used as separation and to allow electrochemical switching. The refractive power of the polymer metalenses is switched ON or OFF on demand via an applied voltage of only +1 V or -1 V, respectively. Bottom: The electrical switching is based on the reversible metal-to-insulator transition of the metallic polymer. A voltage of +1 V turns polymer nanoantennas metallic and their plasmonic resonance ON. A voltage of -1 V switches the polymer nanoantennas into an insulating state and their plasmonic resonance OFF.

thus the refractive power OFF.

In the combined case of the metaobjective, we obtain four different output states, depending on the voltage applied to the individual polymer metalenses. These multiple states are depicted in Figure 2.24. In Figure 2.24a, metalens 1 is turned ON (+1 V) while metalens 2 is turned OFF (-1 V). Only metalens 1 focuses the incoming collimated light beam. The metaobjective possesses a focal length  $f_1$ . The inverted case in Figure 2.24b (metalens 1: OFF, metalens 2: ON) causes only metalens 2 to focus the incoming light. The metaobjective possesses a focal length  $f_2$ . In the third case (metalens 1: ON, metalens 2: ON) we obtain a unique multi-focal state. Due to the general working principle of the metalenses using circularly polarized light, the two metalenses do not influence each other. Incoming RCP light is focused as LCP light and vice-versa. Thus, both metalenses focus the incoming circularly polarized light separately and we obtain two foci, as depicted in Figure 2.24c. Additionally, the

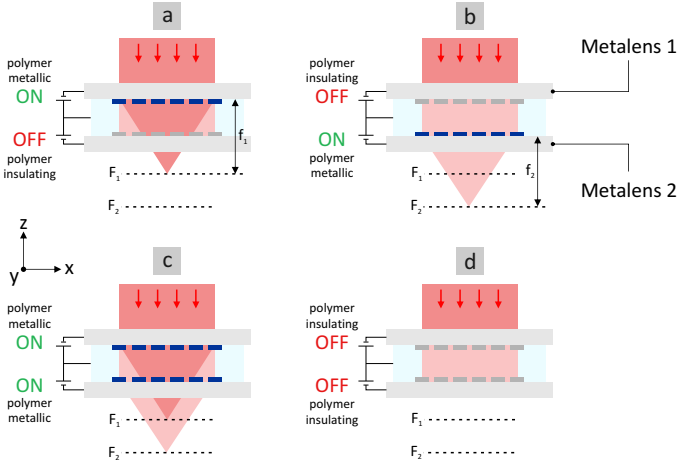


FIGURE 2.24. **Concept of electro-active metaobjective from metalenses-on-demand.** Depending on the individual voltage applied to the polymer metalenses, four different states become possible. (a) (metalens 1: ON, metalens 2: OFF): focus at  $F_1$ . (b) (OFF, ON): focus at  $F_2$ . (c) (ON, ON): focus at  $F_1$  and  $F_2$ . (d) (OFF, OFF): no focus.

metallic polymer metaobjective can also be switched fully OFF. This last case with no focused light in Figure 2.24d results from both metalenses to be switched OFF with an applied voltage of -1 V. Before investigating the metaobjective, we will characterize the following the static as well as dynamic optical properties of the individual metalenses.

### 2.6.2 Static Metallic Polymer Metalens

The functionality and focal length of our metalenses depends on the curvature of the 2D quadratic phase profile, which relies on the geometrical arrangement and individual rotation of the nanoantennas. The rotation angle  $\varphi$  of a nanoantenna at position  $x$  and  $y$  is defined as

$$\varphi(x, y) = \frac{\pi}{\lambda_0} \left( \sqrt{f^2 + x^2 + y^2} - |f| \right), \quad (2.38)$$

where  $\lambda_0$  denotes the free space wavelength and  $f$  the focal length. The phase profile (a) as well as the nanoantenna rotation angle (b) in dependence of the position  $x$  and  $y$  for a metalens with  $f = 5$  mm, a diameter of 1.5 mm, and  $\lambda = 2.65$   $\mu\text{m}$  are depicted in Figure 2.25. It shows a typical quadratic phase profile where the incremental rotation angle decreases towards the center of the metalens. By placing resonant

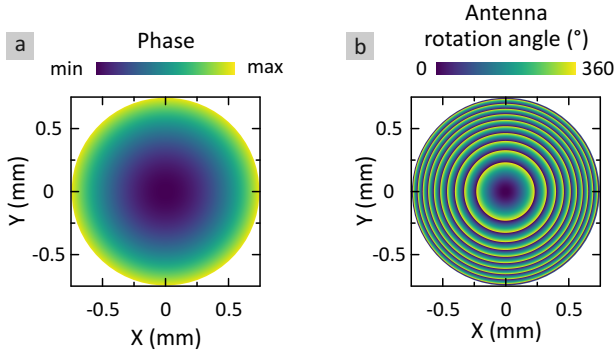


FIGURE 2.25. **Metalens phase profile.** (a) Quadratic phase profile of a metalens with focal length  $f = 5$  mm, diameter of 1.5 mm, numerical aperture of 0.15 at an illumination wavelength of  $\lambda = 2.65 \mu\text{m}$ . (b) 2D map of nanoantenna rotation angle to obtain the quadratic phase profile in (a).

(at  $\lambda = 2.65 \mu\text{m}$ ) metallic polymer plasmonic nanoantennas with the shown rotation angle in an array, one can transfer the quadratic phase profile to the metalens.

A SEM image of a subarea of a metallic polymer metalens is depicted in Figure 2.26a, showing the excellent fabrication quality achievable with spin-coated PEDOT:PSS. As discussed above (Figure 2.9), the plasma frequency/wavelength, which defines the wavelength above which the polymer and thus the nanoantennas become metallic, is around  $\lambda_p = 1.3 \mu\text{m}$ . Consequently, the metallic polymer nanoantennas - the building blocks of the metalenses - exhibit a plasmonic resonance in the IR spectral range, as depicted in Figure 2.26b. The TM resonance position of our used nanoantennas with a length of  $L = 380$  nm, width of  $W = 160$  nm, and height of  $H = 90$  nm is at  $\lambda = 2.65 \mu\text{m}$ , used as working wavelength in all following experiments.

In Figure 2.27a we map the focus of the metallic polymer metalens along the optical axis. The exact measurement setup is depicted in Figure 2.27b. We use a laser (Stuttgart Instruments Alpha HP) tuned to  $2.65 \mu\text{m}$  to be resonant with the plasmonic metallic polymer nanoantennas. Similar to the beam steering metasurface, we rely again on circularly polarized light in order for the metasurface to work (see discussion of Figure 2.19). The laser output is linearly polarized. Using a QWP we obtain RCP (red) light. A telescope reduces the beam diameter to illuminate only the metalenses (diameter 1.5 mm). The metalens/metaobjective is mounted inside an electrochemical cell to facilitate electrical switching. The transmitted (focused) light is polarization

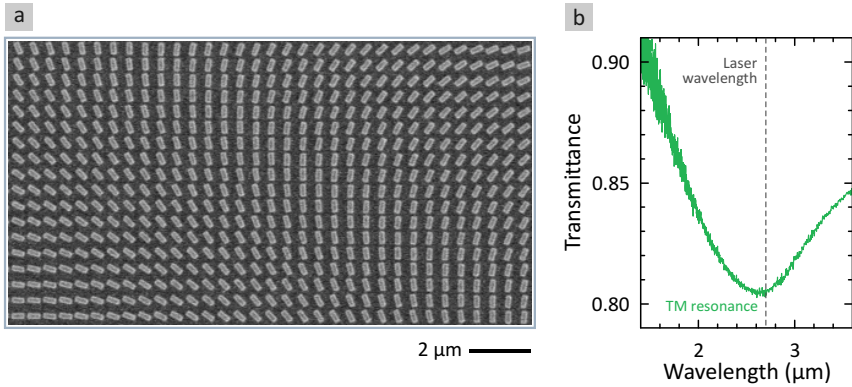


FIGURE 2.26. **SEM image and plasmonic resonance of metallic polymer metalens.** (a) SEM image of a sub-area of the metallic polymer metalens showing the rotated nanoantennas. The nanoantennas have a length of  $L = 380$  nm, width of  $W = 160$  nm, and height of  $H = 90$  nm. The periodicity in  $x$ - and  $y$ -direction is 500 nm. (b) TM plasmonic resonance of used metallic polymer nanoantennas. The working laser wavelength ( $\lambda = 2.65 \mu\text{m}$ ) is marked with a dashed line.

converted and is LCP (blue). The transmitted light is collected and imaged to an IR camera (Spiricon Pyrocam III) using an objective lens. The remaining fundamental RCP light is filtered using a circular analyzer (combination of QWP and polarizer). By moving the entire electrochemical cell along the optical axis in  $z$ -direction, we can map the focus of the metalens/metaobjective. The refractive power of the metalens manifests itself in a focus as depicted in the focal plane of the metalens in Figure 2.27a. The Gaussian beam profile in the focal plane is highly symmetric in both dimensions ( $x$  and  $y$ ). This is proven by a cross-sectional profile along the  $x$ -direction through the focus, as shown in Figure 2.27c. We obtain a focal spot with a FWHM of  $81 \mu\text{m}$  at an illumination wavelength of  $\lambda = 2.65 \mu\text{m}$ .

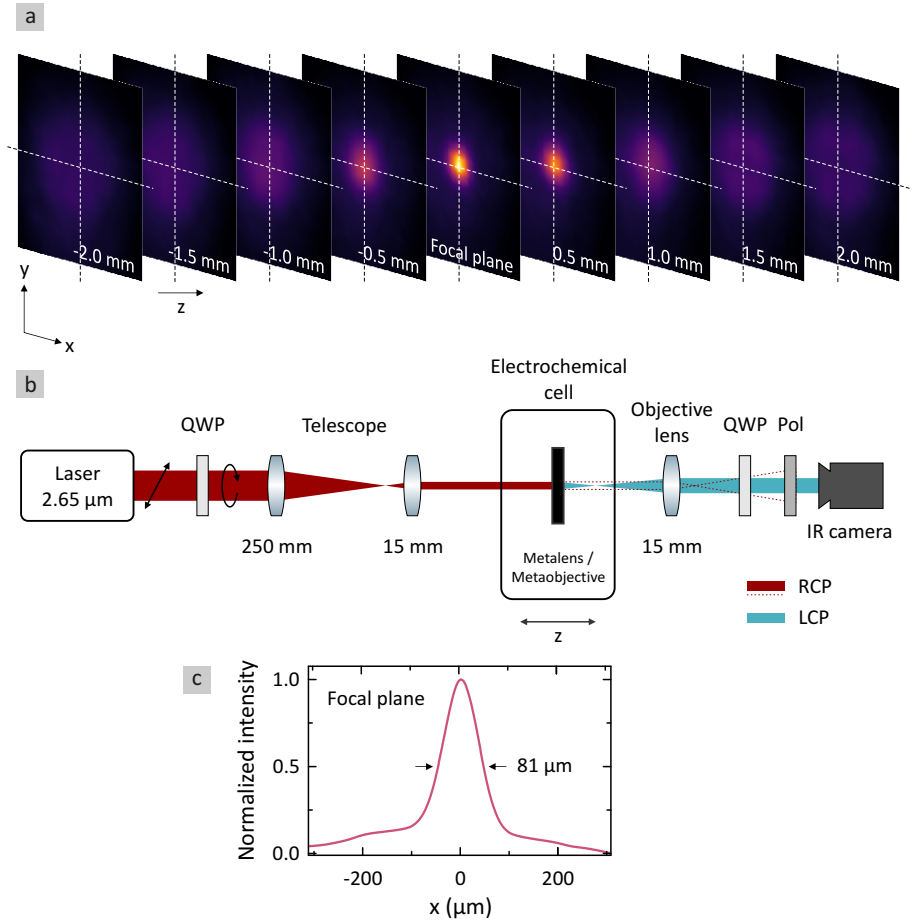


FIGURE 2.27. **Mapping refractive power of polymer metalens.** (a) Camera images at different  $z$ -positions (along the optical axis) around the focal plane of the metallic polymer metalens. (b) Setup to measure and map the focus of the metalenses and the metaobjective. (c) Cross-section of beam profile in the focal plane of the metalens along  $x$ -direction. The full width at half maximum (FWHM) is  $81 \mu\text{m}$ .

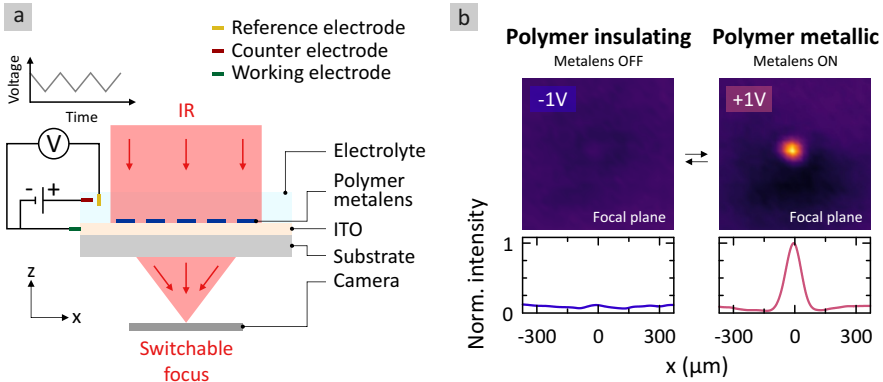


FIGURE 2.28. **High-contrast electrical switching of a metallic polymer metalens-on-demand.** (a) Setup to electrically switch a metalens. An electrochemical three-electrode setup is used to tune the applied voltage via cyclic voltammetry. The camera is placed in the focal plane of the metalens (focal length of  $f = 5$  mm) to image the optical performance of the metalens. (b) Camera images and cross-sectional intensity profiles in the focal plane of the metalens. Left: An applied voltage of  $-1$  V switches the polymer insulating and thus the metalens OFF with no diffractive power. Right: A voltage of  $+1$  V switches the polymer metallic and the metalens ON. A focus is observed.

### 2.6.3 Metalens-On-Demand

Next, we turn our attention to the switching performance of the metallic polymer metalens. The electrical switching is carried out using the previously discussed electrochemical setup in a liquid electrolyte, as it is sketched in Figure 2.28a. It comprises a three-electrode setup including a reference and counter electrode. The polymer metalens itself acts as the working electrode and is contacted via the ITO layer. The applied voltage is cycled between the metallic polymer state at  $+1$  V and the insulating polymer state at  $-1$  V via cyclic voltammetry. Simultaneously, the transmitted intensity and beam profile are imaged using the IR camera positioned in the focal plane of the metalens. Most importantly, we demonstrate in Figure 2.28b that the polymer metalens can be switched between an ON- and OFF-state on demand depending on the applied voltage. A voltage of  $+1$  V turns the plasmonic resonance of the nanoantennas and thus the metalens ON (right). The polymer switches into its metallic state and we observe a focal spot in the focal plane. In contrast, an applied voltage of  $-1$  V turns the plasmonic resonance and the metalens OFF (left). The polymer switches into the insulating state and the refractive power of the metalens is turned OFF. Moreover, this

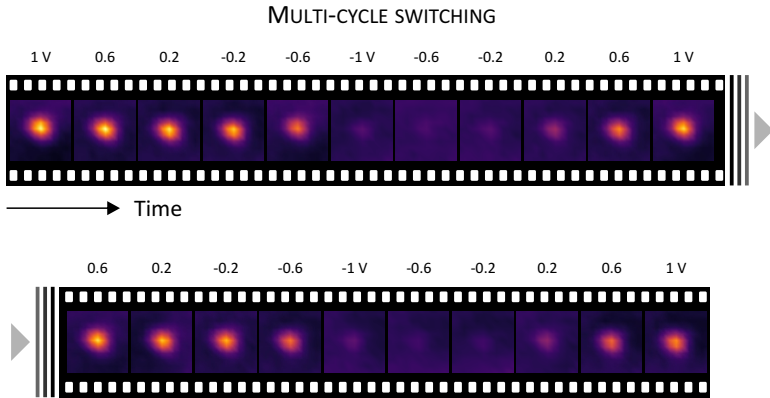


FIGURE 2.29. **Continuous electrical switching of refractive power of metalens.** Time sequence of camera images showing the focused intensity by the polymer metalens while the applied voltage is switched via cyclic voltammetry between  $\pm 1$  V (2 cycles). Grey scale operation is possible as the intensity of the focused light can be adjusted depending on the applied voltage.

electro-optical switching between ON- and OFF-state is reversible and repeatable over hundreds of switching cycles with switching frequencies up to 33 Hz, as previously demonstrated in section 2.4.4.

Selected images of two cycles of electrochemical metalens switching via cyclic voltammetry are depicted in Figure 2.29. The images show the intensity distribution in the focal plane for different applied voltages during the switching cycles. The time axis is from left to right. The scan rate is 20 mV/s. The refractive power of the metalens is reversibly switched ON and OFF. The focused intensity is high at +1 V and low at -1 V. Interestingly, the metalens remains in the metallic ON-state for voltages down to -0.2 V.

This is observable even better in the graph depicted in Figure 2.30. Here, we plot the normalized focused intensity over the applied voltage for the two full cycles. The scanning direction is indicated with arrows. In the backward scan from +1 V to -1 V, we find, that the focused intensity remains almost constant and thus the metalens remains in the ON-state down to voltages of -0.2 V. The intensity fades starting at applied voltages below -0.3 V and the metalens is switched OFF at -1 V. In contrast, in the forward scan from -1 V to +1 V the metalens remains in the OFF-state up to 0 V. From this point the focused intensity increases again until it reaches its maximum

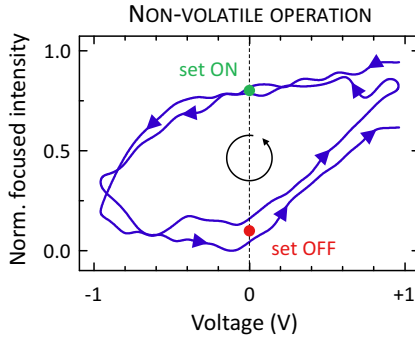


FIGURE 2.30. **Non-volatile operation of metallic polymer metalens.** Normalized focused intensity by the polymer metalens as a function of the applied voltage during the switching cycles shown in Figure 2.30. The scanning direction is marked with arrows. Non-volatile operation is possible at 0 V. The polymer metalens remains in the ON state at 0 V (set ON, marked green) when previously +1 V was applied. In contrast, it remains OFF at 0 V (set OFF, marked red) when previously -1 V was applied.

value around +1 V. Due to this present hysteresis, depending on the preceding applied voltage the metalens can either be set ON or set OFF at 0 V (marked in green and red) and thus an energy-efficient non-volatile operation is possible. This principle is used in the following to switch and set the states of a multi-functional metaobjective comprising two electrically switchable metallic polymer metalenses-on-demand.

#### 2.6.4 *Electro-Active Metaobjective*

The exact electrochemical arrangement to switch the metalenses of the metaobjective is sketched in Figure 2.31. The metalenses are mounted in the same electrochemical cell and their gap is filled with electrolyte. Both use the same reference electrode (Ag/AgCl) and counter electrode (Pt). Using a switches, we can choose which metalens to switch and which voltage to apply with the potentiostat. By closing both switches, we are thus also able to set both metalenses of the metaobjective into the same metallic or insulating state.

The concept of the electro-active polymer metaobjective is sketched in Figure 2.32a. As mentioned, it consists of two metalenses fabricated from metallic polymer, which are separately switchable. The focal lengths are  $f_1 = 6$  mm for metalens 1 and  $f_1 = 5$  mm for metalens 2 and they are spaced by 3.5 mm. Both metalenses comprise nanoan-



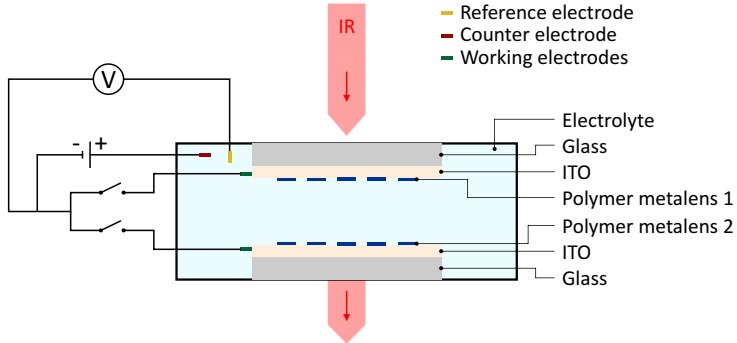


FIGURE 2.31. **Schematic setup to switch the individual metalenses of the metaobjective.** Both polymer metalenses are mounted inside an electrochemical cell filled with electrolyte. We use ITO covered glass substrates to allow electrical addressability and operation in transmittance. Both ITO layers are contacted separately. Using switches, we can choose to which metalens the set voltage is applied to. Furthermore, we can also apply the same voltage to both polymer metalenses simultaneously to set both metalenses to the either ON- or OFF-state.

tennas ( $L = 380$  nm,  $W = 160$  nm,  $H = 90$  nm) resonant at  $\lambda = 2.65$   $\mu\text{m}$ , which is used as the laser illumination wavelength. We use a non-volatile operation (as explained in Figure 2.30) to set the individual states of the two metallic polymer metalenses.

The metaobjective is switchable between four different states. The results are depicted in Figure 2.32b. We plot a cross-section of the  $xz$ -plane which is obtained by moving the IR camera along the optical axis ( $z$ -direction). In the first state (top) metalens 1 is set ON (+1 V) whereas metalens 2 is set OFF (-1 V). Only metalens 1 focuses the incoming circularly polarized light beam and we find a single focus only in the focal plane  $F_1$  at position  $z = 6$  mm. The second state (metalens 1: set OFF, metalens 2: set ON) switches the focal length of the metaobjective and we observe a single focal spot only in the focal plane  $F_2$  of metalens 2 at  $z = 8.5$  mm. Furthermore, we realize two novel states with our metallic polymer metaobjective. Switching both metalenses simultaneously ON via an applied voltage of +1 V creates a multi-focal metaobjective. We obtain focal spots in both focal planes  $F_1$  and  $F_2$ . An applied voltage of -1 V to both polymer metalenses (bottom of Figure 2.32b) sets both metalenses OFF and into the insulating state. The refractive power of the entire metaobjective is switched OFF and no focal spots are observed.

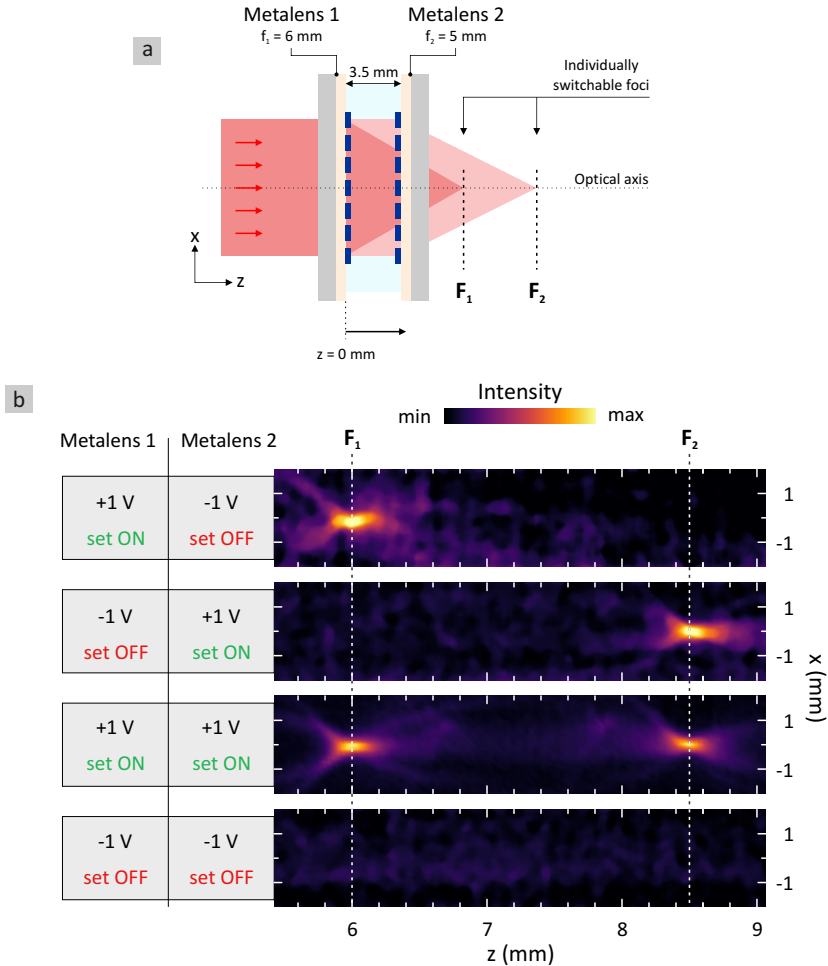


FIGURE 2.32. **Non-volatile electrically switchable multi-functional metaobjective.** (a) Schematic drawing of the arrangement of the metaobjective. It comprises two polymer metalenses spaced with an electrolyte. Both are electrically switchable separately via an applied voltage. The metaobjective is illuminated with an IR laser beam ( $\lambda = 2.65 \mu\text{m}$ ) and the focused intensity is imaged along the optical axis. (b) The metaobjective from metallic polymer allows for four different states. Non-volatile operation is used to set the refractive power of the individual metalenses either ON or OFF with an applied voltage of +1 V or -1 V, respectively. State 1 (metalens 1: ON, metalens 2: OFF): single focus at focal plane  $F_1$  of metalens 1. State 2 (metalens 1: OFF, metalens 2: ON): single focus at focal plane  $F_2$  of metalens 2. State 3 (metalens 1: ON, metalens 2: ON): two foci at focal planes  $F_1$  and  $F_2$ . State 4 (metalens 1: OFF, metalens 2: OFF): no refractive power of metaobjective. The entire metaobjective is thus switched OFF.

## 2.7 CONCLUSIONS & OUTLOOK

Our electrically switchable plasmonic nanoantennas and metasurfaces enabled by metallic polymers expand the functionality and performance of plasmonic-based electro-optical active devices and on-chip optical components. The fabrication from PEDOT:PSS is low cost and scalable due to the commercial availability. We envision that our concept will be of importance in several distinct fields: Subwavelength-sized polymer nanoantennas will make a sizable impact in the development of displays and active optical components. One can address individual subwavelength pixels to push the pixel densities of emerging optical technologies to entirely new dimensions. Furthermore, in comparison to state-of-the-art metallic and dielectric nanoantennas, the polymer nanoantennas allow a new level of flexibility for the fabrication on flexible substrates for curved optical devices. This is necessary to realize AR and VR technologies that work in transmission, e.g., on contact lenses or glasses. Ultimately, this could even enable pixel densities of over 2000 lines/mm, which would support full-color holographic movies at very large field of view. All this is aided by the operation at only  $\pm 1$  V, which is very favorable for low-voltage CMOS compatibility (0 to 3.3 V) at moderate local electric fields. From a more fundamental standpoint, current efforts in quantum technology and methodology require intricate coupling and control schemes, which can, for example, be realized by sophisticated switchable and reconfigurable metasurfaces, currently out of reach with state-of-the-art techniques [70]. Such structures would allow for an entirely new level of integration and miniaturization. From a basic research point of view, further studies into the working principle of the plethora of metallic/conductive polymers will allow for a fine tuning and manipulation of their properties. This includes shifting the plasma frequency and thus the operation point into the visible wavelength region, increase the switching speed for cycling beyond current video-rate, as well as the reduction of degradation. Further detailed investigations on the influence of, e.g., oxygen and humidity during electrochemical switching, adjustments to the fabrication process and electrochemical cell sealing in inert gas environments or using solid electrolytes should benefit the overall switching performance. Additionally, conductive polymers have recently proven to be extremely long-term stable with little to no degradation over  $> 10^7$  cycles at video rate switching frequencies [71]. Metallic polymers also offer the opportunity to gradually change the carrier density and hence the plasma frequency, which allows for grey scale operation and thus opens another window of opportunity. In combination with the hysteresis behavior that enables non-volatile operation, extremely energy efficient display devices could be realized in the future.



This chapter is based on the following published work:

- **J. Karst**, F. Sterl, H. Linnenbank, T. Weiss, M. Hentschel, and H. Giessen  
*Watching In-Situ the Hydrogen Diffusion Dynamics in Magnesium on the Nanoscale*  
*Science Advances* **6**, eaaz0566 (2020).
- **J. Karst**, M. Hentschel, F. Sterl, and H. Giessen  
*Liquid Hydrogenation of Plasmonic Nanoantennas via Alcohol Deprotonation*  
*ACS Photonics* **8**, 1810 (2021).

### 3.1 INTRODUCTION

Switchable optical and nanophotonic systems are of ever-increasing interest, not only from a fundamental [72–76], but in particular from an applied standpoint [17, 48, 77–82]. Plasmonic nanophotonic systems fabricated from materials whose optical properties and material states are tunable upon external stimuli are becoming more important in several different fields of optical applications [40]. They allow the realization of plasmonic optical gas sensors [77, 78, 83], plasmonic molecule detectors [84–89], plasmonic displays [5, 25, 42, 53, 90, 91], tunable plasmonic metasurfaces [4, 12, 17, 24, 38, 92, 93], and many more reversible and non-reversible applications. Especially plasmonic optical sensing platforms are an emerging field of interest as they allow, for example, to detect hydrogen via an optical readout without further need of electronics in highly explosive environments [94–96]. Such sensors rely on the used plasmonic materials to be highly sensitive to a hydrogen exposure. Frequently used materials to show such characteristic properties are, e.g., magnesium (Mg) [45–47, 97–100], niobium (Nb) [80, 101], yttrium (Y) [48, 102], or palladium (Pd) [73–76]. The latter is typically used as a catalyst to split hydrogen molecules at the Pd surface and to allow further diffusion of hydrogen atoms into the attached hydrogen-sensitive layers.

Consequently, active plasmonic and nanophotonic systems require switchable materials with extreme material contrast, short switching times, and negligible degrada-

tion. On the quest for these supreme properties, an in-depth understanding of the nanoscopic processes is essential. In the first part of the following chapter, using a novel scheme, we unravel the nanoscopic details of the phase transition dynamics of metallic Mg to dielectric magnesium hydride ( $\text{MgH}_2$ ) using free-standing films on gold grids for in-situ nanoimaging with near-field microscopy. A characteristic  $\text{MgH}_2$  phonon resonance is utilized to achieve unprecedented chemical specificity between the material states. Our results reveal that the hydride phase nucleates at grain boundaries, from where the hydrogenation progresses into the adjoining nanocrystallites. We measure a much faster nanoscopic hydride phase propagation in comparison to the macroscopic propagation dynamics. Our novel method offers an engineering strategy to overcome the hitherto limited diffusion coefficients and has significant impact on the further design, development, and analysis of switchable phase transition as well as hydrogen storage and generation materials.

In the second part, we will investigate yttrium - another metal whose optical properties are tunable by hydrogen incorporation. Commonly, this happens via exposure to hydrogen gas. Here, we demonstrate that the hydrogenation of yttrium is also possible via the deprotonation of alcoholic liquids. Palladium-covered yttrium is placed in an ethanol bath which causes the deprotonation of ethanol and the hydrogenation of yttrium to yttrium dihydride. Proof of concept is presented with a study on thin films, which is followed by tuning the optical properties of plasmonic nanoantennas. The liquid hydrogenation causes the plasmonic resonance to shift by more than 300 nm in the near-infrared spectral range. Consequently, we show that our plasmonic nanoantennas serve as a local nanooptical indicator for the deprotonation process. Our findings pave the way towards a (nano-)optical investigation and detection of catalytic processes in liquids without the need of electrical, chemical, or electrochemical read-out.

## 3.2 THEORETICAL BACKGROUND

The measurements in the first half of this chapter deal with a high-resolution microscopy method where the optical and topographical properties of metals and dielectrics are measured and analyzed at the nanoscale. With this scattering-type scanning nearfield optical microscopy (sSNOM), one reaches resolutions below the ABBE diffraction limit ( $\lambda/2$ ) of standard optical microscopes but also below the resolution of an aperture-based scanning nearfield optical microscopy (SNOM) ( $\approx \lambda/10$ ), which was firstly realized by Lewis *et al.* [103] and Pohl *et al.* [104] in 1984. The sSNOM technique replaces the small aperture with a small scatterer [105–107] which is illuminated, e.g., by a laser. Due to its small size and its short distance to the sample surface, it can exhibit enhanced optical fields (near-fields<sup>1</sup>) which are modified by the sample underneath. As a result, the scattered light measured in the far-field<sup>2</sup> contains information about the sample’s local properties. In experiment such a small scatterer is realized with an elongated tip of an atomic force microscopy (AFM). The mechanical and optical resolution of the sSNOM is then given by the radius  $a$  of the tip apex. In the following<sup>3</sup> we will shortly explain the principle of sSNOM followed by its theory and will explain the pseudoheterodyne detection for background-free measurements. We will close with a discussion on hydrogen in metals.

### 3.2.1 sSNOM Working Principle

The principle of the sSNOM is shown in Figure 3.1a. It uses a standard AFM to scan over the surface of a sample (tapping mode). The cantilever oscillation frequency, which changes due to tip-sample interaction (e.g. VAN DER WAALS forces), is read out with a laser resulting in an image of the sample topography. In addition, the region around the tip is illuminated with another focused laser beam. This results in an optical image of the sample’s NF optical properties. The spatial resolution is limited by the tip radius of curvature which is on the order of  $a \approx 20 - 25$  nm. The probing region is defined as the gap between the tip apex and the sample. The tip is oscillating at its resonance frequency  $\Omega$  with the consequence that the NF optical signal is modulated at harmonics  $n\Omega$ . Advantageously, the background scattering signal, resulting from scattering at the tip shaft and from the sample outside the probing area, is barely

---

1 In general, the near-field (NF) can be measured for distances  $D$  shorter than the wavelength of the radiated electro-magnetic field ( $D \leq \lambda$ ) and decays exponentially with  $D$ .

2 For longer distances  $D \gg \lambda$ , a propagating electromagnetic field of, e.g., a radiative antenna is defined as far-field (FF).

3 This section is based on [108, 109].

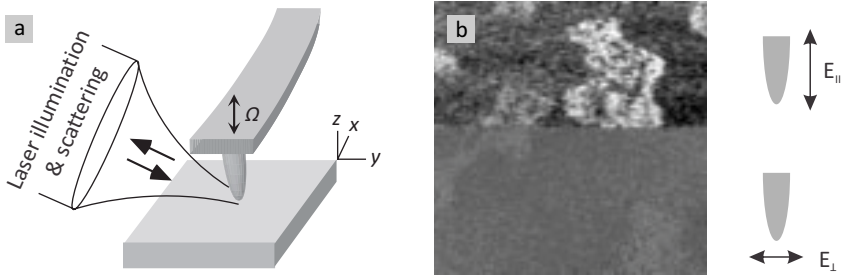


FIGURE 3.1. **Principle of sSNOM.** (a) The tip of an AFM is illuminated by a focused laser. The tip is oscillating at its resonance frequency  $\Omega$ . The backscattered light from tip, sample and shaft is collected in the FF. Sketch is taken from [110]. (b) Infrared NF image of a silicon substrate with 20 nm high gold islands on top. Halfway through, the polarization of the incident light was flipped from parallel (upper part) to perpendicular to the tip (lower part). Image was taken from [111].

modulated and can be **electronically** eliminated.

The tips themselves can either be dielectric or metallic. Early sSNOM experiments used dielectric tips [112], which are limited with respect to the local field enhancement and therefore the coupling of the optical fields in the probing gap. However, metallic shafts / tips can be excited much stronger with an incident light polarized parallel to the shaft / tip axis. As a consequence, the probing NF should be fully z-polarized and the tip will act as an antenna which enhances the probing NF strongly. This is shown in Figure 3.1b for the measurement of the IR NF image of a silicon substrate with 20 nm high gold islands. Halfway through the measurement, the polarization of the incident laser was rotated from parallel (upper part) to perpendicular (lower part) with respect to the metal-coated sSNOM tip. We see that the contrast in the image drops significantly when the polarization is flipped perpendicular to the tip. For applications in the visible (VIS) and IR, researches found platinum (Pt) coated tips to be very suitable [113, 114]. Finally, an interferometric detection allows the simultaneous measurement of the optical NF amplitude *and* phase, especially enabling high phase contrast imaging [113, 115, 116].

### 3.2.2 Finite Dipole Model

The typical configuration in the probing region of a sSNOM setup is shown in Figure 3.2a. An incident electric field  $E_{inc}$  interacts with the tip and the surrounding and



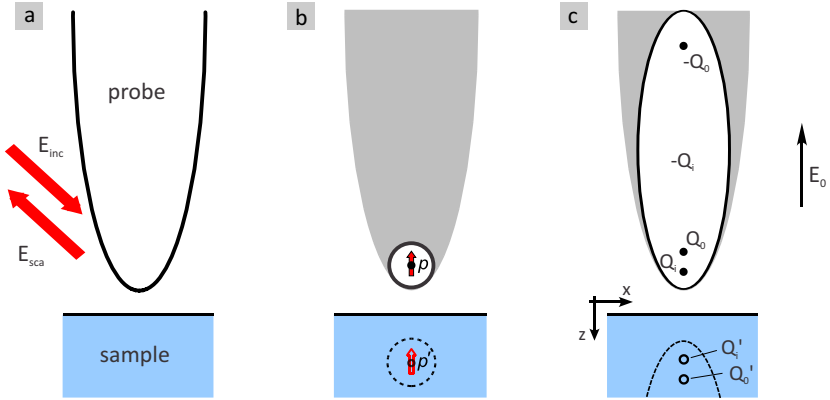


FIGURE 3.2. Sketches of the sSNOM configuration for different theoretical models. (a) shows the sketch of the real configuration in an experiment. (b) The point dipole model approximates the tip firstly as a small sphere, which is then further reduced to a point dipole in its center. (c) In the finite dipole model we approximate the tip by a spheroid in a uniform electric field  $E_0$ . The sketches are taken from [117].

the scattered electric field  $E_{sca}$  is collected in the FF. First attempts to model the results from sSNOM experiments used a point-dipole model [111, 112, 118–123]. A sketch of this model is shown in Figure 3.2b. However, it was found that it is insufficient and many experimental observations could not be explained with the point-dipole model. Furthermore, it is not possible to describe the measured NF contrasts or the spectral position, width, and magnitude of polariton-resonant probe-sample NF interactions quantitatively.

Hence, Cvitkovic *et al.* [117] came up with an analytical finite-dipole model, where an isolated spheroid approximately represents the sSNOM tip [119, 124–128]. The spheroid is assumed to be much smaller than the wavelength  $\lambda$  and it is illuminated by an external uniform electric field  $E_0$ , which is perpendicular to the sample surface. The respective sketch is shown in Figure 3.2c.

The complex model is used to calculate an expression for the NF interaction strength and the amplitude of the scattered field. In order to derive a final expression we have to, at first, neglect the sample and determine the behavior of a perfectly conducting

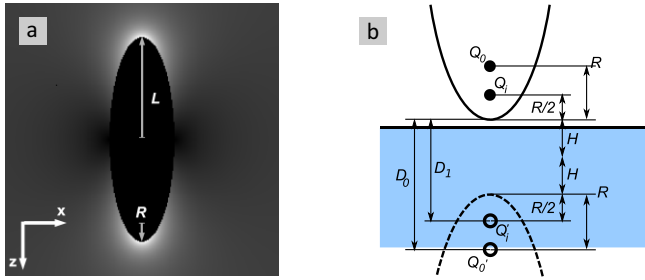


FIGURE 3.3. **Sketches for perfectly conducting spheroid.** (a) Electric field outside of a perfectly conducting spheroid ( $\epsilon \rightarrow \infty$ ). Marked are the long semi-axis  $L$  and the radius of curvature of the spheroid in its apex. (b) Sketch of all charges and distances necessary for calculating the NF interaction between the probe / tip and the sample. The pictures are taken from [117].

spheroid (PCS) in the electric field  $E_0$ . The electric field outside the PCS and along its major axis is

$$E(D) = E_s(D) + E_0, \quad (3.39)$$

with  $E_s$  being the electric field generated by the spheroid and  $D$  being the distance from the spheroid apex. We find from electrostatic calculations

$$E_s(D) = \frac{2D(L+D)}{D^2+L(2D+R)} + \ln \frac{L-F+D}{L+F+D} E_0. \quad (3.40)$$

$$2 \frac{F(L-\epsilon_t R)}{LR(\epsilon_t-1)} - \ln \frac{L-F}{L+F}$$

Here,  $F$  denotes half the distance between the spheroid foci,  $L$  the long semi-axis of the spheroid,  $R$  the radius of curvature of the spheroid in its apex, and  $\epsilon_t$  the dielectric function of the tip material.

The electric field outside of a PCS is shown in Figure 3.3. As we know, for example, from plasmonics, the spheroid electric field  $E_s$  increases for a larger aspect ratio, here given by  $L/R$ . As soon as the spheroid is placed above a surface, it is additionally illuminated by its own reflected NF radiation. This results in very complicated calculations where no closed-form solution of this problem is known. However, it is necessary to calculate the NF interaction. Therefore, we approximate the NF at the spheroid apex by a monopole with charge  $Q_0$ . The electric field is then given by the simple term  $E_{s,m} = A/(R+D)^2$ , where  $A$  is constant.

As we want to calculate the NF interaction of the probe and the surface, we use a mirror charge  $Q'_0 = -\beta Q_0$  to describe the response of the sample to the spheroids NFs. The surface response function

$$\beta = \frac{\varepsilon_s - 1}{\varepsilon_s + 1} \quad (3.41)$$

is very important for further calculations as it includes the dielectric function  $\varepsilon_s$  of the sample [129]. Also the mirror charge  $Q'_0$  radiates an electric field, which acts back on and polarizes the probe (tip), meaning the mirror charge induces in turn charges into the probe. The amount and the distribution of these induced charges needs to be known. In order to calculate these, we place an effective induced point charge  $Q_i$  in the focus of the spheroid at  $z = F$  (see Figure 3.2c for exact position). It is important to note that the charges in the spheroid apex contribute most to the NF interaction when the spheroid is in contact with the sample surface. As soon as the distance  $D$  between apex and sample increases, the relative contribution of the charges further away from the apex increases.

To fully describe the interaction we have to take a further induced charge into account. The induced charge  $Q_i$  in the tip induces a further mirror charge  $Q'_i$  in the sample, which is again acting back on the tip / probe. In total, we find for the illuminated spheroid above a sample an induced charge  $Q_i$  consisting of two parts

$$Q_i = Q_{i,0} + Q_{i,1}. \quad (3.42)$$

To clarify,  $Q'_0$  is the mirror image for  $Q_{i,0}$  and  $Q'_i$  is the mirror image for  $Q_{i,1}$ . They can be calculated as

$$Q_{i,0} = f_0 Q'_0 = - \left( g - \frac{R+H}{L} \right) \frac{\ln \frac{4L}{4H+3R}}{\ln \frac{4L}{R}} Q'_0 \quad (3.43a)$$

$$Q_{i,1} = f_1 Q'_i = - \left( g - \frac{3R+4H}{4L} \right) \frac{\ln \frac{2L}{2H+R}}{\ln \frac{4L}{R}} Q'_i \quad (3.43b)$$

with  $g$  being the fraction of total induced charges to the ones actually contributing to NF interactions (discussion later). Accordingly, we can write for the mirror charges

$$Q'_0 = -\beta Q_0 \quad (3.44a)$$

$$Q'_i = -\beta Q_i. \quad (3.44b)$$

By inserting (eqs. 3.44a and 3.44b) in (eqs. 3.43a and 3.43b), we finally find for the induced charge  $Q_i$ :

$$Q_i = \frac{-\beta f_0}{1 + \beta f_1} Q_0. \quad (3.45)$$

The dimensionless *NF contrast factor*  $\eta$  is then defined as an illumination-independent measure of the sSNOM signal. It is comparable between different samples and different measurements:

$$\eta = \frac{Q_i}{Q_0} = \frac{\beta(g - \frac{R+H}{L}) \ln \frac{4L}{4H+3R}}{\ln \frac{4L}{R} - \beta(g - \frac{3R+4H}{4L}) \ln \frac{2L}{2H+R}}. \quad (3.46)$$

The electric neutrality of the “isolated” spheroid requires an equilibrium of charges, meaning that somewhere on the spheroid a charge  $-Q_i$  exists. This results in a dipole moment  $p_i$  oscillating with the driving field frequency. The light radiated by  $p_i$  is then given as

$$E_{\text{sca}} \sim p = \hat{\alpha} E_0 \quad (3.47)$$

with the dipole polarizability  $\hat{\alpha}$ . In conclusion, the effective dipole moment of the PCS is given as  $p_{\text{eff}} = p_0 + p_i$  with  $p_0 = 2Q_0L$  (dipole moment from external field  $E_0$ ) and  $p_i = \eta Q_0L$  (dipole moment from NF interaction). We find from (eq. 3.40)  $Q_0 = R^2 E_s(0)$  and for the **effective probe polarizability** ( $R \ll L$ )

$$\hat{\alpha}_{\text{eff}} = \frac{p_{\text{eff}}}{E_0} \quad (3.48a)$$

$$= R^2 L \frac{\frac{2L}{R} + \ln \frac{R}{4\epsilon L}}{\ln \frac{4L}{\epsilon^2}} \left( 2 + \frac{\beta(g - \frac{R+H}{L}) \ln \frac{4L}{4H+3R}}{\ln \frac{4L}{R} - \beta(g - \frac{3R+4H}{4L}) \ln \frac{2L}{2H+R}} \right). \quad (3.48b)$$

In contrast, the simplified point dipole model (Figure 3.2b) results in

$$\hat{\alpha}_{\text{eff,PD}} = \frac{\hat{\alpha}}{1 - \frac{\hat{\alpha}\beta}{16\pi(R+H)^3}} \quad (3.49)$$

with the polarizability  $\hat{\alpha} = 4\pi R^3$  of a perfectly conducting sphere.

The scattered NF from the tip-sample-interaction, which is measured in the end in the FF is given by

$$E_{\text{sca}} \propto (1 + r_p)^2 \hat{\alpha}_{\text{eff}} E_{\text{inc}}, \quad (3.50)$$

with the FRESNEL reflection coefficient for  $p$ -polarized light  $r_p$ . This model has only two variable parameters, which are not directly measurable. Firstly, the effective spheroid length (long semi-axis)  $L$ , with the restriction that the probe length  $2L$  is much smaller than the wavelength  $\lambda$ . Secondly, the parameter  $g$ , the fraction of the total induced charge. It is highly relevant for the NF interaction. In the model, we used a perfectly conducting sphere, which is obviously not the case in an experiment.  $g$  takes this into account. In experiments, best values to match the theoretical model to measured data

were found as  $L = 300nm$  and  $g = 0.7e^{0.06i}$ .

Finally, in order to compare the results calculated with this model quantitatively to measured sSNOM data one derives amplitude and phase contrasts

$$\frac{s_{n,A}}{s_{n,B}} = \left| \frac{(1+r_A)^2 \hat{\alpha}_{\text{eff},n,A}}{(1+r_A)^2 \hat{\alpha}_{\text{eff},n,B}} \right| = \left| \frac{\hat{\alpha}_{\text{eff},n,A}}{\hat{\alpha}_{\text{eff},n,B}} \right|, \quad (3.51a)$$

$$\varphi_{n,A} - \varphi_{n,B} = \arg \left( \frac{(1+r_A)^2 \hat{\alpha}_{\text{eff},n,A}}{(1+r_A)^2 \hat{\alpha}_{\text{eff},n,B}} \right) = \arg \left( \frac{\hat{\alpha}_{\text{eff},n,A}}{\hat{\alpha}_{\text{eff},n,B}} \right). \quad (3.51b)$$

Here,  $s_{n,A}$  and  $s_{n,B}$  denote the scattering amplitude of material surface A and B, respectively, with demodulation order  $n$ . Equivalently,  $\varphi_{n,A}$  and  $\varphi_{n,B}$  represent the corresponding scattering phase. As we typically measure the materials A and B close to their material boundaries, we can assume a homogeneous large-area illumination for the reflection coefficient  $r_p$ . This results in  $r_A = r_B$ . Note that the paper by *Cvitkovic et al.* contains a mistake in formula (19), where the left side should read  $\varphi_{n,A} - \varphi_{n,B}$  and not  $\varphi_{n,A}/\varphi_{n,B}$  [117].

### 3.2.3 Pseudoheterodyne Detection

As already explained, sSNOM measurements use an interferometric detection to obtain both amplitude and phase of the scattered electric field  $E_{\text{sca}}$ . However, a simple measurement with lock-in amplification and demodulation at the tip oscillation frequency  $\Omega$  would contain significant background signal, originating from the scattering of the tip shaft as well as from scattering of the sample area around the actually probed area. To remove this background, one can use several methods, however, the most promising one is the pseudoheterodyne detection [130].

In general, most methods use a background (BG) suppression by a demodulation at higher harmonics. To explain this we refer to the effective polarizability  $\hat{\alpha}_{\text{eff}}$ , derived in (eqs. 3.48b and 3.49), which has a non-linear dependence on the tip-sample distance  $H$ . When the tip (time-dependent position  $z(t)$ ) is oscillating with  $z(t) = \Delta z \sin \Omega t$  at the frequency  $\Omega$  with an amplitude

$$\Delta z = \Delta H \ll \lambda, \quad (3.52)$$

this nonlinearity allows a Fourier decomposition of the time-dependent effective polarizability. It is given as

$$\hat{\alpha}_{\text{eff}} = \sum_n \hat{\alpha}_{\text{eff},n} \cos(n\Omega t). \quad (3.53)$$

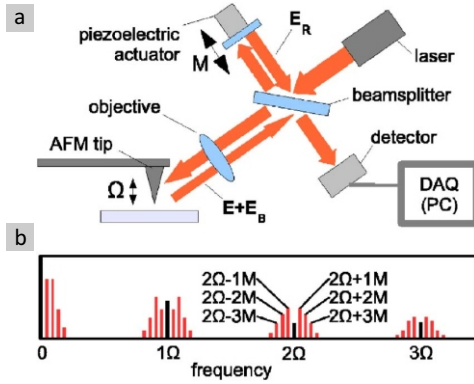


FIGURE 3.4. **Pseudoheterodyne detection** for an sSNOM experiment to eliminate the background scattering  $E_b$ . It is done by a sinusoidal phase modulation of the reference beam  $E_R$ . (a) shows the experimental setup. (b) shows the detected signal spectrum. The figure is taken from [130].

with the scattered electric field components

$$E_{sca,n} = \sigma_n E_{inc} = s_n e^{i\varphi_n} E_{inc} \sim (1 + r_p)^2 \hat{\alpha}_{eff,n} E_{inc}, \quad (3.54)$$

where  $\sigma_n = s_n e^{i\varphi_n}$  is the scattering coefficient and  $s_n$  and  $\varphi_n$  are interferometrically measured with an sSNOM setup. Conclusively, the fast changing NF interaction generates light scattering at higher harmonics  $n\Omega$ . However, the BG changes only slowly and is therefore modulated at DC or at lower harmonics compared the NF signal. Hence, signal demodulation at high-enough harmonics  $n\Omega$  would seem sufficient in order to remove the BG. However, as detectors always measure light *intensity*, we can show that the BG  $E_b$ , present in the scattered electric field  $E_{sca} = E_{NF} + E_b$ , still affects the detector output. The intensity at the detector is given as

$$I \propto E_{tot} E_{tot}^* = (E_{NF} + E_b + E_{ref}) \cdot (c.c.) \quad (3.55a)$$

$$= E_{NF}^2 + E_{NF} E_b^* + E_{NF}^* E_b + E_{NF} E_{ref}^* + E_{NF}^* E_{ref}, \quad (3.55b)$$

where  $E_{ref}$  denotes the electric field of the reference beam in the interferometric detection (here: MICHELSON-interferometer). One possibility to get rid of  $E_b$ -contributions is by using a pseudoheterodyne detection, where the reference beam is additionally modulated at a frequency  $M$  causing frequency side-bands where no BG is present anymore.

To show this, we write out the scattered electric field  $E_{\text{sca}}$  as a Fourier series  $E_{\text{sca}} = \sum_n \tau_n e^{in\Omega t}$ . Please note again that the scattered field  $E_{\text{sca}} = E_{\text{NF}} + E_b$  is a sum of NF  $E_{\text{NF}}$  and BG contributions  $E_b$ , similar as its expansion coefficients. They are given as  $\tau_n = \sigma_n + \sigma_{b,n}$ , where  $\sigma_n$  and  $\sigma_{b,n}$  are the Fourier coefficients of  $E_{\text{NF}}$  and  $E_b$ . The detector output voltage is then given as

$$u_n \approx \kappa(\sigma_{b,0}\sigma_n^* + \sigma_{b,0}^*\sigma_n) = 2\kappa s_{b,0}s_n \cos(\varphi_{b,0} - \varphi_n), \quad (3.56)$$

where  $\kappa$  is a proportionality constant for the detector sensitivity. The goal of the detection mechanism is to extract the pure NF contribution  $\sigma_n = s_n e^{i\varphi_n}$  by avoiding its interference with the background  $\sigma_{b,0} = s_{b,0} e^{i\varphi_{b,0}}$  ( $s$  and  $\varphi$  are the scattering amplitude and phase, respectively). For this, the pseudoheterodyne detection uses a sinusoidal phase modulation of the reference wave  $E_R$ . A sketch of a typical setup is shown in Figure 3.4a. The phase modulation is given by

$$E_R = \rho e^{i\gamma \sin(Mt) + i\Psi_R}, \quad (3.57)$$

where  $M$  is the phase modulation frequency and  $\gamma$  its modulation depth.  $\Psi_R$  denotes the phase offset resulting from the average optical path difference between signal and reference beam. When we choose the reference modulation frequency  $M$  to be lower than the tip vibration frequency  $\Omega$ , meaning  $M < \Omega$ , each scattered high-harmonic signal  $n\Omega$  ( $n > 0$ ) is split into side-bands. The frequencies are given by

$$f_{n,m} = n\Omega + mM \quad (3.58)$$

as illustrated in the signal spectrum Figure 3.4b. Finally, the *multiplicative* BG is still present at the frequencies  $f_{n,0} = n\Omega$ , but not at the side-band frequencies  $f_{n,m \neq 0}$ . By demodulating the scattered signal  $E_{\text{sca}}$  at these side-bands  $f_{n \neq 0, m \neq 0}$ , we avoid multiplicative BG interference.

With this pseudoheterodyne detection (eq. 3.55b) is simplified to

$$I \propto E_{\text{tot}} E_{\text{tot}}^* = E_{\text{NF}} E_{\text{ref}}^* + E_{\text{NF}}^* E_{\text{ref}}, \quad (3.59)$$

where no BG contribution is present anymore.

### 3.2.4 Magnesium and Hydrogen

As we will analyze the phase transition from metallic Mg to dielectric MgH<sub>2</sub> in section 3.3, we will elaborate on this metal-hydrogen system in following in more detail. Hereby, the most important aspects include the general optical properties in the VIS and infrared (IR) spectral range including phonon resonances.

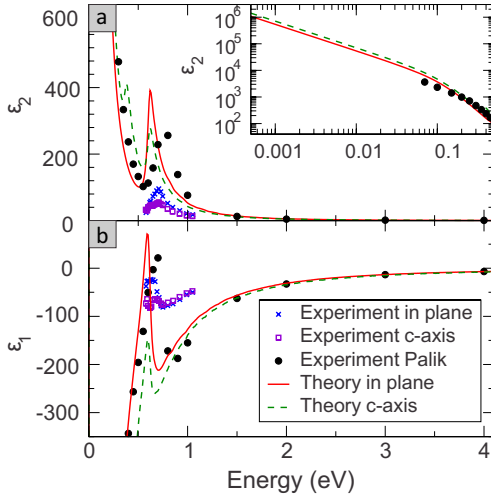


FIGURE 3.5. **Dielectric function of Mg.** (a) Imaginary part  $\epsilon_2$  and (b) the real part  $\epsilon_1$ . Plots are taken from [132].

### Hydrogen

Before having a closer look onto Mg and  $\text{MgH}_2$ , we want to briefly discuss hydrogen itself. The hydrogen atom is the smallest atomic unit and consists of one proton and one electron (1s orbital). In nature, hydrogen is found as a molecule hydrogen ( $\text{H}_2$ ), consisting of two single hydrogen atoms. In air, it is ignitable at concentrations between 4 % and 74 % [131]. For safety reasons, our chosen concentrations of  $\text{H}_2$  in nitrogen ( $\text{N}_2$ ) in this work do not exceed  $c_{\text{H}_2} = 4$  %. The reason is that the reaction of  $\text{H}_2$  in combination with oxygen ( $\text{O}_2$ ) is exothermic. A useful application of this reaction are, e.g., fuel cells which can be used as energy sources for transportation industry. For this purpose, hydrogen has to be stored and released in a hydrogen storage system.

### Magnesium and Hydrogen

Mg is a promising hydrogen-storage-material, as it can incorporate up to 7.6 mass% of hydrogen. The crystal structure of Mg is a hexagonally closed package (hcp). When it is switched to  $\text{MgH}_2$ , the hydrogen atoms bind to the Mg atoms changing its crystal structure to tetrahedral. In addition, Mg holds great promise for active and switchable optical systems. However, the hydrogenation of Mg to  $\text{MgH}_2$ , so far, comes with very



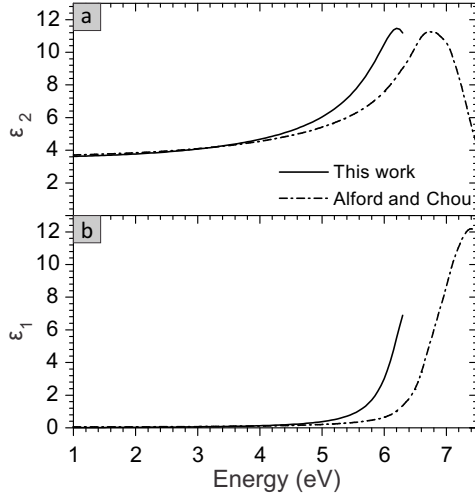


FIGURE 3.6. Dielectric function of MgH<sub>2</sub>. (a) Imaginary part  $\epsilon_2$  and (b) the real part  $\epsilon_1$ . Plots are taken from [133].

long switching times.

To overcome this drawback, several strategies can be envisioned. On the one hand, it is possible to alloy Mg with other metals such as, e.g., nickel. This increases the hydrogen diffusion speed, however simultaneously reduces the hydrogen storage capacity. On the other hand, a multilayer system of Mg with a titanium (Ti) buffer layer topped with a Pd layer can be used to enhance the kinetics of hydrogen absorption and desorption. The key component here is Pd, which acts as a catalyst. At its surface, the hydrogen molecules are split up into atoms and can thus diffuse into the volume / layers. This greatly increases the diffusion speed into Mg. In this multilayer system, Ti is used as a buffer layer to prevent alloying between Mg and Pd. Interestingly, this alloy would act as a diffusion barrier for hydrogen.

Very important for this chapter and for all optical applications are the actual optical properties of Mg and MgH<sub>2</sub>. They are mostly given by the complex dielectric function  $\epsilon = \epsilon_1 + i\epsilon_2$ . Figure 3.5a and b show the imaginary ( $\epsilon_2$ ) and the real part ( $\epsilon_1$ ) of the dielectric function for Mg, respectively [132]. For small energies  $E < 1.5$  eV, we see a typical metal-like DRUDE behavior for  $\epsilon_1$  and  $\epsilon_2$  as explained in section 2.2.2 with (eq. 2.13a). It is overlaid with a sharp peak at  $E = 0.7$  eV corresponding to interband

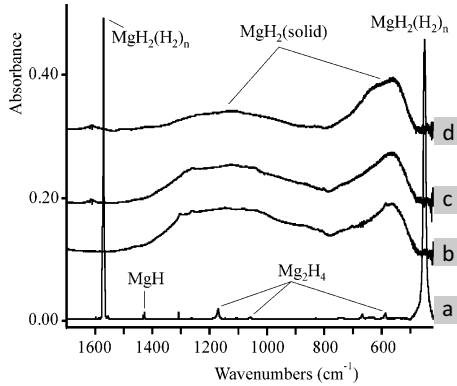


FIGURE 3.7. IR spectrum of laser-ablated  $\text{MgH}_2$ . Deposited on cryogenic windows. FTIR spectrum (a) after deposition, (b) after warming to 10 K, (c) after warming to 200 K and (d) at room temperature. Plots are taken from [134].

transitions, similar to the data shown in Figure 2.2 for gold.

Figure 3.6a and b depict the imaginary and real part of  $\epsilon$  for  $\text{MgH}_2$ , respectively. We find the typical behavior for a dielectric in the whole displayed spectral range, meaning the real part  $\epsilon_1$  (Figure 3.6b) is always positive but close to zero and the imaginary part  $\epsilon_2$  (Figure 3.6a) is positive but very small. In the range of  $E = 5 - 7$  eV the data shows a peak in  $\epsilon_2$  as well as an increase in  $\epsilon_1$ . This absorption in a  $\text{MgH}_2$  film is due to its band gap energy at  $E \approx 5.6$  eV [133].

#### Phonon Vibrations of Mg and $\text{MgH}_2$

Apart from resonances due to interband transitions, Mg and also  $\text{MgH}_2$  possess additional resonances. In solids, the lattice vibrations, called phonons, are of prime interest. One has to distinguish between acoustic phonons (coherent displacement in propagation direction) and optical phonons (out of phase movement perpendicular or parallel to the propagation direction). Only optical phonons can be excited directly or indirectly by light. Here we distinguish between *IR-active* (direct) and *RAMAN-active* (indirect) phonons. On the one hand, a phonon is *IR-active* when the lattice vibration results in a change of a permanent dipole moment. This is only possible in crystals with at least a diatomic base (as e.g.  $\text{MgH}_2$ ). The crystal lattice vibrates in the opposite direction after flipping at the center of inversion, which is why *IR-active* phonons possess an odd symmetry and are called “ungerade  $u$ ”. On the other hand, *RAMAN-active* phonons have a changing polarizability. They are present in crystals already for a

one-atomic base (e.g. Mg). The crystal lattice vibrates same after flipping at the center of inversion, which is why RAMAN-*active* phonons possess an even symmetry and are called “gerade  $g$ ” [135].

In this work, we perform sSNOM experiments in the mid-infrared (MIR) to measure the NF optical properties of Mg and MgH<sub>2</sub>. Previous reports have shown that in these measurements one can only excite *IR-active* phonons. However, as Mg possess a one-atomic base it therefore exhibits only RAMAN-*active* phonons. In contrast, we can use specific *IR-active* phonons of MgH<sub>2</sub> to achieve a scattering amplitude and phase contrast enhancement between Mg and MgH<sub>2</sub> in our experiments due to enhanced NFs. A typical measured IR spectrum of MgH<sub>2</sub> for different temperatures is shown in Figure 3.7a-d. Particularly important is the measurement at room temperature (Figure 3.7d) as as all our sSNOM measurements are taken at RT. We see two vibrational modes in the IR spectrum for bulk MgH<sub>2</sub>. The first mode appears at  $\nu \approx 1160 \text{ cm}^{-1}$  ( $\lambda \approx 8.6 \text{ }\mu\text{m}$ ) and the second mode at  $\nu \approx 573 \text{ cm}^{-1}$  ( $\lambda \approx 17.5 \text{ }\mu\text{m}$ ). One major drawback of these phonon modes is that they are very broad at room temperature ( $\Delta\nu \approx 300 - 400 \text{ cm}^{-1}$ ). Therefore, one needs very broadband light sources to be able to detect them.

### 3.3 WATCHING HYDROGEN DIFFUSION IN MAGNESIUM

As mentioned, switchable and active nano-optical systems are of ever-increasing interest. Especially, materials with prominent metal-to-insulator phase transitions are prime candidates for such systems and have thus been investigated in great detail [40, 136]. The extreme change of the optical properties at the transition from the metallic to the dielectric phase renders them highly relevant for switchable optical as well as active plasmonic systems.

One prominent and archetypical material system is Mg which has been widely studied, however, mainly in the context of hydrogen storage [99, 137–143]. In its initial metallic state Mg shows large free electron densities accompanied with comparably small parasitic loss and is consequently an excellent plasmonic material [47, 144]. Exposing Mg to H<sub>2</sub> induces the phase transition from metallic Mg into dielectric MgH<sub>2</sub>, a highly transparent dielectric material. More strikingly, the MgH<sub>2</sub> phase can be reversed into the metallic Mg state, making the phase transition fully cyclical. Conceptually, this allows to controllably and reversibly switch the plasmonic resonances of Mg nanostructures on and off. First studies proved the applicability of the Mg-MgH<sub>2</sub> phase transition for switchable metasurfaces [145], enabling dynamic holography [28], or dynamic plasmonic color displays [42, 90].

Widespread applications are thus far hindered by a number of limiting factors and obstacles such as the volume expansion of the material upon hydrogenation [146], poor cyclability, limited hydrogen diffusion coefficients, and similar. While significant progress has been made in the understanding of nanoscale diffusion [147, 148], a number of application-related obstacles and the strategies to overcome these are related to the following unanswered questions at the boundary between the micro- and nanoscale: Is the comparably slow macroscopic diffusion limited by an intrinsically limited nanoscopic diffusion? What is the influence of the grain boundaries and the nanoscale crystallinity and crystallite formation of the Mg films on the macroscopic diffusion [149]? Why does alloying of Mg with, e.g., nickel (Ni) increase the diffusion coefficient, nanoscopically speaking [150–154]? Answering these questions will lay out new routes to improving the material systems and bringing them closer to the proposed applications.

The aforementioned challenges clearly underline that an in-depth nanoscale investigation of the switching behavior with chemical specificity is highly desired. Here, we present a definite analysis utilizing sSNOM [107, 110–114, 155–157]. We introduce,

on the one hand, a technique that allows for an in-situ imaging of the hydrogenation dynamics of Mg to investigate the influence of nanoscale morphology and crystallinity on the hydride formation process with the high spatial resolution, in this case less than 20 nm. On the other hand, we demonstrate that we can exploit the existence of a strong phonon mode in the dielectric MgH<sub>2</sub> state to achieve unprecedented chemical resolution and specificity between the metallic and dielectric state of our switchable material system. For the first time it becomes possible to spatially visualize in-situ the hydrogenation process with nanometer resolution and image the nanoscopic influence of small grain boundaries in great detail, in contrast to previous studies [148]. We conclude that individual crystallites load hydrogen on significantly shorter timescales than the bulk macroscopic film. Our results suggest that the limited macroscopic hydrogenation speed is related to the prominent crystallite and grain boundary formation in Mg films, highlighting the possibility for significant future improvements.

Additionally, our method is applicable for investigations on several other gas-in-metal systems where the gas causes a sufficient change in the optical properties of the pristine metal. Especially for hydrogen storage, hydrogen generation [158], as well as electrochemical applications, the influence of, e.g., grain boundaries in a huge diversity of material systems is of great interest.

### 3.3.1 *Concept & Measurement Technique*

The main idea of our method is sketched in Figure 3.8a. We use transmission electron microscopy (TEM) gold grids pre-coated with a 2-3 nm Pd thin film (Substratek, Ted Pella, Inc.). Subsequently, we thermally evaporate 10 nm Pd, 5 nm Ti and 50 nm Mg thin films (without breaking the vacuum in between two consecutive evaporation steps). During evaporation, the sample is kept at a constant temperature of  $T = 20^\circ\text{C}$ . Consequently, at the holes of the TEM grid we obtain free-standing thin films. The Pd acts as a catalytic layer, splitting the hydrogen molecules and enabling the diffusion into the Mg film [97, 159]. Ti is used to prevent alloying of Mg and Pd, which would cause the formation of a hydrogen diffusion barrier [160, 161]. Mounting the grids into a home-built gas cell, hydrogen gas can access the free-standing thin films from below while the top Mg surface is accessible for the sSNOM measurements. Scanning the tip of the sSNOM over the exposed Mg surface, we can observe in-situ and investigate the time dynamics of the hydride formation and the diffusion of hydrogen into the film with nanometer resolution. We obtain chemical specificity by utilizing an IR-active phonon resonance of MgH<sub>2</sub>. All measurements are performed at room temperature. Please note that due to oxidization of the surface of Mg, a thin MgO layer is formed.

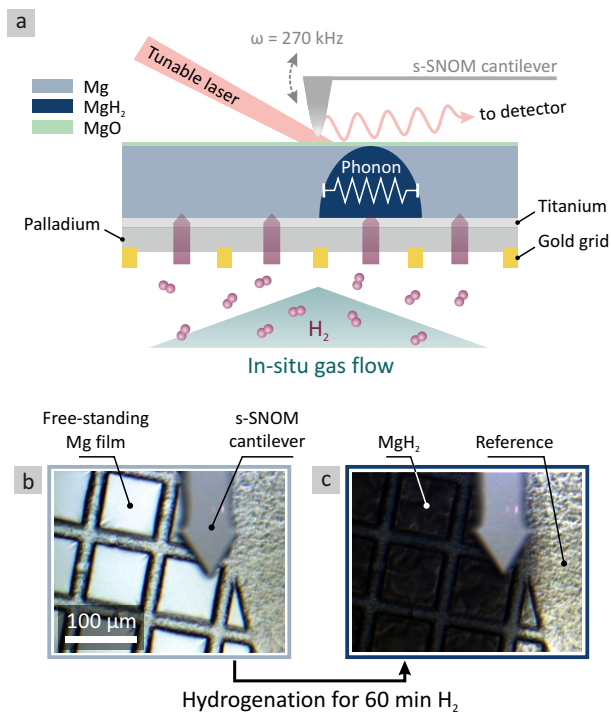


**FIGURE 3.8. In-situ sSNOM principle.** (a) Schematic drawing of the principle for in-situ sSNOM. We use free-standing thin films realized by thermally evaporating 10 nm Pd, 5 nm Ti, and 50 nm Mg on a Pd-Au-membrane. This allows hydrogenation from below. The metalized AFM tip of the sSNOM setup is scanning the top surface to investigate the local optical properties while the Mg thin film is absorbing hydrogen. Additionally, a characteristic IR phonon of MgH<sub>2</sub> enables chemically specific imaging. The Mg layer is in contact with air causing oxidization. However, the very thin magnesium oxide (MgO) layer is transparent for imaging at the frequency of the MgH<sub>2</sub> phonon and is barely influencing our sSNOM measurements. (b,c) Optical images (taken in reflection) showing the sSNOM cantilever and the free-standing Mg film in its pristine state as well as after 60 min hydrogen gas flow (2% at 1 bar), respectively.

However, this oxide layer is barely influencing our sSNOM measurement, as neither Mg, MgO [162] nor any Mg(OH)<sub>x</sub> compounds [163, 164], but only MgH<sub>2</sub> has a characteristic material resonance at our imaging wavelength. Additionally, as MgO and Mg(OH)<sub>x</sub> are dielectric materials we expect them to be mostly transparent at the imaging wavelength in our near-field sSNOM measurements.

In Figure 3.8b and c, optical images (taken in reflection) depict the sSNOM cantilever and the surface of the Mg film in its pristine state as well as after 60 min of hydrogenation. The film is exposed to a H<sub>2</sub> concentration of 2% in N<sub>2</sub> at 1 bar pressure with a flow rate of 0.3 l/min. The highly reflective metallic Mg film switches to dielectric MgH<sub>2</sub>, which appears black. Additionally, we marked the reference position, where we take reference sSNOM measurements to normalize all near-field sSNOM measurements.

For all sSNOM measurements a commercial sSNOM (neaSNOM, neaspec) equipped with a liquid-nitrogen-cooled MCT detector is employed. A platinum-iridium coated AFM tip with a tip radius of 25 nm and a cantilever resonance frequency of approximately 285 kHz (NanoWorld Arrow, NCPt) serves as near-field probe. We are using a pseudo-heterodyne interferometric lock-in detection of the backscattered light from tip and surrounding sample to obtain the optical near-field information [130]. Utilizing the side-bands of the 4<sup>th</sup> harmonic (n=4) of the cantilever oscillation frequency  $\omega_{\text{tip}}$  we obtain the amplitude  $s_4$  and phase  $\varphi_4$  of the scattered electric field. For the tip illumination, a parametric frequency converter system (Alpha-HP, Stuttgart Instruments) and a subsequent difference-frequency generation allows to tune the illumination wavelength in the mid infrared from  $\lambda = 1.4 \mu\text{m}$  to  $\lambda = 20 \mu\text{m}$  [165]. To specifically address individual phonon resonances the output radiation of the aforementioned light source is filtered with a grating monochromator to below  $10 \text{ cm}^{-1}$  full width at half maximum (FWHM).

Our in-situ sSNOM measurements of the hydrogenation of Mg are taken on the free-standing film, where hydrogen can directly access the Pd film via a home-built gas flow-cell from below. The measured area is  $1 \times 1 \mu\text{m}^2$  with a resolution of  $100 \times 100$  pixel. First, we take a sSNOM scan of the pristine Mg film, while flushing the flow-cell with pure N<sub>2</sub>. When the scan is finished, we add 2% of H<sub>2</sub> in N<sub>2</sub> to hydrogenate the sample for a time  $t$ . Subsequently, we turn H<sub>2</sub> off and flush again with pure N<sub>2</sub> to keep the Mg/MgH<sub>2</sub> film in its current state and to prevent the desorption of hydrogen during the sSNOM scan. We take another scan and repeat this procedure until the hydrogenation saturates and no more hydrogen is absorbed.

We take reference measurements to normalize and correct our near-field scattering amplitude and phase data. As marked in Figure 3.8c, the reference measurements are taken on the grid, as here the Mg film is not influenced by the hydrogenation and stays in its pristine state for the whole 60 min of H<sub>2</sub> exposure. We take a reference sSNOM measurement ( $1 \times 1 \mu\text{m}^2$  with a resolution of  $50 \times 50$  pixel) after each hydrogenation time-step  $t$  and correct the near-field scattering amplitude  $s$  and phase  $\varphi$  as follows:

$$s_{i,j,\text{norm}}(t) = \frac{s_{i,j}(t)}{\bar{s}_{\text{ref}}(t)}, \quad (3.60a)$$

$$\varphi_{i,j,\text{norm}}(t) = \varphi_{i,j}(t) - \bar{\varphi}_{\text{ref}}(t), \quad (3.60b)$$

where  $i,j$  denote the pixel coordinate in the respective sSNOM measurement,  $s_{i,j,\text{norm}}(t)$  and  $\varphi_{i,j,\text{norm}}(t)$  the normalized/corrected scattering amplitude and phase value of this pixel, respectively,  $s_{i,j}(t)$  and  $\varphi_{i,j}(t)$  the raw values of the pixel, and  $\bar{s}_{\text{ref}}(t)$  and  $\bar{\varphi}_{\text{ref}}(t)$  are the mean values of the scattering amplitude and phase of the reference measurement, respectively.

### 3.3.2 Near-Field Appearance of Phase Transition

As a first step, we are introducing the main measurement quantities as well as their respective significance in our experimental routine in Figure 3.9. Generally speaking, an sSNOM measurement delivers two main quantities: Topological information as well as information about the local optical properties, i.e., the complex dielectric function of the sample surface [113]. The AFM cantilever is raster scanned over the sample surface and delivers the surface topography. An incident light field is additionally scattered from the oscillating tip and reports information about the local nanoscopic interaction of this light field with the sample surface. As explained in section 3.2, appropriate demodulation and detection techniques allow inferring on the local optical properties with nanoscale resolution.

Typical sSNOM measurements of the same area of a Mg film are depicted in Figure 3.9a-d. For comparison, we plot these measurements for the film in its pristine state (left columns) and after 10 min of hydrogenation (right columns). All measurements of one column are acquired simultaneously in one single sSNOM scan. Panels a and b are depicting the information obtained from the AFM part of the sSNOM, which are the surface topography or height variation of the surface as well as the mechanical cantilever oscillation phase, respectively. As seen, the visibility of the boundaries between individual grains is much higher in the mechanical phase as compared to the topography. Consequently, we utilize the mechanical phase for a grain boundary



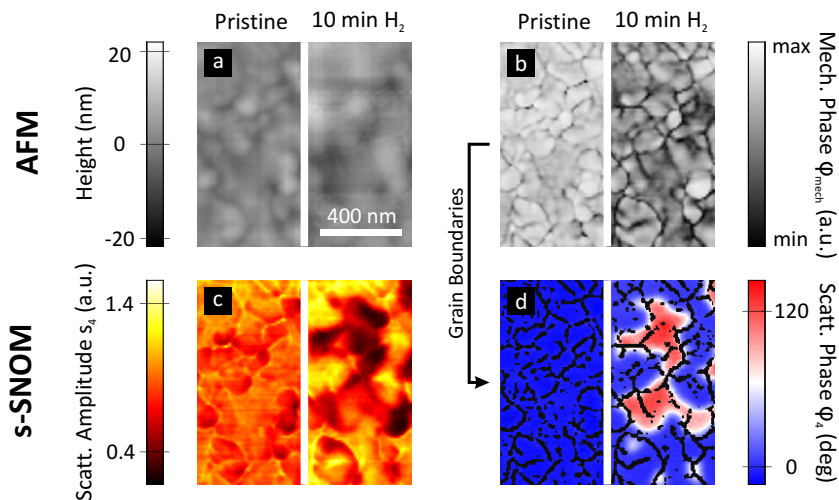


FIGURE 3.9. **Near-field appearance of the Mg-MgH<sub>2</sub> phase transition.** (a-d) sSNOM measurements depicting the same area of a 50 nm Mg film in its pristine state and after 10 min of hydrogenation at room temperature. (a) The topography depicts the expansion of the individual nanocrystallites of the polycrystalline Mg film during hydrogenation. (b) The mechanical phase  $\varphi_{\text{mech}}$  indicates clear grain boundaries between the individual nanocrystallites of the polycrystalline Mg film. By applying an edge detection filter, we extract a mask of these grain boundaries. (c) The scattering amplitude  $s_4$  (4<sup>th</sup> demodulation order) drops when metallic Mg changes to dielectric MgH<sub>2</sub>. However, the scattering amplitude is also highly influenced by the surface roughness as grain boundaries are clearly visible in the 2D scans plotted in (c). This leads to an inaccuracy in the determination where Mg has switched to MgH<sub>2</sub>, as both, a change in the optical properties as well as a change in the surface morphology / roughness, change the scattering amplitude. (d) The scattering phase  $\varphi_4$  displays a very high material contrast between metallic Mg (blue appearance) and dielectric MgH<sub>2</sub> (red appearance). This is achieved by performing sSNOM measurements at a characteristic IR phonon resonance of MgH<sub>2</sub> and allows a chemically specific nanoscale imaging of the hydrogen diffusion without the influence of the surface topography. The 2D images are overlaid with the grain boundary mask from (b).

extraction.

As mentioned, the tip is illuminated with a strong light field in order to probe the local optical properties of the material. Panels c and d of Figure 3.9 are depicting the near-field scattering amplitude and phase, respectively. The tip-illumination frequency is  $\nu = 1280 \text{ cm}^{-1}$  ( $\lambda = 7.6 \text{ }\mu\text{m}$ ). We find that the scattering amplitude is influenced by changes in the local optical properties and by changes of the film topography. Consequently, it is close to impossible to disentangle these two independent processes from the data. In contrast, the scattering phase shown in Figure 3.9d exhibits supreme phase contrast between Mg (blue) and  $\text{MgH}_2$  (red), without any detectable influence of sample topography and morphology. The reason for this remarkable finding, which is at the heart of our technique, lies with a characteristic infrared phonon of  $\text{MgH}_2$  at about  $\nu = 1320 \text{ cm}^{-1}$ . This resonant phenomenon leads to a significantly increased local absorption of the incident radiation, placing our experiments in the strong absorption regime [166]. Strong absorption is known to influence both scattering amplitude and phase [167]. However, we find that in our case the impact on the scattering phase is much larger as compared to the scattering amplitude. Thus, the  $\text{MgH}_2$  phonon causes a distinct signature of the hydrogenated areas compared to the metallic regions in which this phonon is absent.

In order to prove the resonant nature of this enhancement phenomenon, we have studied the scattering phase in dependence of the wavelength of the exciting radiation. The spectral dependence of the near-field scattering phase is plotted in Figure 3.10a for  $\text{MgH}_2$  (red) and Mg (blue). They are measured using the nanoFTIR module of our sSNOM employing homodyne detection [168, 169]. The solid thin lines indicate the average of four positions whereas the standard deviation is plotted in lighter colors in the background. We observe a large standard deviation on  $\text{MgH}_2$  for  $\nu < 1400 \text{ cm}^{-1}$ . The origin lies within the measurement principle to obtain the nano-FTIR scattering phase spectra. It is based on stitching together 17 individual spectra as the laser offers only limited bandwidth at a certain center frequency. Between the measurement of two individual spectra we have to re-position our sample to compensate for sample drift. The inaccuracy in this re-positioning causes an error in the scattering phase spectrum, which seems to be large on the rough  $\text{MgH}_2$  for wavenumbers  $\nu < 1400 \text{ cm}^{-1}$ .

In Figure 3.10a, one can clearly see the signature of an IR phonon resonance around  $\nu = 1320 \text{ cm}^{-1}$ . We ascribe this resonant enhancement to the known phonon mode of  $\text{MgH}_2$  in this spectral region [134]. In stark contrast, the scattering phase of metallic Mg is spectrally flat over the entire spectral range. The corresponding spectra of the scat-

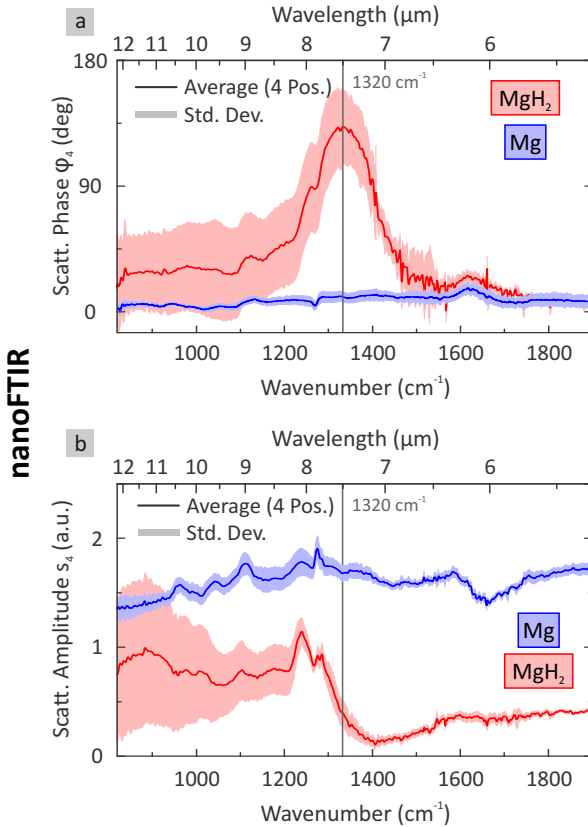


FIGURE 3.10. **Near-field spectral response of Mg and MgH<sub>2</sub>.** nanoFTIR spectra of the near-field scattering (a) phase and (b) amplitude taken on Mg (blue) as well as on MgH<sub>2</sub> (red). The plot shows the average and standard deviation of 4 positions each. The distinct phonon resonance of MgH<sub>2</sub> peaks at  $\nu = 1320 \text{ cm}^{-1}$  and causes a maximum scattering phase difference of  $\Delta\varphi \approx 130^\circ$  between MgH<sub>2</sub> and Mg.

tering amplitude for Mg and MgH<sub>2</sub> can be found in Figure 3.10b. As expected, we find a dispersive line shape in the scattering amplitude spectrum for MgH<sub>2</sub>. Furthermore, we can clearly see that the strong absorption causes, as mentioned above, a much higher contrast between Mg and MgH<sub>2</sub> in the scattering phase than in the amplitude.

This is in good quantitative as well as qualitative agreement with contrast calculations. These results can be found in Figure 3.11. We plot in (a) the scattering amplitude contrast

$$C_s = \frac{s_{4,\text{MgH}_2}}{s_{4,\text{Mg}}} \quad (3.61)$$

and in (b) the scattering phase contrast

$$C_\varphi = \varphi_{4,\text{MgH}_2} - \varphi_{4,\text{Mg}} \quad (3.62)$$

between Mg and MgH<sub>2</sub>. The amplitude and phase spectra are taken from Figure 3.10. Overall, we find a much higher contrast between Mg and MgH<sub>2</sub> in the scattering phase in comparison to the scattering amplitude. Additionally, we use the finite dipole model adapted from *Cvitkovic et al.* to calculate the expected amplitude and phase contrast arising from the MgH<sub>2</sub> phonon around 1320 cm<sup>-1</sup>. It was explained in detail in section 3.2.2. The results are plotted with dashed lines in Figure 3.11. We obtain a very good qualitative agreement with the experimental data. To be able to calculate this material contrast between Mg and MgH<sub>2</sub> in our sSNOM experiments, we require the dielectric function of Mg and MgH<sub>2</sub> in the whole measurement range from  $\nu = 820$  cm<sup>-1</sup> to  $\nu = 1900$  cm<sup>-1</sup>. *Palik* provides  $\epsilon$  for Mg [170], however, no literature data for the dielectric function of MgH<sub>2</sub> is available, especially missing data containing the phonon resonance around  $\nu = 1320$  cm<sup>-1</sup>. Thus, we determine  $\epsilon_{\text{MgH}_2}$  via extrapolation of existing data and modeling of the phononic resonance. First, we extrapolate the  $\epsilon$  data for MgH<sub>2</sub> from *Isidorsson et al.* for the visible and near-infrared spectral range to a constant of  $\epsilon_{\text{MgH}_2}$  for  $\lambda > 1.3$   $\mu\text{m}$  [133]. Second, we add a LORENTZ pole (see section 2.2.3 to the extrapolated dielectric function of MgH<sub>2</sub> to account for the phonon resonance. We adjust only the parameters for the LORENTZ oscillator to match the experimental results best, without varying any other parameters for the finite dipole model.

Furthermore, we make sure the calculated dielectric function results in good qualitative agreement between far-field reflectance measurements and calculations as it is depicted in Figure 3.12. We use experimental FTIR reflectance spectrum of our MgH<sub>2</sub>/TiH<sub>x</sub>/PdH<sub>x</sub> thin films where the phonon resonance is visible (red solid line) and reproduce it with a multi-layer scattering matrix calculation. For these calculations

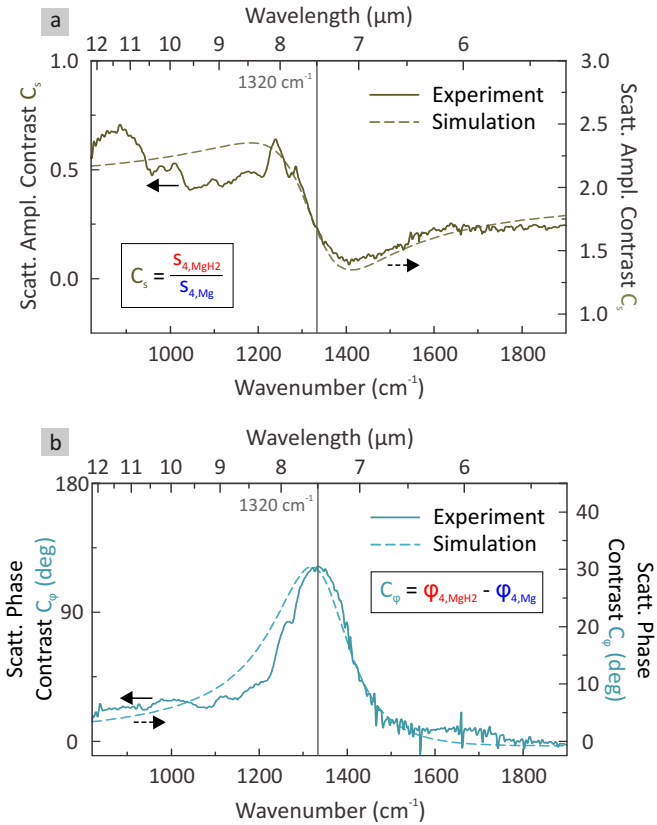


FIGURE 3.11. **Comparison of NF contrast between measurement and calculation.** (a) Measured (solid line, left y-axis) and calculated (dashed line, right y-axis) scattering *amplitude* contrast  $C_s = s_{4,\text{MgH}_2}/s_{4,\text{Mg}}$  between Mg and MgH<sub>2</sub>. (b) Corresponding measured (solid line, left y-axis) and calculated (dashed line, right y-axis) scattering *phase* contrast  $C_\phi = \varphi_{4,\text{MgH}_2} - \varphi_{4,\text{Mg}}$ . The scattering amplitude and phase spectra can be found in Figure 3.10. The calculated spectra are obtained via the finite dipole model explained in section 3.2.2.

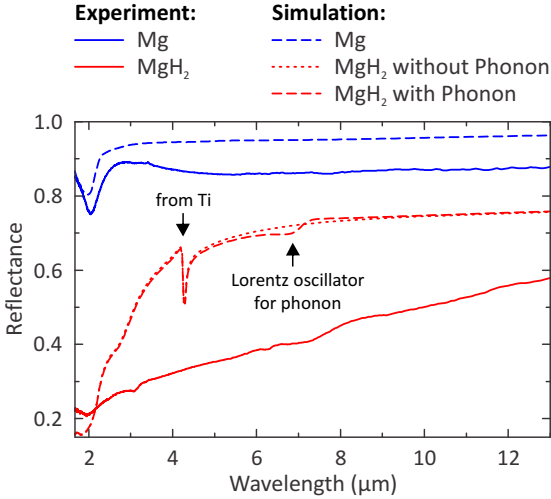


FIGURE 3.12. **Measured and calculated reflectance spectra of Mg and MgH<sub>2</sub> thin films.** The experimental reflectance spectra for Mg and MgH<sub>2</sub> are plotted in solid blue and red lines, respectively. The simulated spectra are plotted with dashed/dotted lines using the same color code. For the simulation of the MgH<sub>2</sub> reflectance spectra we use once dielectric data *without* (red dotted line) and once *with* the phonon (red dashed line), as it was described in the discussion of Figure 3.11.

we use the dielectric function for MgH<sub>2</sub> determined for the calculation in Figure 3.11 *without* the phonon (red dotted line) and *with* the phonon resonance (red dashed line). The arising phonon feature in the calculated reflectance spectrum matches qualitatively well with the experiment. Please note that there is no exact literature data for the dielectric function of PdH<sub>x</sub> and TiH<sub>x</sub> in the spectral range  $\lambda > 2.0 \mu\text{m}$ . Thus, the calculations are always performed with pristine Pd and Ti  $\epsilon$ -data [170]. This is the reason for the overall different line-shape as well as the arising feature around  $4.5 \mu\text{m}$  for the calculated MgH<sub>2</sub> reflectance spectra in comparison to the experiment. For consistency, we depict in Figure 3.12 also the experimental (blue solid line) and calculated (blue dashed line) reflectance spectra of the pristine Mg/Ti/Pd thin films. We obtain a very good quantitative and qualitative agreement.

Overall, this remarkable finding consequently enables chemically specific imaging of the Mg/MgH<sub>2</sub> phase transition and, in combination with the grain boundary mask from the mechanical phase measurement, allows us to precisely track hydride formation.

### 3.3.3 Time-Resolved Hydrogen Diffusion

Following the aforementioned findings, we are investigating the hydrogenation of our free-standing Mg films by inspection of the scattering phase maps. To facilitate interpretation, we overlay these phase maps with the grain boundaries as extracted from the mechanical phase maps. We show these combined maps in Figure 3.13 for selected time steps of the in-situ hydrogen absorption process in Mg. To be able to show the same area of the Mg film during hydrogenation we have to compensate for sample drift between two subsequent sSNOM measurements but also during a single sSNOM measurement. This is done by pre-measurement re-positioning of the sample followed by a post-measurement drift correction. Here, we track the position of two fixed points in each frame at time  $t$  manually and compensate for the drift by shifting and stretching the  $x$ - $y$ -grid of the respective sSNOM scan. We obtain for each frame a  $x'$ - $y'$ -grid, where the pixels of each sSNOM scan correspond to the almost same positions of the Mg/MgH<sub>2</sub> film. Subsequently, we interpolate the respective data onto the original  $x$ - $y$ -grid and crop the area which lies within all sSNOM scans.

Our in-situ nanoimaging of the hydrogenation dynamics of Mg gives us the unique opportunity to understand the nanoscale hydride phase formation in Mg in detail. Before hydrogenation, we observe a nearly constant scattering phase over the entire field of view, indicating a pure metallic Mg state. After  $t = 2.5$  min, we see that the hydrogenation of Mg to MgH<sub>2</sub> starts at several positions simultaneously. Most probably, hydrogen enters the film via weak spots from below (see Figure 3.14, where we show a schematic drawing of the vertical MgH<sub>2</sub> formation). Please note that due to the finite thickness of the film as well as the hydrogen flow from below, we observe a superposition of vertical and lateral hydride phase propagation. The first hydride formation occurs directly at the grain boundaries, which matches our expectation as the grain boundaries are known as fast diffusion paths in Mg [147]. From here, hydrogen permeates laterally into adjoining grains/single nanocrystallites until they are fully loaded. Please note, as the hydrogen is delivered from below, the hydride formation might also have the possibility to start from the bottom edge of a grain / lower grain boundary. This nucleation and growth process dominates for the first ten minutes. Simultaneously, a hydrogenation front progresses from grain to grain, causing the size of the hydrogenated areas to grow until several of these areas combine. This leads to the formation of channels of MgH<sub>2</sub> all over the film surface. The width of these channels is on the order of several tens of nanometers and they are caused by hydrogenated and unhydrogenated Mg, which is in stark contrast to previous studies where similar linear arrangements on the tens of micrometers scale have been found

## Hydrogen Absorption

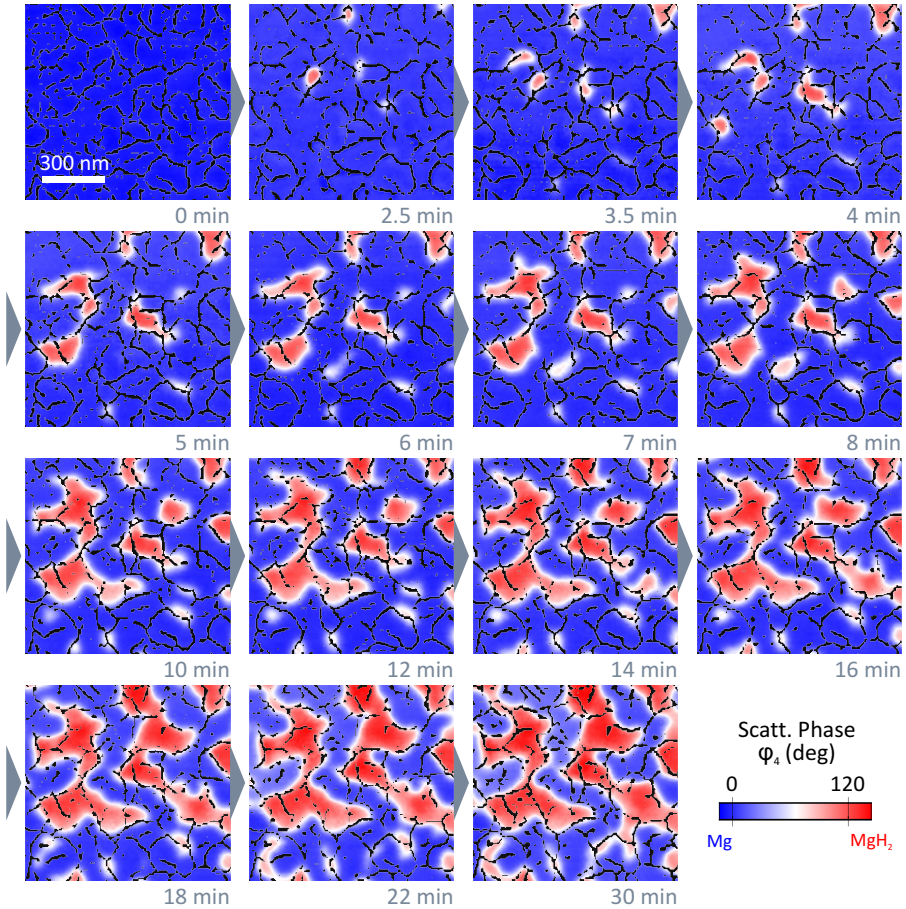


FIGURE 3.13. **Watching nanoscale hydrogen diffusion in Mg.** Chemically specific in-situ nanoscale imaging of the diffusion dynamics of hydrogen into a 50 nm Mg thin film. We plot 2D sSNOM images of the scattering phase  $\phi_4$  at several time-steps of the hydrogen loading process. All scans are performed with an illumination frequency of  $\nu = 1280 \text{ cm}^{-1}$ . Hydrogenated areas (dielectric  $\text{MgH}_2$ ) lead to a large shift of the optical phase compared to metallic Mg, as visualized by a blue-to-red transition. An overlay with grain boundary masks allows an excellent tracking of the  $\text{MgH}_2$  formation and a detailed study of the diffusion mechanism of hydrogen in Mg thin films. We find that hydride formation is nucleated at grain boundaries and is followed by a growth process of these nucleation centers. The hydrogenation front progresses from grain to grain until channels of  $\text{MgH}_2$  have formed all over the film surface. Interestingly, the phase formation stops although the surface is not completely switched from Mg to  $\text{MgH}_2$ .



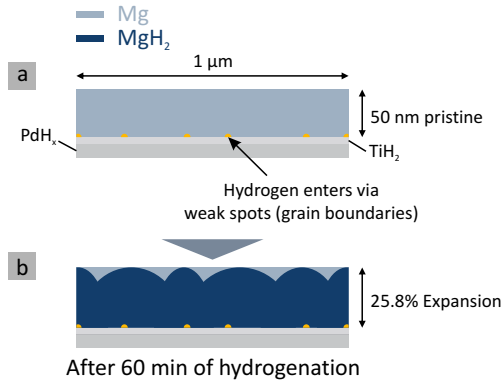


FIGURE 3.14. **Schematic drawing of the vertical  $\text{MgH}_2$  formation in a 50 nm Mg film.** (a) Hydrogen enters via weak spots at grain boundaries and diffuses vertically to the surface via the grain boundaries. From these nucleation centers the hydrogenation front progresses laterally. (b) After 60 min of hydrogenation, a closed layer of  $\text{MgH}_2$  blocks further hydrogen diffusion leaving areas at the top surface of metallic Mg. The average vertical expansion is 25.8%, close to 30% of a completely hydrogenated film.

[143].

After  $t = 20$  min, the hydrogen absorption becomes significantly slower. As schematically shown in Figure 3.14, we attribute this to the well-known formation of a blocking layer inside the Mg film [137, 171].  $\text{MgH}_2$  itself acts as a diffusion barrier for hydrogen and thus prevents continued hydrogenation of the film. Carefully comparing the optical phase maps, one can already qualitatively assess that the hydride phase front propagation stops after 30 min. This behavior can also be found quantitatively when examining the time dynamics of the hydrogenated area, which can be found in Figure 3.15 (solid purple line and squares). Interestingly, even after 60 min of hydrogen exposure and saturation, the film surface has not completely hydrogenated and shows a  $\text{MgH}_2$  content of only 38% in the probed surface layer. This means that unhydrogenated material is left, which is, on first sight, unexpected from literature for Mg [99], but has also been found in hydrogenated niobium films [172]. However, we explain this behavior, on the one hand, again with the formation of the blocking layer which halts the vertical hydrogen front progression [173], leaving areas at the surface in the pristine state (Figure 3.14). On the other hand, we expect that the thin  $\text{MgO}$  layer (approx. 5 nm), which forms on the surface, does not seal the Mg film completely. Additionally, as our samples are hydrogenated from below, Mg has no

direct exposure to hydrogen gas, but only Pd does (see Figure 3.8a). Due to the large volume expansion during hydrogenation of the rough Mg film, cracks form and can cause individual Mg grains to be decoupled from either adjoining Mg/MgH<sub>2</sub> grains or from hydrogen-delivering PdH<sub>x</sub>/TiH<sub>x</sub> below. Consequently, hydrogen can leak out at the top of the Mg surface as it can pass the Mg film without any contact to Mg and leave unhydrogenated areas/grains.

We have seen that our in-situ technique allows for tracking the hydrogenation of the metallic Mg film with very high spatial resolution, significantly larger as compared to conventional optical microscopy. Consequently, further analysis of the data shown in Figure 3.13 will in fact allow us to distinguish between the nanoscopic and the macroscopic hydride phase propagation dynamics in Mg, providing valuable insight into the fundamental hydrogenation processes. Already quantitatively, it can be seen that individual grains seem to switch on very short time scales compared to the progression of the hydrogenation in the entire film. The individual hydrogen loading times of four selected crystallites are extracted from the data shown in Figure 3.13 and are depicted in Figure 3.15 in direct comparison with the loading dynamics of the entire film. The data extraction works as follows: The hydrogen loading of the individual grain is tracked by determining the relative hydrogenated area  $A_{\text{MgH}_2}(t)/A_{\text{Grain}}$ , where  $A_{\text{MgH}_2}(t)$  is the total hydrogenated grain area at time  $t$  and  $A_{\text{Grain}}$  is the total size of the grain after hydrogenation. The data is shown color coded according to the marked positions of the grains in the scattering phase image of the pristine Mg film on the right. The same procedure is applied to determine the hydrogen loading dynamics of the entire film. Here, we used two different methods to normalize the hydrogenated film area  $A_{\text{MgH}_2}(t)$ . The solid line and squares represent the dynamics when normalizing to the area of the entire measured film (including unhydrogenated areas)  $\rightarrow A_{\text{MgH}_2}(t)/A_{\text{Entire Film}}$ . The dashed line represents the dynamics when normalizing only to the maximum hydrogenated area of the entire film  $\rightarrow A_{\text{MgH}_2}(t)/A_{\text{Hydrogenated Film}}$ . When comparing film and grains, we find that no matter which normalization we choose, the individual grains load much faster. From the inset in Figure 3.15, showing a zoom-in of 1 min - 10 min, we find that all grains are fully loaded within only a few minutes. In particular, grain 2 reaches a loading of 75% of its total surface area in less than two minutes. This behavior is a clear indication that the limited hydrogen diffusion in Mg films, as observed in many experimental studies, is in fact not related to the nanoscopic diffusion and is thus fundamentally limited but lies with the morphology of the film itself. After every individual grain the hydrogenation of the film stops and requires a new nucleation spot before the next grain transforms. This indicates that a tailoring of grain size as well as an increase

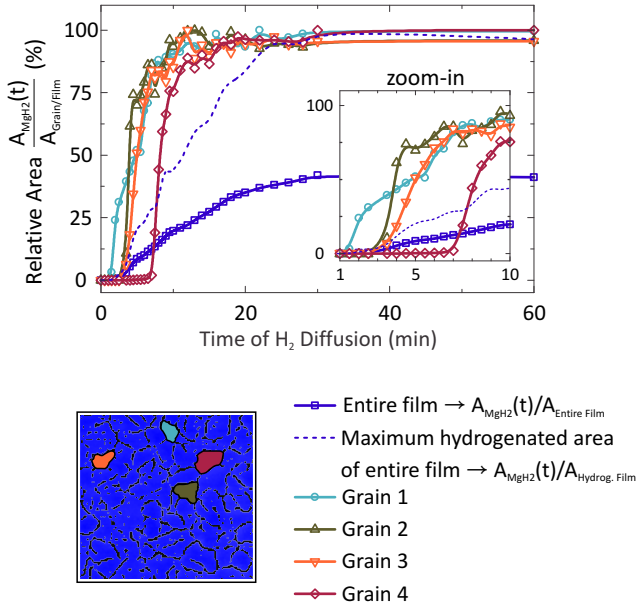


FIGURE 3.15. **Dynamics of the hydride phase propagation in individual grains vs. the entire film.** We plot the relative hydrogenated area  $A_{\text{MgH}_2}(t)/A_{\text{Grain/Film}}$  in dependence of the hydrogen diffusion time. The relative hydrogenated area is obtained by determining the total area of  $\text{MgH}_2$  (from the optical phase data shown in Figure 3.13) in four individual grains and in the entire film, respectively. Then we normalize it to the size of the respective grain and entire film, respectively. Additionally, we plot the relative hydrogenated area in the whole film when normalized to the maximum hydrogenated area of the entire film. The analyzed grains are marked in the near-field scattering phase image of the pristine Mg film on the right with the respective color. The inset shows a zoom-in of the time dependency of the hydride formation between 1 and 10 minutes, allowing for a better comparison of the loading times. The loading in individual Mg grains is significantly faster than the diffusion of hydrogen in the entire film. We observe, e.g., for grain 2, a loading of 75% of its area in less than 1 minute.

of the grain boundary or nucleation site density is a promising route to significantly decrease the film hydrogen loading times.

### 3.3.4 Vertical Expansion

As mentioned above, we observe significant amounts of pristine metallic Mg on the surface of our films, even after 60 min of hydrogenation. Comparing our results to literature findings, this behavior appears surprising as the film is expected to have fully hydrogenated after saturation [99]. This apparent contradiction can be explained when closely examining the changing film morphology and in particular the film expansion: Figure 3.16 depicts the topography of the film after 2, 10, 20, and 60 min of hydrogen exposure. The surface roughness changes drastically during the hydrogenation process. After 2 min, we find a finely structured surface with small peaks, which are mostly located at grain boundaries. After 10 min, the peaks are almost completely gone, and the film starts to expand quickly vertically and also most probably laterally. The more hydrogen is absorbed, the rougher the surface becomes, and large hills and valleys are formed after 60 min of hydrogen diffusion. From this topography we can calculate the local vertical expansion (Figure 3.17) by referencing the height value at each pixel to the corresponding height value of the pristine Mg film. This calculation is explained in detail in the following:

At first, we calculate the incremental vertical expansion between consecutive sSNOM scans. Afterwards, the total vertical expansion is obtained by summing up all previous incremental vertical expansions. In detail:

The incremental vertical expansion  $VE_{i,j}(t_n)$  of pixel  $i, j$  of the sSNOM scan at time-step  $t_n$  is calculated as

$$VE_{i,j}(t_n) = \frac{z_{i,j}(t_n) - z_{i,j}(t_{n-1}) - \Delta z(t_n)}{d_{\text{Mg}}}, \quad (3.63)$$

where  $z_{i,j}(t_n)$  is the height of the pixel at time-step  $t_n$ , where  $z_{i,j}(t_{n-1})$  is the height of the same pixel at the previous time-step  $t_{n-1}$ , and where  $d_{\text{Mg}} = 50$  nm is the total thickness of the pristine Mg film. During the hydrogenation, the film exhibits an overall bulging which we have to account for by introducing a correction factor  $\Delta z(t_n)$ . We define it as follows [143]:

Firstly, the lateral length scale of the bulging is large compared to the measured field of view (see Figure 3.8). Secondly, the time difference  $\Delta t = t_n - t_{n-1}$  between

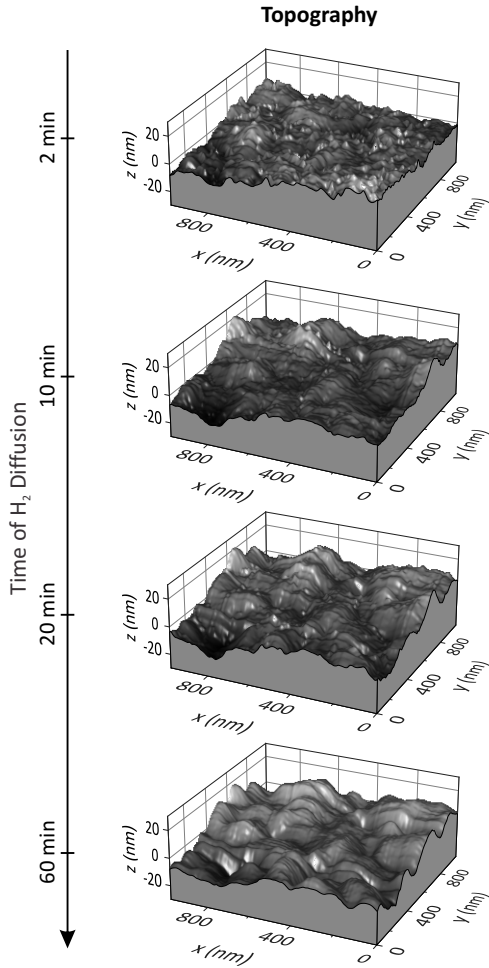


FIGURE 3.16. **Topography evolution of Mg during hydrogen loading.** 3D plots of topography of a Mg thin film after 2 min, 10 min, 20 min, and 60 min of hydrogen flow. First, there are small peaks appearing. The longer the hydrogenation takes, the rougher/more uneven the surface becomes with larger hills and valleys appearing.

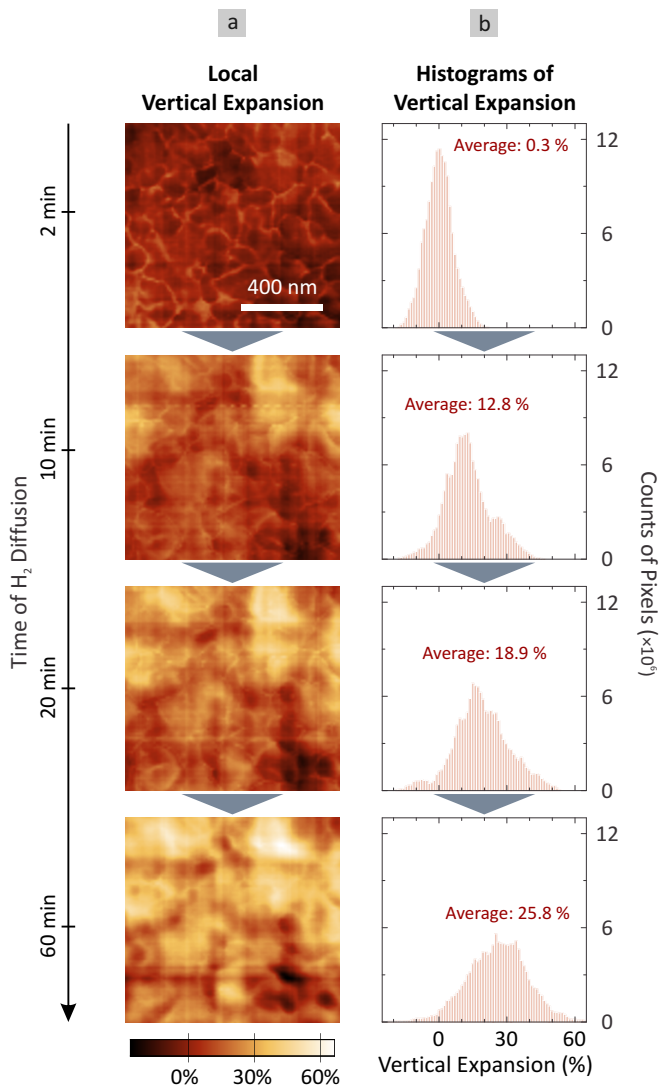


FIGURE 3.17. **Vertical expansion of Mg during hydrogen loading.** (a) 2D images of the local vertical expansion as well as (b) their histograms of a Mg thin film after 2 min, 10 min, 20 min, and 60 min of hydrogen flow. We find a local vertical expansion of more than 60%. The average vertical expansion is calculated by integrating each histogram.

two consecutive sSNOM scans is so small, that the change of the respective topography is small, too, and only small incremental height adjustments have to be made. This is the reason why we assume a constant height correction factor for all measured pixels. Additionally, as the film mostly expands in positive  $z$ -direction, the small changes of the topography happen at high film positions. Thus, we select a thin layer of pixels at low  $z$ -values to calculate the incremental correction factor  $\Delta z(t_n)$ . It is given as

$$\Delta z(t_n) = \overline{z_{2\text{ nm}}(t_n)} - \overline{z_{2\text{ nm}}(t_{n-1})}, \quad (3.64)$$

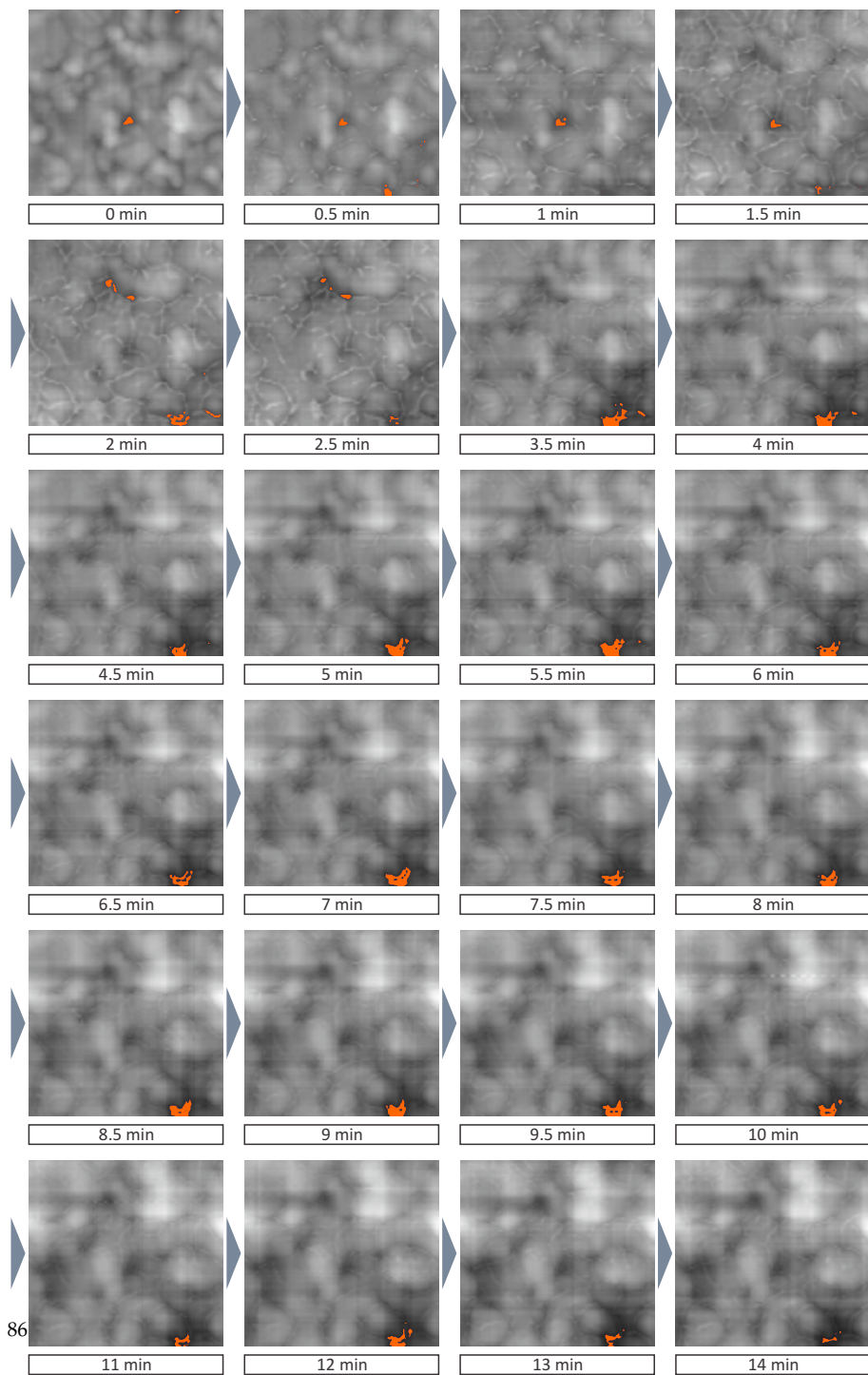
where  $\overline{z_{2\text{ nm}}(t_n)}$  and  $\overline{z_{2\text{ nm}}(t_{n-1})}$  denote the mean height value of all pixels at time-step  $t_n$  and  $t_{n-1}$ , respectively, which lie within the lowest 2 nm of the respective height scan. These pixels are marked in orange for each time-step in Figure 3.18 overlaid with the topography change during the hydrogenation process.

Please note that we cannot choose always the same pixels in every topography scan to calculate  $\Delta z$ . The reason lies within the local film expansion due to hydrogenation at individual areas. Additionally, it is almost impossible to perfectly correct the sSNOM data for a sample drift (see procedure above). This means that the pixels would not correspond to the exact same position of the film surface. Consequently, this would lead to a significant overestimation of the vertical expansion.

Finally, the total vertical expansion of each pixel  $i, j$  after time-step  $t_n$  is then calculated relative to  $t_0 = 0$  min by adding all previous incremental vertical expansions, namely

$$VE_{\text{tot},i,j}(t_n) = \sum_{k=1}^n VE_{i,j}(t_k). \quad (3.65)$$

We obtain the images shown in Figure 3.17a for 2, 10, 20, and 60 min. The respective histograms of these images are shown in Figure 3.17b. We find from the local vertical expansion that for the first 2 min the expansion is mostly limited to grain boundaries, where we observed the small peaks in the topography. Further film expansion is mostly limited to whole grains which expand in parts by more than 60%. Additionally, there are areas/grains which show a negative vertical expansion. This can be explained with our free-standing film. In contrast to a pinned film on a substrate, our film can expand during hydrogenation not only in positive but also in negative  $z$ -direction. This causes a large change of the surface roughness leading to very high but also small negative expansion values. In general, we find that the histogram of the vertical expansion becomes broader the longer hydrogen is absorbed, which coincides





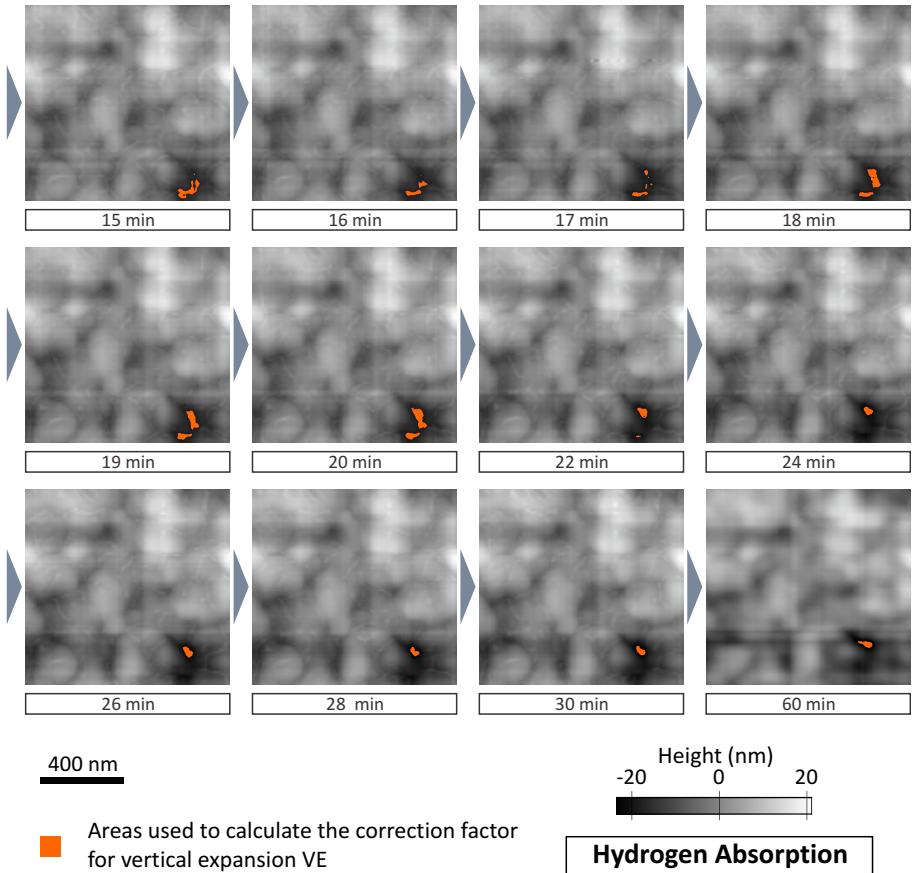


FIGURE 3.18. **Change of topography during hydrogenation.** Topography of the Mg hydrogenation time-series sSNOM scans with the respective pixels marked (orange) which are used to calculate  $\overline{z_{2\text{nm}}}$  for the correction factor  $\Delta z$  (bulging of film) for the vertical expansion in Figure 3.17. We only select the pixels whose  $z$ -values lie within the lowest 2 nm of a respective topography scan.

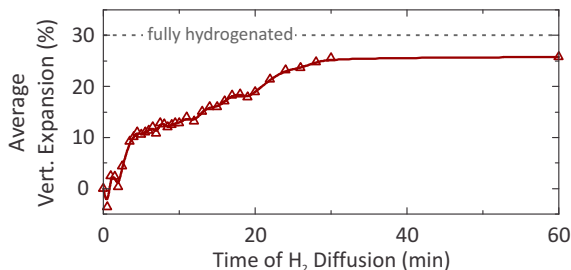


FIGURE 3.19. **Average vertical expansion of Mg thin film vs. hydrogen loading time.** For a fully hydrogenated Mg film, one would expect the expansion to be 30%. As the hydrogen absorption in our 50 nm Mg film has saturated while still areas of metallic Mg were left, we reach a maximum average vertical expansion of approximately 25%. This can be explained with the hydrogenation front propagation in vertical direction through the Mg film as indicated in Figure 3.14.

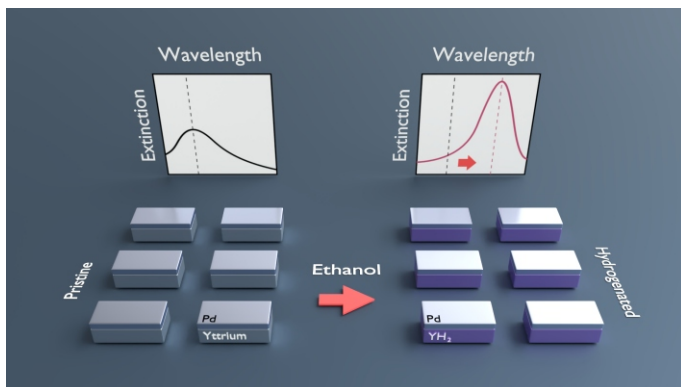
with the increase of the surface roughness for longer H<sub>2</sub> diffusion. In addition, the average vertical expansion, which is obtained by integrating the respective histogram, increases with longer hydrogen diffusion.

The evolution of the average vertical expansion over time is depicted in Figure 3.19. We reach a maximum average expansion of 25.8% after 60 min of hydrogenation. As already mentioned, a completely hydrogenated Mg film should expand on average by approximately 30% in volume. Our free-standing film is still clamped on the grid causing that most of the expansion is happening vertically and not laterally. The small lateral expansion leads to the bulging of the film. Consequently, our value of 25.8% results in a hydrogenated Mg volume of approximately 86%, meaning that most of the volume below the measured area of the Mg film has switched to MgH<sub>2</sub>. This finding alleviates the apparent contradiction observed in the data of Figure 3.13: Our in-situ sSNOM technique is highly surface sensitive and we are thus measuring mainly the surface (5-10 nm) of the film which retains significant metallic Mg while the film as a whole is close to fully hydrogenated. This behavior additionally supports our assumption of the formation of the blocking layer and the leakage of hydrogen at the top surface. We have thus found that, in contrast to common expectation for such a thin 50 nm film, a certain fraction of Mg remains metallic. This so far unknown aspect might offer additional adjustment possibilities for future material engineering. Furthermore, it was shown that quantitative investigations of vertical material compositions are possible using sSNOM measurements [174, 175]. Comparing

multi-layered finite dipole models with experimental tomographic sSNOM data will allow to study, e.g., the local hydrogenation depth in our Mg/MgH<sub>2</sub> films.

## 3.4 LIQUID HYDROGENATION OF YTTRIUM NANOANTENNAS

Besides using sSNOM to investigate the nanoscale hydrogen diffusion in metallic thin films, one can also utilize plasmonic nanoantennas made directly from hydrogen sensitive materials as local probe. Typically, they give a feedback on their nano-optical properties via spectroscopic measurements. In the following, we present a local nano-optical indicator which allows detection of hydrogenation of yttrium nanoantennas via the deprotonation of alcohols assisted by a catalytic Pd cover. While common hydrogenation schemes of Y rely on hydrogen gas exposure, we show that upon an exposure to liquid alcohols such as ethanol or methanol, Y can be hydrogenated at room temperature and ambient pressures. This Pd-catalyzed deprotonation/oxidation of alcohols is known in literature [176–179]. However, so far, it has not been possible to visualize such a deprotonation optically.



After proving the concept in the VIS spectral range with Y-Pd thin films, we demonstrate a plasmonic nanoantenna resonance shift of several hundred nanometers in the near-infrared (NIR) and MIR spectral range after ethanol exposure. By varying the length of the plasmonic nanoantennas, we confirm excellent tunability and modulation of the plasmonic resonances as necessary for future wide-range applications. Our liquid hydrogenation method and nano-optical deprotonation indicator paves the way towards a purely optical local monitoring and detection of hydrogen-involving chemical processes in liquid environments without further need of electrical, chemical, or electrochemical read-out. It will be possible to optically and locally track chemical

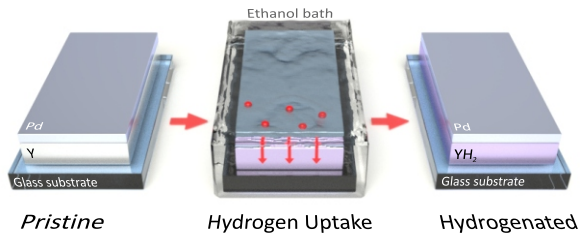


FIGURE 3.20. **Concept of liquid hydrogenation.** The pristine optical indicators consist of a 50 nm yttrium layer covered with a 20 nm catalytic palladium layer, as illustrated on the left. When placing such a sample in an ethanol bath (middle), the Pd layer causes the deprotonation of the ethanol and absorbs hydrogen (indicated by red spheres), which is then absorbed by the Y. After the immersion in the ethanol bath, the yttrium film has hydrogenated to a stable yttrium dihydride ( $\text{YH}_2$ ) state, as indicated on the right.

reactions where a local hydrogen indication is necessary, as for example during redox reactions in fuel cells to further improve their efficiency.

### 3.4.1 Concept

The main concept of our liquid hydrogenation scheme is illustrated in Figure 3.20. The hybrid optical indicators consist of stacked layers of Y and Pd on glass substrates as depicted on the left in Figure 3.20. This two-layered indicator is able to hydrogenate in an ethanol bath (Figure 3.20, middle), as the catalytic properties of Pd cause the deprotonation of ethanol and the hydrogen uptake of Pd and Y. As known from gasochromic hydrogenation experiments, in which the samples are exposed to gaseous  $\text{H}_2$  buffered in  $\text{N}_2$  or synthetic air, Y is an excellent candidate to visualize its hydrogen uptake optically. Similarly, after the liquid hydrogenation, the optical properties of Y have changed dramatically as stable yttrium dihydride ( $\text{YH}_2$ ) has formed (Figure 3.20, right). This phase transition from metallic Y in hcp configuration to metallic  $\text{YH}_2$  in fcc configuration comes with a strong increase in the electrical and optical conductivity. Consequently,  $\text{YH}_2$  is the preferred metal to exhibit a plasmonic resonance as we will show in the course of this work. Please note that the transition from Y to  $\text{YH}_2$  is non-reversible at ambient pressures and room temperature. In contrast, Pd is expected to return to its pristine state as soon as the layered system is taken out of the ethanol bath as we will discuss in the course of the manuscript. Consequently, as mentioned, our new liquid hydrogenation method allows for a local optical indication and detection

of chemical processes in liquids. We have to point out that due to non-cyclability it is unlikely to be suited for reversible optical switching applications.

### 3.4.2 *Material Investigation via Thin Films*

To prove our concept of liquid hydrogenation via the deprotonation of ethanol, we first study the change of the optical properties of  $\Upsilon$ -Pd thin films (50 nm  $\Upsilon$  + 20 nm Pd). The materials are evaporated subsequently via electron beam evaporation without breaking the vacuum. To keep the deposition conditions and thus the optical properties of the catalytic metals highly reproducible, we keep the deposition parameters (chamber pressure, deposition rate, film thicknesses, vacuumized material storage, etc.) identical for all samples shown in this work [45]. Figure 3.21 illustrates the change in the (a) reflectance and (b) transmittance spectrum in the VIS and NIR spectral range (500 nm to 900 nm). They are measured using a customized upright microscope spectroscopy system (NT& C NanoMicroSpec) referenced to an aluminum mirror (reflectance measurements) and to the bare substrate (transmittance measurements). The corresponding spectra of the film after immersion in ethanol are displayed in Figure 3.21a and b in red, the spectra for a gasochromic reference in blue, and the spectra of the pristine films in black. Numerical calculations of the reflectance and transmission spectra are plotted as dashed lines. The calculations are performed via a scattering matrix formalism [180]. The dielectric data of  $\Upsilon$  is taken from Weaver et al. [181], and the data for  $\Upsilon\text{H}_2$  is taken from van Gogh et al. [182]. We find that the optical properties change drastically upon ethanol and gas exposure. The reflectance of the thin films decreases from 0.6 to approximately 0.1 at 600 nm. Similarly, the transmittance increases by almost a factor of seven from a value of approximately 0.01 to a value of 0.07. This characterization of the spectral appearance allows for the determination of the material state of  $\Upsilon$  after the liquid hydrogenation in an ethanol bath. Strikingly, the reflectance as well as the transmittance spectra of the ethanol state and the gasochromic  $\Upsilon\text{H}_2$  state are nearly identical. This proves that the immersion in ethanol leaves the film in the hydrogenated  $\Upsilon\text{H}_2$  state.

Figure 3.21c shows the visual appearance of the backside of a pristine  $\Upsilon$  film (left) and of the same film after liquid hydrogenation in ethanol (right), taken in reflection (imaged through the glass substrate). The white balance is taken on the pristine Pd front side. We find, as expected, a silverish appearance of the pristine  $\Upsilon$ , whereas the film after the ethanol bath appears purple. As  $\Upsilon\text{H}_2$  becomes dielectric for  $\lambda < 800$  nm, this purple appearance is most likely due to a Fabry-Perot resonance in the  $\Upsilon\text{H}_2$  thin film which is tunable via the initial  $\Upsilon$  film thickness. This is known from previous work

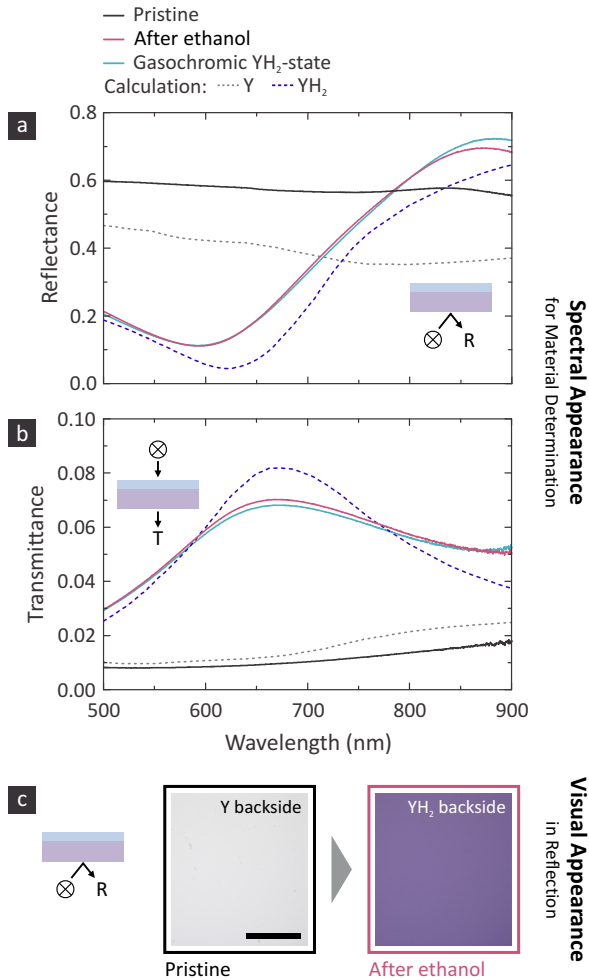


FIGURE 3.21. **Material investigation via thin films - proof of concept.** (a) Reflectance and (b) transmittance spectra of Y-Pd thin films in its pristine state (black solid lines), after ethanol bath (red solid lines), in a gasochromic  $\text{YH}_2$  state (blue solid lines), as well as calculated spectra for the pristine Y and hydrogenated  $\text{YH}_2$  state (dashed lines). The spectra of the gasochromic  $\text{YH}_2$  state and after ethanol agree very well, which implies also  $\text{YH}_2$  material after the ethanol bath. We assume the Pd cap layer to return to its pristine state after the ethanol immersion and subsequent ambient air exposure, as validated by calculations (see Figure 3.22). (c) Visual appearance of the backside of a pristine Y film and  $\text{YH}_2$  film after ethanol. The images are taken with a reflection microscope. The scale bar is 1 mm and is valid for both images.

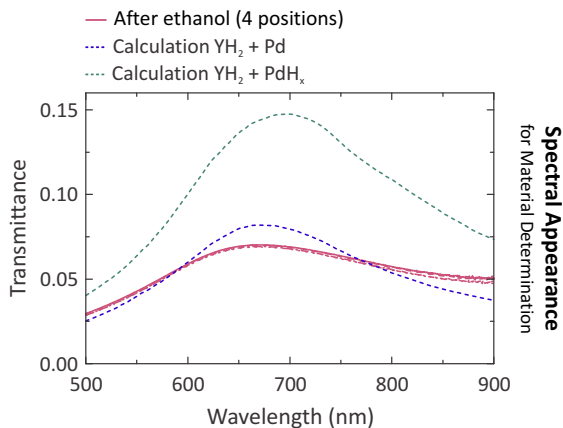


FIGURE 3.22. **Pd cap layer state after ethanol exposure.** Transmittance spectra of hydrogenated Y-Pd thin films after ethanol exposure (red, solid lines) as well as calculated spectra (dashed lines) with the cap layer being Pd (violet) and PdH<sub>x</sub> (green). We find that the calculation where the cap layer is in its pristine Pd state agrees well with the measured spectra. The calculation with hydrogenated PdH<sub>x</sub> cap layer over-estimates the transmittance obtained from the experiment by a factor of 2. Thus, we conclude that the PdH<sub>x</sub> present during the ethanol exposure dehydrogenates to Pd within seconds when the sample is exposed to ambient air before the measurement. In contrast, YH<sub>2</sub> remains in its hydrogenated state as this transition is non-reversible.

in literature [183]. Consequently, this resonance seems also to be the reason for the absorptive dip in the reflectance spectra of the hydrogenated YH<sub>2</sub> films in Figure 3.21a around  $\lambda = 600$  nm.

Furthermore, we assume the Pd cap layer to return to its pristine state after the ethanol immersion and subsequent ambient air exposure, as validated by calculations of different material stacks summarized in Figure 3.22. We find that the calculated transmittance through a YH<sub>2</sub>-PdH<sub>x</sub> material stack where the cap layer is still hydrogenated (green dashed curve) over-estimates the experimentally obtained values by a factor of 2. In contrast, we achieve a very good qualitative and quantitative agreement with the spectrum calculated for a YH<sub>2</sub>-Pd combination (violet dashed curve vs. red curves).

Additionally, we performed the experiments using a wider set of solvents, in particular of varying pKa value (a detailed discussion of the influence of the pKa value will



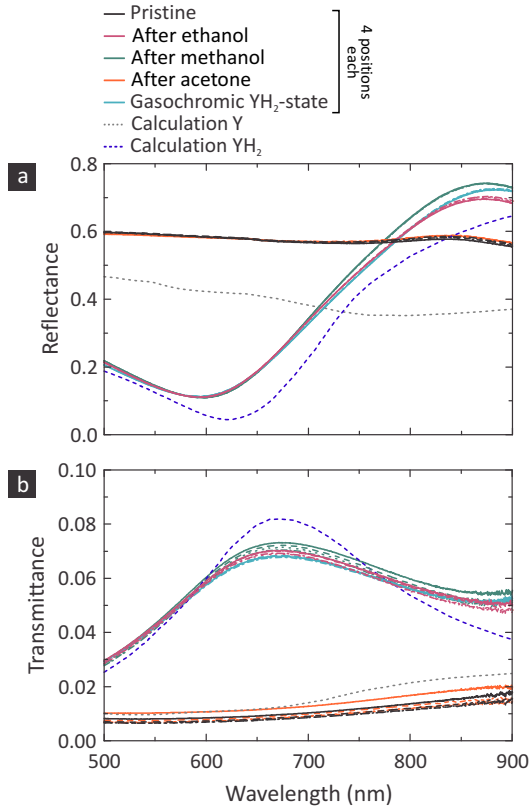


FIGURE 3.23. **Liquid hydrogenation of Y thin films with different alcohols.** (a) Reflectance and (b) transmittance spectra of thin films in a pristine state (black), after ethanol (red), after methanol (green), after acetone (orange), in a gasochromic  $\text{YH}_2$  state (blue), as well as calculated spectra for the pristine Y and hydrogenated  $\text{YH}_2$  state (dashed lines). The experimental data represents four different positions for each solvent. The spectra of the gasochromic  $\text{YH}_2$  state and after ethanol/methanol are almost identical and agree very well with the simulation.

follow in section 3.4.3). These results are shown in Figure 3.23. In addition to ethanol, we compare an immersion of  $\Upsilon$ -Pd films in baths of methanol (green) and acetone (orange). Overall, we observe a very similar hydrogenation of  $\Upsilon$  for ethanol and methanol. The quantitative agreement between ethanol, methanol, and the gasochromic state is remarkable, clearly underpinning the existence of  $\Upsilon\text{H}_2$ . In contrast, acetone (no alcohol) leaves the  $\Upsilon$  film unaffected and matches the pristine measurement.

Please note that Pd-capped yttrium is an ideal candidate to visualize this effect of liquid alcohol deprotonation. The reason lies with the very low hydrogen/proton partial pressure of only  $10^{-30}$  -  $10^{-25}$  bar necessary for the transition from  $\Upsilon$  to  $\Upsilon\text{H}_2$  to start in a controlled environment without oxygen [184]. In contrast, the transition to the  $\Upsilon\text{H}_3$  state starts at comparably high partial pressures of  $10^{-5}$  -  $10^0$  bar. Similarly, the phase transitions of pure Pd or other Pd-capped hydrogen-sensitive materials such as magnesium or niobium occur at similarly high hydrogen partial pressures, which are not reached by our liquid hydrogenation method. Please also note, that even via common gas exposure a transition to full stoichiometric  $\Upsilon\text{H}_3$  cannot be reached. Typical experiments with Pd-capped  $\Upsilon$  stop at a hydrogen content  $\Upsilon\text{H}_x$  of  $x \approx 2.7 - 2.9$  (under very high pressure  $x = 2.99$  can be reached) [48].

### 3.4.3 Temporal Investigation via Thin Films

For potential applications as optical indicator of local catalytic chemical processes it is important to understand the transition dynamics in more detail. Thus, we turn our attention to the temporal behavior of the transition from  $\Upsilon$  to  $\Upsilon\text{H}_2$ . Figure 3.24a depicts the spectral change in reflection during the liquid hydrogenation upon ethanol exposure. For clarity we plot spectra every 8 min of ethanol exposure. The temporal spectral change clearly indicates the transition from the pristine  $\Upsilon$  state (black) to the hydrogenated  $\Upsilon\text{H}_2$  state (red) as the Fabry-Perot mode around  $\lambda = 600$  nm becomes more and more pronounced, causing the reflectance to drop significantly. As seen in the time trace of the reflectance at  $\lambda = 600$  nm in Figure 3.24b, the liquid hydrogenation of  $\Upsilon$  in the ethanol bath saturates after approximately 120 min (red curve). Further, acetone leaves the  $\Upsilon$ -Pd films unaffected as no hydrogen uptake via Pd is taking place (orange curve). At this point we have to discuss the potential reason for this liquid hydrogenation in ethanol. As mentioned above, we believe that the catalytic Pd layer causes a deprotonation of the alcohols, as it is known in case of Pd nanoclusters [178, 185]. As the ability to deprotonate a solvent is directly related to its pKa value, the hydrogenation speed should depend on the pKa value of the solvent being used. The lower the pKa value, the more likely is the deprotonation of the solvent, in turn speed-

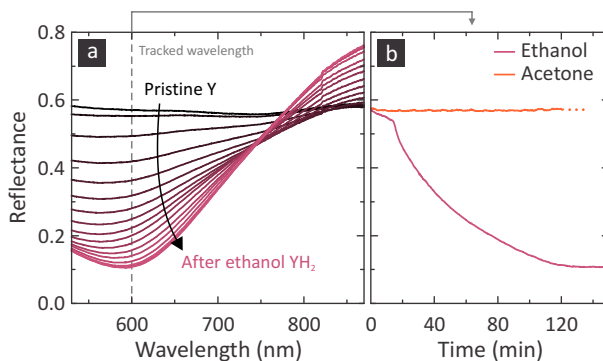


FIGURE 3.24. **In-situ temporal investigation of liquid hydrogenation of Y thin films.** (a) Reflectance spectra at every 8 min of the ethanol exposure. The transition from pristine Y (black) to YH<sub>2</sub> (red) is clearly observed. (b) Time trace of the change of the reflectance at a wavelength of 600 nm for ethanol exposure (red curve). For comparison, the time trace for acetone (orange) is depicted. Acetone leaves the pristine Y film unaffected.

ing up the liquid hydrogenation. However, a lower pKa value also implies a stronger acid which means that it becomes increasingly likely that highly reactive materials such as Y degrade.

#### 3.4.4 Nanooptical Indicator for Deprotonation

For local detection of chemical reactions, it is necessary to transfer this hydrogenation concept to the micro- or nanometer scale. Our design of a local nanooptical indicator of the ethanol deprotonation is depicted in Figure 3.25a. We use plasmonic nanoantennas made from Y and Pd with a plasmonic resonance in the NIR and MIR spectral ranges. These nanoparticles hydrogenate and change to YH<sub>2</sub> upon the liquid ethanol exposure and thus cause a large shift of the plasmonic resonance. The nanoparticles are fabricated via electron beam lithography (EBL) and subsequent metal deposition via electron beam evaporation with a subsequent lift-off process. The pristine antennas have a length of 460 nm, a width of 190 nm, and a height of 70 nm (50 nm Y + 20 nm Pd cap). The periodicity of the antenna array is 700 nm in x- and y-direction. An SEM image of the fabricated pristine array is depicted in the upper panel (black) of Figure 3.25b. The geometrical parameters lead to a somewhat weakly modulated plasmonic resonance of the pristine Y nanoantennas with a center wavelength at around 1390 nm, as shown in Figure 3.25a (black curve). The spectra are measured with a commercial Fourier transform infrared spectroscopy system (Bruker Vertex 80 with

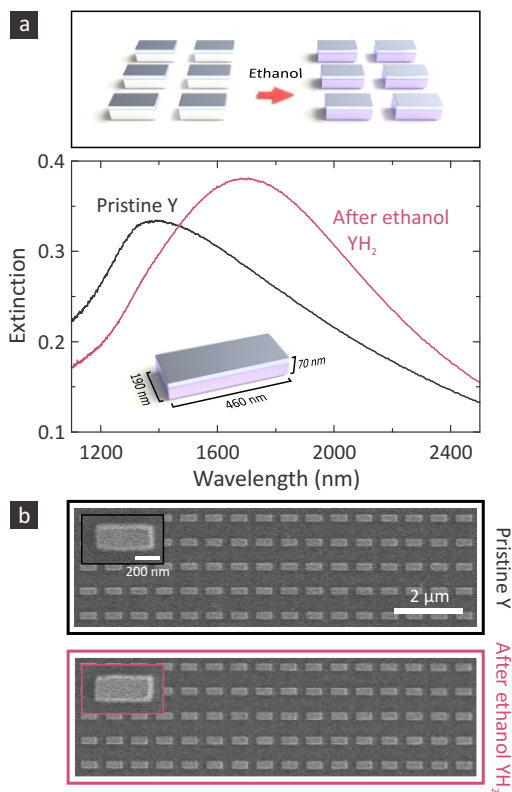
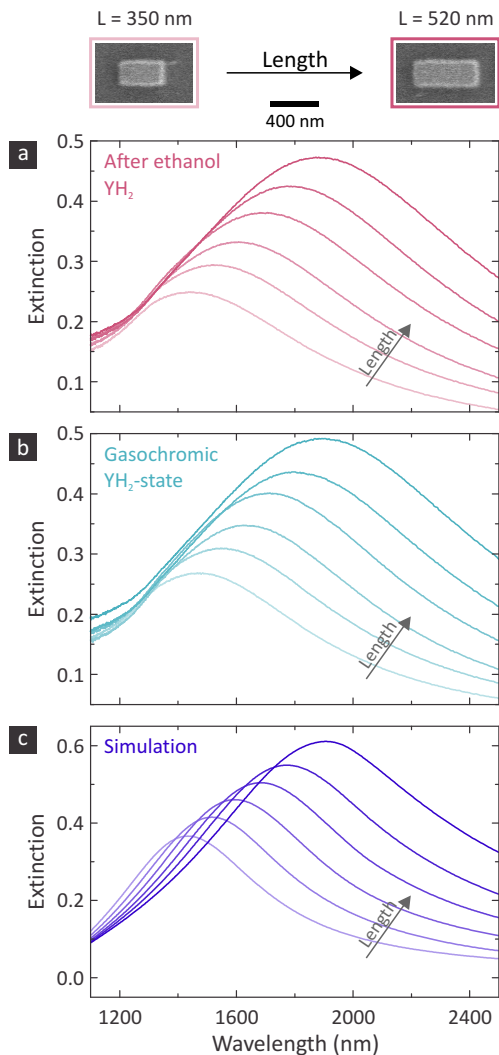


FIGURE 3.25. **Nanooptical indicator for deprotonation process - hydrogenation of plasmonic nanoantennas.** (a) Schematics of Y plasmonic nanoantennas hydrogenating in ethanol to metallic YH<sub>2</sub> (upper panel) as well as the corresponding change of the extinction spectra (lower panel). The pristine antennas have a length of 460 nm, a width of 190 nm, and a height of 70 nm (50 nm Y + 20 nm Pd). The periodicity of the array is 700 nm in x- and y-direction. The plasmonic resonance for pristine Y (black curve) shows a peak wavelength at around 1390 nm and is somewhat weakly modulated. After the ethanol bath (red curve) the plasmonic resonance has red-shifted to a peak wavelength at around 1700 nm and is well modulated. (b) scanning electron microscopy (SEM) images depicting the nanoantennas in its pristine state (black, upper panel) and after ethanol (red, lower panel). Although there has been a hydrogen uptake, no degradation or noticeable volume expansion is observable. The large scale bar is 2 μm. The small scale bar for the inset SEM images is 200 nm.

Hyperion 3000 microscope). This rather broad plasmonic resonance is caused by the low electrical conductivity of  $\Upsilon$  [182, 186]. The actual existence of a resonance is mostly due to the 20 nm Pd cap. After the ethanol exposure we find the nanoantennas switched to the  $\Upsilon\text{H}_2$  state which, as shown above, causes a strong change in the optical properties. Consequently, the resonance of the nanoantennas shifts by more than 300 nm to a center wavelength of around 1700 nm, demonstrating excellent spectral separation between the pristine and hydrogenated state. Furthermore, the resonance is now well modulated as the conductivity of  $\Upsilon\text{H}_2$  is strongly increased in comparison to  $\Upsilon$ , which is caused by a change in the atomic and electronic structure upon hydrogen uptake [187]. Please note that both measurements in Figure 3.25a are taken when the sample is completely dry - once before (black curve) and once after (red curve) the ethanol exposure. This means that there is no liquid present during the measurement, which could have caused the red-shift of the plasmonic resonance due to a refractive index change of the surrounding medium. An SEM image of the  $\Upsilon\text{H}_2$  nanoantennas after ethanol exposure is shown in the lower panel (red) in Figure 3.25b. We find no deformation or noticeable expansion of the nanoantennas after hydrogenation. The reason lies with the comparably small volume expansion of only approximately 5% when  $\Upsilon$  changes to  $\Upsilon\text{H}_2$  [188]. This conclusively demonstrates that the change and shift of the plasmonic resonance of our nanooptical indicator in Figure 3.25a is almost solely caused by the change in the electronic and consequently optical properties of the plasmonic nanoantennas upon ethanol deprotonation and hydrogen uptake.

In order to utilize yttrium nanoantennas as, e.g., nanooptical plasmonic indicator, one has to be able to tune the plasmonic resonance over a wide spectral range. Thus, we vary the length of our plasmonic nanoantennas from  $L = 350$  nm to  $L = 520$  nm while keeping the width (190 nm), the height (70 nm), and the periodicity (700 nm in  $x$ - and  $y$ -direction) constant. The spectral evolution of the corresponding plasmonic resonances is depicted in Figure 3.26 for  $\Upsilon\text{H}_2$  nanoantenna arrays which have been switched via (a) an ethanol bath and (b) gasochromically. Overall, we find perfect tunability of the plasmonic resonance and an excellent agreement between both experimental hydrogenation schemes. This underlines the exceptional power of our alcohol deprotonation technique to hydrogenate  $\Upsilon$  nanoantennas without the need for explosive hydrogen gases. Furthermore, Figure 3.26c illustrates the corresponding simulated plasmonic nanoantennas. The simulations are carried out with the frequency domain solver of CST Microwave Studio. As the nanoantennas in experiment form a native yttrium oxide ( $\Upsilon_2\text{O}_3$ ) layer we include a 3 nm thin  $\Upsilon_2\text{O}_3$  shell in the simulations. Furthermore, the nanostructuring processes (PMMA masking and development, lift-off etc.) can introduce small defects and impurities in the  $\Upsilon$  nanoantennas. To

compensate for this degradation in the simulation we increase the free electron damping in the respective dielectric function [48]. Consequently, we achieve very good agreement between experimentally measured and simulated  $\text{YH}_2$  nanoantennas. In the experiments, the length tuning allows for a shift of the plasmonic resonance from approximately 1440 nm to 1890 nm. This closely matches the overall expected shift and absolute center position from the simulations.



**FIGURE 3.26. Plasmonic resonance tuning via ethanol, gasochromic comparison, and simulation of  $\text{YH}_2$  nanoantennas.** Extinction spectra of  $\text{YH}_2$  plasmonic nanoantennas (a) after ethanol (b) after gas exposure, and (c) simulated. The length of the antennas varies from 350 nm to 520 nm. The width is 190 nm and the height is 70 nm (50 nm  $\text{YH}_2$  + 20 nm Pd). The cap layer for the simulations is in a Pd state as the samples are exposed to oxygen during the measurement and thus the  $\text{PdH}_x$  present during the ethanol/gas exposure is expected to dehydrogenate to Pd within seconds. In contrast,  $\text{YH}_2$  remains stable at oxygen exposure at room temperature and ambient pressure.

### 3.5 CONCLUSIONS & OUTLOOK

In conclusion, we have investigated in this chapter two hydrogen-sensitive metals which can be used for several applications in active plasmonic systems:

In the first part, we watched and analyzed in detail the nanoscale hydrogen diffusion dynamics in magnesium in an in-situ environment using sSNOM. A characteristic IR phonon resonance of  $\text{MgH}_2$  enabled chemical specificity to unambiguously track the hydride formation, nucleation, and lateral growth. We find that this process is highly influenced by the nanoscale morphology of the Mg film. This morphology seems to be mainly responsible for the slow hydrogen diffusion through the entire film. Interestingly, the hydrogenation stopped before the entire film is switched, leaving areas of metallic Mg within the dielectric  $\text{MgH}_2$ . From the analysis of the local as well as the average vertical expansion we can deduce that a  $\text{MgH}_2$  blocking layer has formed below the surface preventing further hydrogen diffusing through the film. In addition, we have proven that individual Mg grains show hydrogen loading dynamics which are significantly faster than the dynamics on the macroscopic film scale. This behavior is caused by an effective averaging over single nanocrystallites and grain boundaries. Thus, we expect, on the one hand, thin films with large monocrystalline grains to exhibit a significantly faster overall hydrogen diffusion coefficient. On the other hand, as our findings have shown that the hydrogenation requires nucleation at grain boundaries, an increased grain boundary density should also speed up the overall hydrogenation process. This could explain the significant improvement of hydrogen diffusion coefficients in alloyed Mg systems, such as  $\text{Mg}_x\text{Ni}_y$  thin films in which we observe very small grains and thus large grain boundary densities [189]. Our findings have immediate implications for a number of active optical and plasmonic systems, where magnesium but also other phase transition materials are being used. Our work is an important step forward in enhancing and understanding the diffusion kinetics, dynamics, and efficiency of phase change and as well as a huge variety of hydrogen storage and generation materials.

In the second part, we have demonstrated a novel method to hydrogenate yttrium films as well as yttrium nanoantennas in a liquid environment. We have carried out a proof of concept via alcohol hydrogenation of Y thin films to  $\text{YH}_2$  and have shown excellent agreement with gasochromically switched films as well as with calculated optical responses. Our presented local nanooptical indicators for the deprotonation of alcohols consist of periodically arranged plasmonic nanoantennas realizing a resonance with great oscillator strength and wide tunability in the NIR and MIR spectral



range. Upon alcohol exposure, the plasmonic resonance shifted by several hundreds of nanometers, leading to an excellent distinguishability between the pristine and hydrogenated state. Again, a comparison with gasochromically hydrogenated as well as simulated  $\gamma\text{H}_2$  nanoantennas revealed excellent agreement. These findings have immediate implications in hydrogen-regulated optical and chemical systems and can lead to applications where a hydrogen detection and indication in liquids is required. A utilization of our liquid hydrogenation scheme in other metal hydride systems or hydrogen sensitive materials such as metal organic frameworks could, in the future, even allow for a reversibility of the liquid hydrogenation process. Volumetric detection limits of chemical reactions and catalytic processes in liquids can be even further pushed by using and investigating single plasmonic particles as local nanoprobe instead of the entire nanoantenna array. Furthermore, our work can be highly beneficial for a better understanding of chemical reactions in liquids as it paves the way towards accessing and visualizing the reaction optically and locally without the necessity of an additional electrical, chemical, or electrochemical readout.



This chapter is based on the following published work:

- **J. Karst**, N. H. Cho, H. Kim, H.-E. Lee, K. T. Nam, H. Giessen, and M. Hentschel  
*Chiral Scatterometry on Chemically Synthesized Single Plasmonic Nanoparticles*  
ACS Nano **13**, 8659 (2019).
- **J. Karst**, M. Hentschel, N. H. Cho, H. Kim, K. T. Nam, and H. Giessen  
*Plasmonic Materials and Metastructures: Fundamentals, Current Status, and Perspectives*  
Chapter: Chiral Plasmonics  
Book edited by S. Gwo, A. Alù, Y.-J. Lu, X. Li, and C.-K. Shih  
Elsevier, expected publication date: 2023

#### 4.1 INTRODUCTION

A chiral object cannot be superimposed onto its mirror image by simple translation or rotation. The original and its mirrored object are so called true enantiomorphs or enantiomers of each other. Typically, they are termed right- and left-handed. Chirality is nearly omnipresent in our everyday lives, as the handedness of chemical substances is crucial to determine the basic functionality of key molecules, amino acids, proteins, drugs, and others. Similarly, the phenomenon of chirality has drawn lots of attention in physical research fields, especially in the optics and plasmonics community. Light itself can possess helicity or chirality, defined via its polarization. Here, one typically distinguishes right-circularly polarized (RCP) and left-circularly polarized (LCP) light which are differentiated by a clockwise or anti-clockwise rotation of the electric and magnetic field vectors.

Recently, chiral plasmonic structures have gathered significant interest due to the manifold potential and suspected applications, such as polarization control and manipulation [190–195], chiral sensing [196–199], three-dimensional chiral rulers [200, 201], switchable chiral systems [202–204], and many more [205–208]. However, al-

ready from a very fundamental and basic viewpoint, people have been captivated by plasmonic chirality [201, 209–219]. The reason lies with their molecular counterparts: Chirality, or the structural handedness of molecules, manifests itself optically in a different absorption for LCP and RCP light. Consequently, the polarization state of light can be manipulated: circular dichroism (CD) leads to differential absorption, and optical rotatory dispersion (ORD) causes the plane of linearly polarized incident light to be rotated. However, all of these effects are small for molecules due to their small light interaction cross sections. This is in stark contrast to plasmonic systems. Here, extremely large asymmetry has been found, which is linked to the enormous dipole strength of the plasmonic resonances. Additionally, the chiral response can be tailored as there is significant control over composition, relative orientation, position, shape, and size of individual plasmonic nanoparticle (NP)s [220–222]. Moreover, it was found that the chiral response of plasmonic systems is more diverse as in the case of molecular systems as plasmonic nanoparticles scatter and absorb light, leading to chiroptical effects in absorption as well as scattering [223].



There are mainly two possibilities to fabricate chiral plasmonic nanoparticles. On the one hand, top-down fabrication methods, such as electron-beam lithography, allow for a very high control of the individual nanoparticle shape and their relative position resulting in three-dimensional multilayer nanostructures [224–227]. On the other hand, the interest in bottom-up synthesis techniques is mainly fueled by the scalability of these methods, allowing, in principle, to manufacture the large quantities of nanoparticles required in real-world applications. The goal of the synthesis, however, is to fabricate nanoparticles, which do not only show similar shape but also possess similar optical properties. Consequently, significant effort has been undertaken to refine the nanoparticle synthesis. Such a refinement requires feedback. In most studies, this

feedback is the structural investigation of the nanoparticles via scanning electron microscopy (SEM) or transmission electron microscopy (TEM). However, in most cases, the optical properties are, in fact, key for future applications, which makes the optical properties appear highly appealing as a potential feedback.

In that sense, one question stood out from the beginning: What is the ultimate limit in the chiroptical response? How does one maximize the asymmetry of these plasmonic systems? More specifically, what is the ideal structure leading to the largest chiroptical response? In particular, the relation between the nanoscale morphology and the optical properties is of utmost interest, however, difficult or even impossible to determine. This holds, in particular, true for chiral geometries in which minute morphological differences can manifest themselves in pronounced chiroptical differences [108].

Recently, a water-based chemical synthesis route to fabricate three-dimensional chiral metal nanoparticles utilizing cysteine and cysteine-containing peptide additives as chiral shape modifiers has been presented [228]. This strategy has provided a possibility to synthesize various chiral helicoidal nanomaterial series and allowed a controlled bottom-up fabrication of solid symmetric left-handed and right-handed (as well as achiral) nanoparticles [229, 230]. The nanoparticles of these series exhibit an exceptional chiroptical response with an ensemble asymmetry factor of up to  $g = 0.2$ , while offering full tunability of the material properties via the synthesis. Nevertheless, further improvement of the chiroptical properties requires a deeper understanding of the working principles in these chemically synthesized helicoid NPs. In this chapter, we will show that single particle chiral scatterometry is one possible method which is ideally suited (in combination with SEM techniques) as an in-depth investigation method for the correlation between nanoscale morphology and far-field optical properties.

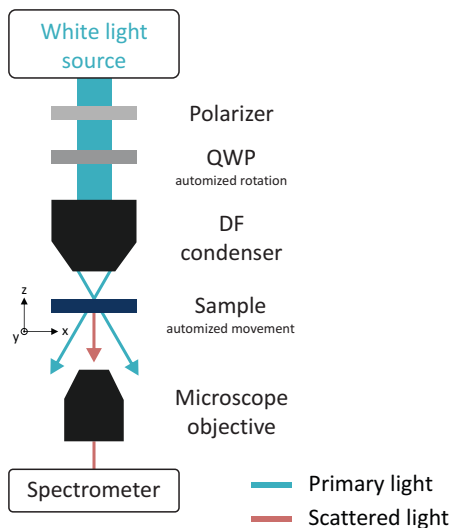


FIGURE 4.1. **Automized single particle chiral scatterometry.** Scheme of the optical transmission setup to automatically measure single NP chiroptical responses. The illumination unit consists of a high intensity white light source, a polarizer, and a quarter wave plate (QWP) to generate circularly polarized light, as well as a dark-field (DF) condenser to focus the light on the sample. The sample is mounted on an xyz-stage to automatically scan the measurement area over the sample. The detection path contains a microscope objective, which collects the scattered light from the NPs, and a spectrometer.

## 4.2 INSTRUMENTATION: CHIRAL SCATTEROMETRY

To investigate the Rayleigh scattering of single chiral plasmonic NPs, we use a modified dark-field microscope (Nikon Eclipse TE2000-U) [108]. A scheme of the setup is shown in Figure 4.1. We place the NPs onto glass substrates at the sample position on a motor driven xyz-stage. With a high-intensity laser-driven plasma white light source (Energetiq EQ-99) and a subsequent combination of linear polarizer (Thorlabs LPVIS100) and broadband QWP (B. Halle RAC 5.4.20) we generate circularly polarized light. The QWP is rotated automatically to switch between LCP and RCP light, which is focused via a DF condenser onto the individual structures. Due to the high numerical aperture ( $NA = 0.8 - 0.95$ ) of the condenser, only the scattered light in forward direction (indicated by red lines in Figure 4.1) is collected by the objective (magnification 60x). The primary light (blue lines) passes the objective. This allows us to resolve a single NP and detect its chiral scattering spectrum with a grating spectrometer (Princeton Instruments SP2500i) in combination with a Peltier-cooled front-illuminated CCD

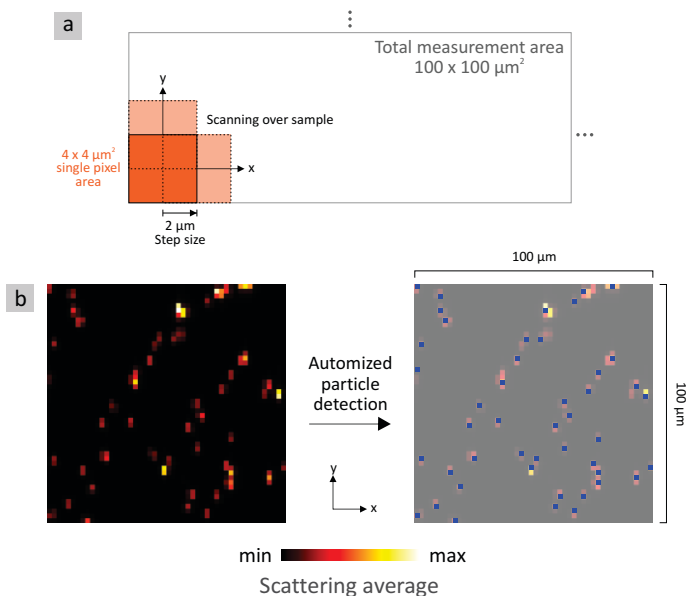


FIGURE 4.2. **Measurement procedure for automated chiral scatterometry.** (a) Measurement scheme illustrating the scanning of a  $4 \times 4 \mu\text{m}^2$  single pixel area over a total measurement area of  $100 \times 100 \mu\text{m}^2$  on the sample. The scanning increment is  $2 \mu\text{m}$  to ensure that all measured particles are once in the exact focus and close to the center of the illumination spot. (b) Obtained image from an automated scan showing the average scattering intensity (left). The particles are detected (right, blue squares) and spectroscopic information is extracted automatically.

camera (Acton PIXIS 256E).

With our setup it is possible to automatically measure single particles via an automated sample scanning as illustrated in Figure 4.2a. For an individual “pixel” of such a scanned image we illuminate an area of approximately  $4 \times 4 \mu\text{m}^2$ . Subsequently, this pixel area is scanned over the sample with a step size of  $2 \mu\text{m}$  in  $x$  and  $y$  direction. Due to the comparably large single particle spacing, achieved by spin coating a dilute particle solution, this incremental step ensures that one particle is measured without the influence of surrounding particles. Additionally, we choose the incremental step such that we can ensure a single NP is once in the exact focus and close to the center of the illumination spot. At each position we automatically measure the scattering spectra for an illumination with RCP and LCP light (automatic rotation of the QWP)

to retrieve the full chiroptical spectral information of the pixel/NPs. An exemplary scanned image of a sample containing single plasmonic nanoparticles is shown in Figure 4.2b. The left shows the forward scattering average intensity of a sampling area of  $100 \times 100 \mu\text{m}^2$ . We use post-processing of the scanned image to automatically detect the pixels containing single particles, as it is illustrated in Figure 4.2b on the right. The chiroptical spectral information at these positions is extracted and all particles are analyzed in detail and fully automatically.



## 4.3 CHIRAL SCATTEROMETRY ON SINGLE HELICOID NANOPARTICLES

4.3.1 *Single Helicoid Nanoparticles*

Schematic representations of the ideal shape of our single L-handed and D-handed helicoid NPs as well as the achiral hexoctahedrons are shown in Figure 4.3 on the left. For helicoid NPs with the highest  $g$ -factor, uniform sized  $\{111\}$  facet enclosed gold octahedron NPs are used as pre-synthesized low-index seeds. Under normal growth condition, achiral hexoctahedron nanoparticles composed of 321 facets on 48 identical triangular faces with  $4/m\bar{3}2/m$  point group symmetry were synthesized. Upon addition of the chiral glutathione molecule as chirality encoder, a preferred interaction between L-glutathione with the generated 321R facet in the hexoctahedron leads to a slower development of the R region. This shifts the R-S boundary towards the S region, whereas the counter-enantiomer shifts the R-S boundary towards the R region. This asymmetric growth breaks the mirror and inversion symmetry for the 432-point group symmetry generation. Viewed from the [100] direction, convex inner edges, highlighted in the achiral hexoctahedron in Figure 4.3, rotate in clockwise and anticlockwise direction, resulting in pinwheel-like structures with four highly curved arms on each six faces of the cubic geometry. These chiral arms evolve away from the center point as increasing its thickness, therefore, generating high-curvature gaps (chiral cavities).

After synthesis, the NPs are dispersed on a glass substrate via spin-coating at high speed which separates them spatially. While also preventing near-field interactions, it more importantly allows for single particle measurements as the scattered light from a single particle can be recorded only for a certain minimal inter-particle distance due to the size of the far-field focus, typically on the order of one resonance wavelength. The glass-air interface can introduce measurements artifacts due to the lowered symmetry. In order to measure the chiroptical properties of the NPs immobilized on the surface, it is important to remove the local structural asymmetry and any potential contribution caused by this asymmetry. We thus spin-coat a thin polymer layer (Futurrex IC1-200 spin-on glass) onto our samples. The particles are afterwards embedded into a homogeneous material consisting of the glass substrate and the spin-on glass polymer layer with same refractive index, which is crucial for avoiding symmetry breaking at the substrate-air interfaces.

SEM images of four representative L-handed, achiral, and D-handed single NPs without the polymer coating are depicted on the right in Figure 4.3. When comparing the

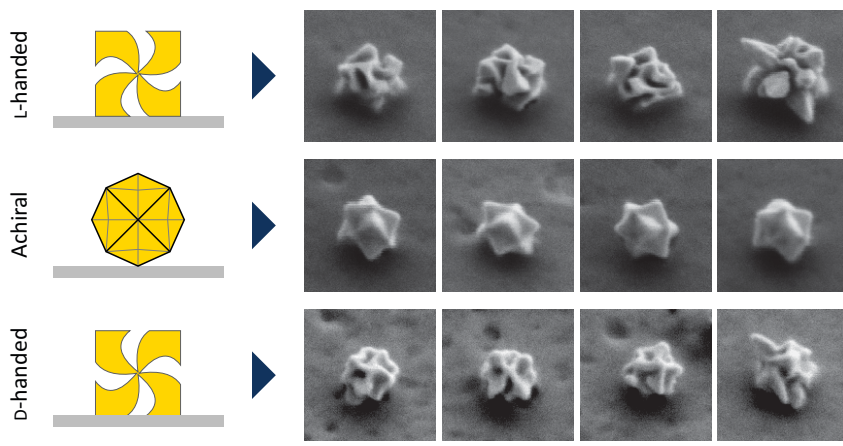


FIGURE 4.3. **Single helicoid chiral nanoparticles.** Left: Schematic illustration of single chiral plasmonic NPs showing the left-handed (L-handed), achiral, and right-handed (D-handed) structure. The achiral hexoctahedrons are the seeds for the growth of the two enantiomers. Right: Representative SEM images showing four L-handed, achiral, and D-handed single NPs. We find clear structural differences between the single L-handed and D-handed helicoid NPs, respectively. In contrast, the achiral hexoctahedrons show very little visible structural differences. The scale bar is 200 nm.

shapes of the synthesized particles with the schematic illustrations on the left, we find that both, L-handed and D-handed helicoids, possess the pinwheel-like morphology. The first two enantiomeric NPs clearly show the clockwise and anticlockwise rotation of the chiral arms with respect to the center symmetry point. Despite a consistent generation of a chiral motif, artifacts can exist within a batch and in between batches as slight deviations from the optimum synthesis conditions which can influence the chiral nanoparticle morphology significantly. In that sense, a “chiral motif” in our terminology means a common and persistent structural or also spectral feature (see below) which is present on average in most single nanoparticles. Representative artifacts of nanoparticle morphologies are shown in the SEM images of the two enantiomers in Figure 4.3. Some of the NPs have chiral features which possess underdeveloped curved arms (third L-handed particle) and some with overdeveloped protruded and extended arms (fourth L-handed particle). Additionally, we see slight size difference between the L-handed and D-handed NPs. The achiral hexoctahedrons show significantly less structural spread, having similar shape and dimensions. For a comprehensive understanding of the synthesis and a quantification of the synthetic potential, it is now important to correlate the morphological differences with the spectral response. A pri-

ori, it is not clear which of the particle morphologies visible in Figure 4.3 will exhibit the strongest chiroptical response. Moreover, it is not clear which spectral signatures will survive ensemble averaging.

As mentioned, we immobilized spin-coated L-handed, achiral, and D-handed nanoparticles on different substrates. As the particles are embedded into the spin-on glass their position and orientation is fixed and we can locate specific particles again, allowing to re-measure the spectra as well as to measure the same spots for different illumination, e.g., from the back- or front side. In order to obtain reliable spectral information and a decent overview of the spectral spread, it is indispensable to have large enough sampling as well as un-biased automated particle selection.

#### 4.3.2 *Scattering and Differential Scattering*

Our quantitative study compares the chiroptical properties of 26 L-handed, 26 achiral, and 26 D-handed single NPs. Their single NP scattering spectra in the visible (VIS) and near-infrared (NIR) ( $\lambda = 500 - 1025 \text{ nm}$ ) are shown in Figure 4.4 for illumination with LCP (solid) and RCP (dashed) light. The spectra in each waterfall plot are shifted vertically by 1 (the color code we used to plot the spectra for the individual particles remains the same throughout the manuscript). This presentation of all the  $3 \times 26$  single nanoparticles in such a waterfall plot is essential as it allows for a quantitative and clear comparison of their scattering spectra and helps to find spectral differences.

First, we investigate the response of the achiral structures, depicted in the middle column. The strongest scattering for the particles, similarly to the chiral ones, appears between 700 and 900 nm, explaining the reddish appearance of the particles in the dark field microscope. We see that the scattering spectra for RCP and LCP illumination can hardly be distinguished for all of the particles. This finding is important for two reasons: Firstly, it demonstrates that the nanoparticle synthesis indeed delivers achiral particles of very high quality. Secondly, it confirms the validity of our measurement procedure as the achiral particles indeed should not show any chiroptical response. In previous works it has been shown that minute deviations from the ideal achiral shape indeed already cause significant chiroptical activity, which makes it challenging if not impossible to perform this control experiment with, e.g., top-down fabricated structures [108]. Therefore, the excellent optical achirality is testimony to the synthesis strategy used.

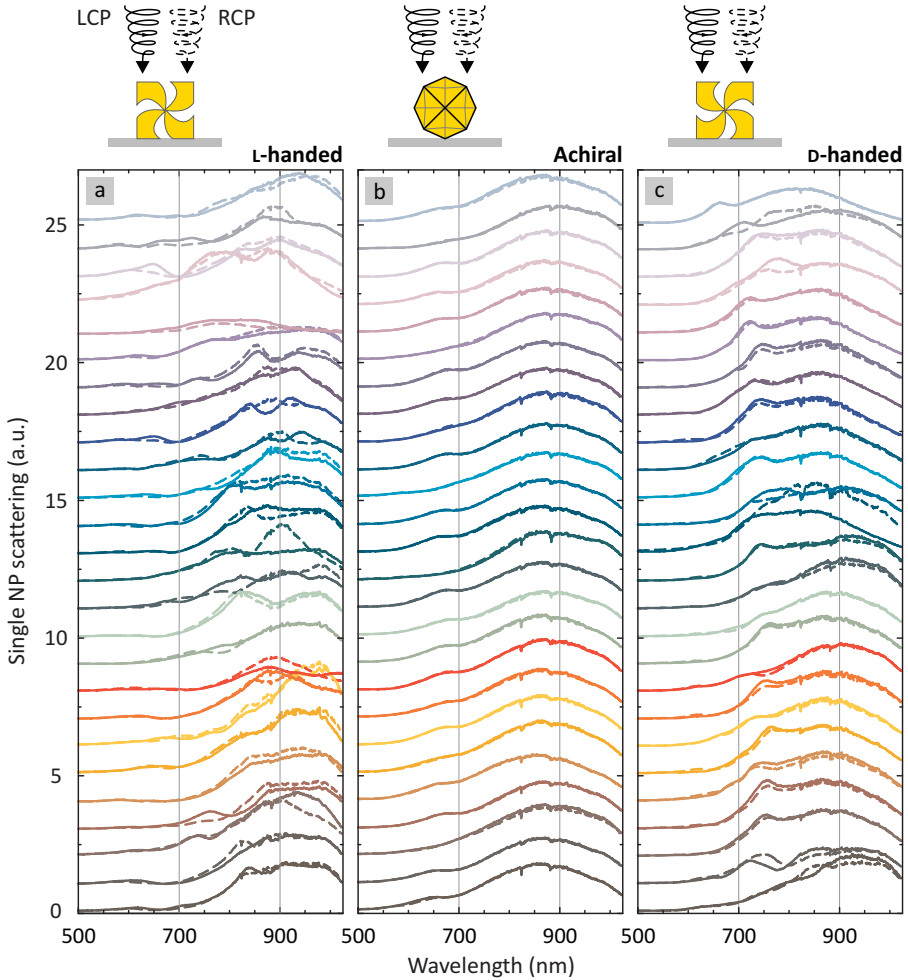


FIGURE 4.4. **Single helicoid chiral scattering spectra.** Scattering spectra of  $3 \times 26$  randomly picked single NPs (26 L-handed, 26 achiral, 26 D-handed) for LCP (solid) and RCP light illumination (dashed). The L-handed NPs are shown in (a), achiral NPs in (b), and D-handed NPs in (c). The offset between the spectra is 1. The L-handed and D-handed NPs show a large spread in the resonance position as well as in their spectral features, especially when compared to the achiral NPs. The cause of this observation lies within the structural differences in between the L-handed and D-handed single NPs.

The left column (Figure 4.4a) depicts the scattering spectra of the 26 L-handed single NPs. Already at first sight the scattering for RCP and LCP illumination can be clearly distinguished for all particles, pointing to a strong chiroptical response. The exact spectral shapes and signature, however, show a surprisingly large spread. Some of the NPs show only a single peak, some possess two distinct features whereas others show significantly reduced scattering. A similar behavior is observed for the D-handed single NP scattering spectra in Figure 4.4c, however the spread in optical features seems to be less in comparison to the L-handed enantiomers. Almost all D-handed NPs show a narrow peak around  $\lambda = 700 - 750 \text{ nm}$ . Overall, their scattering spectra are shifted slightly towards smaller wavelengths. The origin lies most probably within the slightly smaller dimensions of the D-handed NPs as we have observed in the SEM images shown in Figure 4.3. Comparing the scattering response of the L-handed and D-handed NPs, the chiroptical response of the L-handed ones seems to be larger on average, with also larger spectral spread. The D-handed NPs appear more uniform in their response.

Next, we want to study the chiroptical properties of the NPs in detail. In molecular systems this chiroptical response is generally given as differential absorbance for RCP and LCP incident light, called circular dichroism. This does, however, not imply that the chiroptical response of any system is defined via absorbances. The reason for the definition lies with the properties of molecular systems which predominantly absorb light and show very little to no scattering of light (as absorbance scales with  $V$ , while scattering scales with  $V^2$  and the molecular volume  $V$  is very small). This is in stark contrast to plasmonic systems. Here, due to its larger size compared to molecules, the light scattering cross sections can even significantly surpass the absorption cross sections. Consequently, it has been demonstrated that the structural chirality of a plasmonic systems manifests itself in the absorption and scattering response. These two contributions can in fact hold different information, as spectral far-field scattering maxima do not necessarily coincide with the maximum in absorption, in particular in systems with pronounced interaction via resonant light scattering. In Figure 4.5 we thus plot the differential scattering defined as  $\Delta S = S_{\text{RCP}} - S_{\text{LCP}}$ .

The differential scattering spectra obtained from the scattering spectra shown in Figure 4.4 are depicted as solid lines in Figure 4.5. Please note that our structures are intrinsically highly  $C_4$  symmetric and thus no correction for linear artifacts, such as linear birefringence, is necessary. The differential scattering reveals that the chiroptical response is significantly more pronounced than the spectra of Figure 4.4. Thus, it becomes even more important for the differential scattering to be able to quantitatively compare the individual responses and the spectral chiral signature of all  $3 \times 26$  single

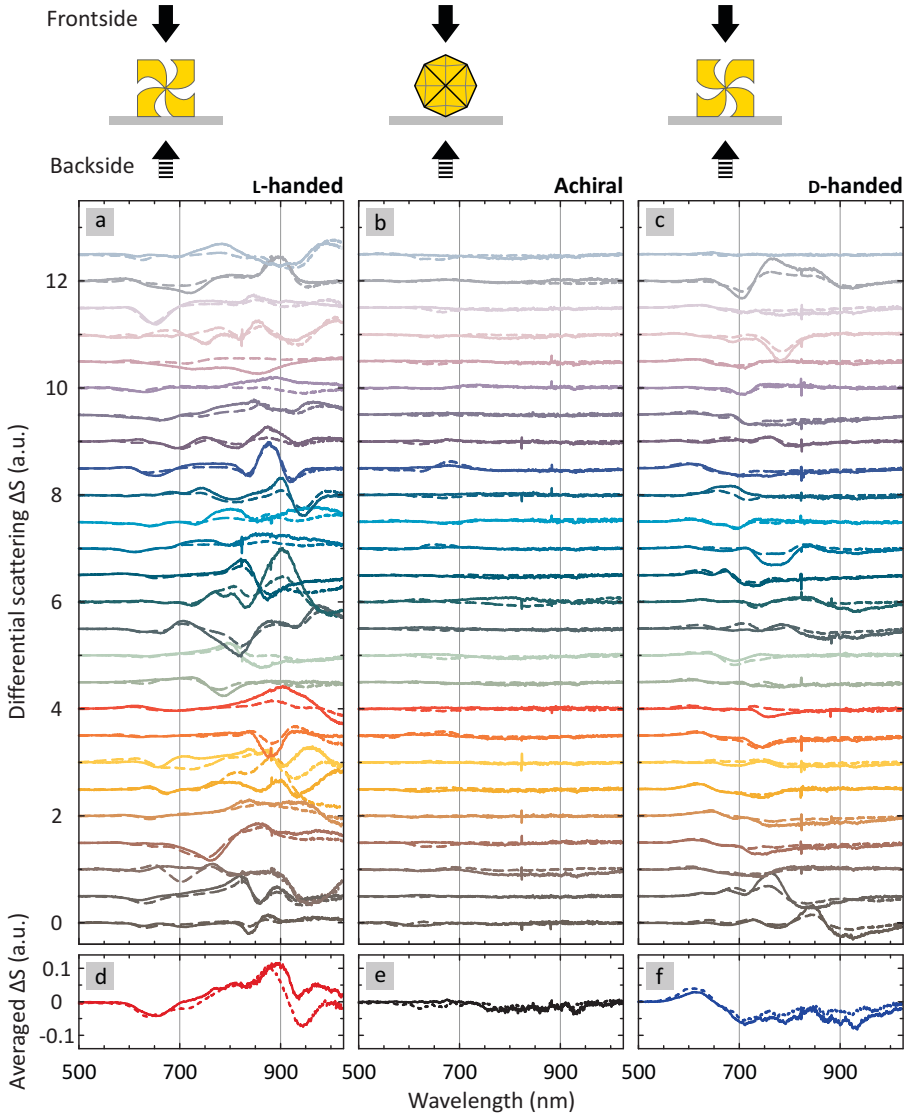


FIGURE 4.5. **Single helicoid differential scattering spectra.** Differential scattering spectra  $\Delta S = S_{\text{RCP}} - S_{\text{LCP}}$  of  $3 \times 26$  single NPs (26 L-handed, 26 achiral, 26 D-handed) in forward (solid) and backward illumination directions (dashed), respectively. The L-handed (a) and D-handed (c) NPs show a large spread in the differential scattering spectra caused by structural differences. In contrast, almost all achiral NPs show barely any chiroptical response. (d-f) Average of the differential scattering spectra of the single NPs shown (a-c), respectively. The average achiral chiroptical response is, as expected, clearly distinguishable from the chiroptical response of the enantiomers.

nanoparticles. This is again achieved (similar to Figure 4.4) by making use of the shown waterfall plot. Firstly, we turn our attention to the reference achiral NPs: We observe a close to zero chiroptical response for all 26 particles. As already mentioned, this is important as a control experiment to make sure the optical detection path performs flawlessly while also revealing the excellent NP quality. As we used the same scale on all panels, it is obvious that the small observed spectral features for the achiral structures are most likely measurement artifacts, but in any case, fully negligible when compared to the response of the chiral NPs. The results of another important control experiment are depicted as the dashed lines: Due to the encapsulation and immobilization of the nanoparticles we can flip the sample and thus revert the illumination direction. The handedness of a chiral particle is a geometric property and thus independent of the illumination direction. However, in general a sufficiently large chiral nanoparticle will not have exactly the same spectral response for all possible illumination directions due to retardation effects. This behavior is most obvious for an elongated spiral illuminated along the long axis or perpendicular to it, beautifully investigated in detail by Sachs et al. [231]. However, for exactly counterpropagating light fields the response needs to be close to identical. The reason for this control experiment is simple: Only in case of a true chiral response the differential scattering spectra will show reasonable agreement. Contributions of, for instance, polarization conversion or elliptical birefringence in contrast will flip sign. When inspecting the differential scattering spectra for forward and backward illumination for the achiral NPs, we see that also these spectra show little to no signal, again underlining the achirality of the NPs. The optical response of one particularly interesting particle is depicted in dark green (13th particle from the bottom): We observe a comparably strong differential scattering signal, however, it nearly perfectly flips sign for opposite illumination directions. This indicates that the observed signal in fact most probably originates from linear birefringence. For reasons unclear, locally the symmetry seems to be reduced, causing linear birefringence, which can be mistaken for a chiroptical signal without proper control experiments.

We now turn words to the chiroptical response of the L-handed NPs depicted in the left panel of Figure 4.5. Again, the differential scattering for forward and backward illumination is plotted as solid and dashed lines, respectively. Most of the chiroptical features are present in the wavelength range from  $\lambda = 750$  nm to  $\lambda = 950$  nm. In addition, some of the L-handed NPs show features at shorter wavelengths around  $\lambda = 600$  nm – 650 nm. Compared to the scattering spectra, the differential scattering very prominently indicates a surprisingly large spectral spread of the particles. We observe spectral signatures of varying number of modes and at different spectral

positions. The relative strength of these modes as well as their absolute values vary significantly. Some signatures, such as the one around 900 nm, are extremely pronounced in some spectra while being nearly absent in others. A subset of particles exhibits spectral signatures below 700 nm, which are not at all detectable for others. In general, the spectral spread is much larger than we would have naively expected from the SEM images as well as from the maturity of the synthesis strategy. This in fact points at two important implications: First, also in these particles seemingly minor structural deviations lead to significant spectral changes, which is in fact a very desirable property of interest. Moreover, it underpins that there is significant potential for improvement of the overall chiroptical response of the ensemble. The spectra measured for opposite illumination directions in general show excellent agreement with their counterparts. There are minor differences, which we ascribe to inaccuracies in alignment (single NP measurements are highly sensitive to possible small positioning differences) and smaller retardation effects. However, the overall spectral features and their relative strength are in excellent agreement, underlying that we are indeed measuring the true chiroptical response.

The right panel of Figure 4.5 finally depicts the differential scattering for the *D*-handed NPs for forward and backward illumination. The overall observations are very similar as in case of the *L*-handed NPs. The spectra for forward and backward illumination show reasonable agreement, validating our measurements. In general, the chiroptical response is smaller as well as blue-shifted in comparison to the *L*-handed NPs. Also, we observe smaller overall spread of the spectral response in terms of number of modal signatures and overall amplitudes. We ascribe this observation as well as the blue-shift to the slightly smaller size of the *D*-handed NPs which causes an overall blueshift as well as a less pronounced mode splitting. Additionally, we calculate the average of the single NP differential scattering spectra and plot them in Figure 4.5d-f, respectively. As expected from the individual spectra, the average of the achiral NPs is close to zero over the entire spectral range and is clearly distinguishable from the *L*- and *D*-handed response. They both show in parts, especially for  $\lambda < 700$  nm, mirror symmetry in the differential scattering. Again, we find a good agreement between the averages for the NPs being measured in forward (solid) and backward direction (dashed).

### 4.3.3 *Single vs. Ensemble*

As mentioned above, the full chiral answer of a plasmonic structure constitutes scattering and absorption contributions. As we are analyzing the scattering part in this work,



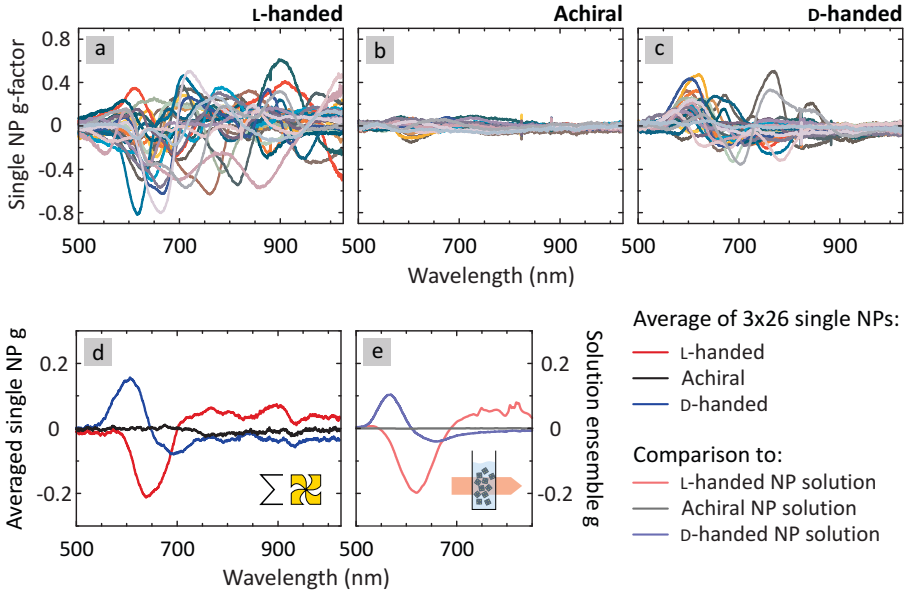


FIGURE 4.6. **Detailed g-Factor analysis of helicoid chiral nanoparticles as single vs. in an ensemble.** (a-c)  $g$ -factor spectra for all  $3 \times 26$  single NPs (26 L-handed, 26 achiral, 26 D-handed). The calculation of the  $g$ -factor allows for a comparison of the optical activity to solution (ensemble) measurements. In panel (d), we plot the averaged  $g$ -factor of the 26 L-handed (red), 26 achiral (black), and 26 D-handed NPs. Additionally, the  $g$ -factor of the respective NP solution is plotted in lighter colors in (e). The agreement between averaged single NPs and NP solution in terms of resonance position and absolute values of the  $g$ -factor is very good. We obtain similar maximum  $g$ -factor values of approximately  $\pm 0.2$ .

a direct comparison of the chiroptical response measured here to the absorptive CD measurements of the NPs in solution presented before requires proper normalization. The asymmetry  $g$ -factor represents a convenient normalized quantity facilitating this comparison. We define the transmission  $g$ -factor as

$$g_T = 2 \frac{S_{LCP} - S_{RCP}}{S_{LCP} + S_{RCP}}, \quad (4.66)$$

and the scattering  $g$ -factor as

$$g_S = 2 \frac{S_{RCP} - S_{LCP}}{S_{RCP} + S_{LCP}}, \quad (4.67)$$

meaning that we interchange the RCP and LCP contributions. This is simply an inversion of sign, and we link this definition to the contribution of absorption and scattering to the extinction cross section

$$\sigma_{\text{ext}} = \sigma_{\text{abs}} + \sigma_{\text{scat}}. \quad (4.68)$$

In Figure 4.6 we plot the asymmetry factor for all  $3 \times 26$  single NPs in panels a to c. We deliberately plotted each set of 26 measurements in one panel to once more demonstrate the diverse nature of the spectra. Examining the spectra for the L-handed and D-handed NPs, there seems to be no common pattern, but more a random distribution of modes at different spectral positions. The asymmetry factors for the achiral NPs show very little response when compared to the handed particles, in accordance with the previous discussion. Strikingly, when performing an averaging[108] by individually averaging the sets of  $3 \times 26$  measurements of Figure 4.6a-c, we observe a clear and pronounced chiral feature in the spectra, as shown in panel d of Figure 4.6. The averages of the L-handed and D-handed NPs show a remarkably strong dispersive chiral feature with good mirror symmetry (apart from the previously discussed slight spectral blue-shift of the D-handed NPs). The achiral average exhibits barely any features at all, as expected. Even more remarkable, the spectra show excellent agreement with the solution measurements of the same particles obtained with a Jasco CD spectrometer in transmission, as plotted in Figure 4.6e (note that this measurement can only be performed up to 775 nm). Despite a small spectral red-shift of the average due to a refractive index increase (from water  $n=1.33$  to spin-on-glass  $n = 1.41$ ), we obtain almost identical spectral shapes as well as absolute asymmetry values (note the identical y-scale). Fundamentally speaking, it is remarkable that the  $g$ -factor spectra obtained from these two different types of measurements (scattering vs. absorption) as well as from these completely different nanoparticle arrangements (average of single particles vs. solution ensemble) are almost identical [232].

This finding is important for a number of reasons: The individual measurements contain clearly significantly more details and information when compared to the average [108, 233–236]. In fact, it is stunning how many modal signatures vanish in the average while only a single dispersive feature remains. This immediately leads to an important question: Is this feature a consequence of a common chiral motif among all particles or is this the signature of a certain subset of particles which survives the averaging while the other signatures and particles cancel each other out? This question cannot be answered at this point, however, is highly relevant for future applications. If the signature is indeed related to a certain subset of particles, these particles could be identified, and purification strategies developed which would immediately increase the overall asymmetry. This point is underlined by another important finding of

the single particle measurements: The asymmetry of a few single NPs significantly outperforms the maximum  $g$ -factor values of the averaged NPs as well as of the solution, which is on the order of  $g \approx \pm 0.2$ . We find L-handed single particles with values of up to  $g = -0.8$ , which is four times larger than the average.

#### 4.3.4 *Correlation with Morphology*

The measurements and results above can only be explained by deviations in shape, size, dimensions, relative features, etc. between the individual particles. In particular, random uncontrolled deviations would most likely rather cancel out in an ensemble than being detectable. It is therefore highly compelling to try and analyze the morphology of the individual particles we measured optically and determine which particle is the “best”, hence resulting in the largest asymmetry factor. Such an analysis is in fact not straightforward. Firstly, even if the particles would be freely accessible, a determination of their three-dimensional morphology would only be possible by advanced transmission electron microscopy techniques. Additionally, the investigation is hindered by the fact that the particles are fully incorporated into the spin-on glass layer. In order to at least partially overcome this issue, we used a focused ion beam tool equipped with a laser interferometer stage (Raith ionLine Plus) to determine the exact coordinates of the particles and to selectively thin/mill the polymer over-coating. In detail, when we measured the chiroptical response of the  $3 \times 26$  single NPs, we saved the  $x$ - $y$ -coordinates of each particle relative to a chosen fix point. Afterwards, this allowed us to mark each particle in a separately taken overview dark-field image of the sample. Subsequently, this image was used to locate all particles with the Raith ionLine Plus system equipped with a laser interferometer stage and mill down the spin-on glass layer over an area of  $1 \times 1 \mu\text{m}^2$  at each particle position. Selected SEM images of these particles are shown in Figure 4.7 for six single L-handed in panel a and for six D-handed single NPs in panel b. The color code for each particle matches the color used in all previous figures. Please note that we milled as much of the spin-on glass as possible without destroying or damaging the particles. However, there are still parts of the layer left on top of as well as around the particles which causes the shown SEM images to exhibit a certain “blurriness” due to additional electron scattering in this layer.

The most prominent finding is that we in fact measured a number of L-handed pairs of particles instead of single ones. Spin coating of particles can lead to certain unavoidable clustering. This finding is also testimony to our unbiased selection of measurement spots. The spectral response of the particle pairs is, in fact, highly interesting.

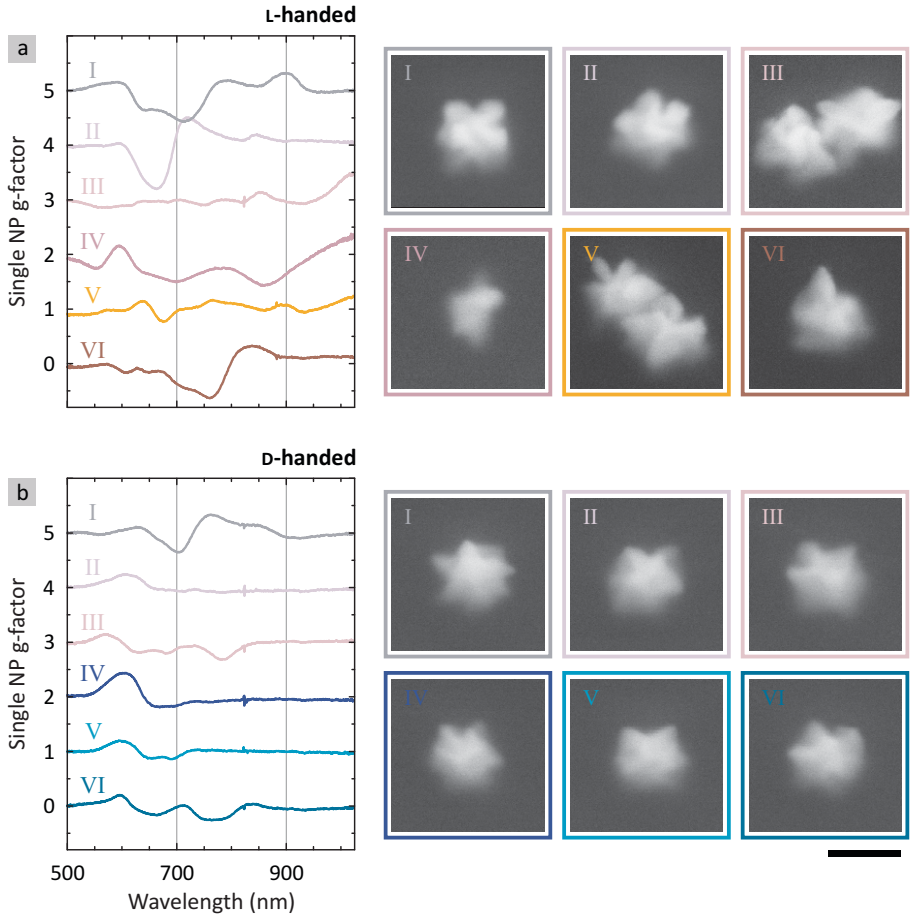


FIGURE 4.7. **Correlation between chiroptical response and morphology.** Single NP  $g$ -factor as well as the corresponding SEM images of six selected (a) L-handed and (b) D-handed NPs (labeled with I-VI). Note that the NPs are completely embedded in a spin-on glass layer, hence the SEM images are blurrier than the images in Figure 4.3. We see that the distinct differences in the  $g$ -factor spectra are caused by huge differences in the shape as well as in the dimensions of the NPs. Interestingly, some chiroptical responses correspond to dumbbell-shaped pairs of L-handed NPs, which was not observable in the initial dark-field scattering measurements. The scale bar is 200 nm.

Pair III depicted in pink shows barely any chiroptical response when compared to the other particles. This is a first hint that certain spectral signatures of different particles might indeed cancel out (particle pair V in orange shows similar behavior). Particles I and II possess the highest asymmetry factor of  $g = 0.5$  and  $g = 0.8$ . Interestingly, the main chiroptical features are in the same spectral region ( $\lambda = 600 - 750$  nm) as the mono-dispersive average response in Figure 4.6d (red curve). Previously reported simulation data of the helicoid nanoparticles showed a strong correlation between the chiroptical response and the helicoid NP geometrical parameters such as the gap depth, width, particle size and tilt angle, while resulting in a maximum asymmetry factor of around  $g \approx 0.8$  for the given pinwheel-like chiral nanostructures [228]. Due to the spin-on glass layer as well as the inability to observe all 6 facets of the particles it is difficult to access the precise shape of the particle. However, the best visible top facet ([100] view) closely resembles the ideal pinwheel-like structure, as shown in Figure 4.3. Further detailed investigation with appropriate statistics is needed, but this finding provides two valuable insights. First, it might again point to a potential subset of particles which is in fact responsible for the persistent chiral spectral motif visible in Figure 4.6d and e. Secondly, the observed significantly larger single NP asymmetry factor compared to the ensemble value suggests that there is potential to further improve the already impressive chiroptical properties of the NPs grown via the amino-acid and peptide directed synthesis approach. In contrast, particles IV and VI are clearly deformed. Despite limited visibility, particle IV shows an underdevelopment of chiral arms and cavities, causing it to be smaller in size. Particle VI is an example for a particle with overdeveloped chiral arms, similar to the last L-handed particle in Figure 4.3 (right). Significant extrusion and overgrowth of one of the chiral arms coincides also with a smaller core body. For both particles IV and VI, it is not straightforward to identify the chiral shape, still it is clearly presented as indicated by their chiroptical response which is in fact surprisingly large. Their chiral response, however, clearly differs from the average response of the L-handed NPs in Figure 4.6d.

In panel b of Figure 4.7 we show similar results for six D-handed single NPs. The SEM images underline the point made above: From the images it is very difficult to access the true and full morphology. The six particles appear significantly more uniform than the six L-handed NPs in panel a. Yet, there is still a significant spread in the spectral features which we cannot correlate with any particular structural differences. Particles II-VI appear to be more similar to the ideal D-handed shape with anticlockwise rotation of chiral arms as shown in Figure 4.3, whereas the shape of particle I seems ill-formed. However, clear assignments require significantly more statistics and merit further in-depth study.

### 4.3.5 Evolution of Chirality

Lastly, we investigate the evolution of the chirality of our helicoid single NPs. By adjusting the ratio between the gold precursor and peptide ratio, we can control the size of the helicoid nanoparticles and analyze the evolution of structural and optical chirality upon particle growth [237]. This is depicted in Figure 4.8 for the L-handed enantiomers. Panels a-c show SEM images of the differently sized helicoid nanoparticles. We clearly observe an evolution of the morphological chirality. While we observe for the 100 nm helicoids in Figure 4.8a no clear and well-pronounced typical pin-wheel like morphology, this structural chiral motif evolves and becomes more pronounced for the larger 125 nm helicoids in panel b. By increasing the gold precursor proportion even further, we obtain the large 150 nm helicoid NPs in panel c with the well pronounced pin-wheel like morphology, as known from our study in the previous sections.

As we have discussed, due to strong morphological differences between individual NPs, a chiroptical study on the single particle level requires a large quantity of measured and analyzed NPs. As our chiral scatterometry method works fully automated we are able to measure and investigate these required large amounts of single helicoids for all three particle sizes shown in Figure 4.8. Panels d-f depict scanned images of three samples containing the three helicoid NPs with different sizes. We plot the largest differential scattering signal (positive or negative) of each measured pixel over a measured area of  $100 \times 100 \mu\text{m}^2$ . The automatically detected and analyzed particles (from average scattering images, see Figure 4.2b) are marked with black crosses. Please note that due to different adhesion of the particles during spin-coating on the glass substrates the interparticle distance can vary. Consequently, the sampling area of  $100 \times 100 \mu\text{m}^2$  contains a different amount of helicoid NPs for the three investigated samples/sizes. While Figure 4.8d contains 87 helicoid NPs, panels e and f contain 163 and 46 single helicoid NPs, respectively.

Additionally, the differential scattering images underline a very important property of our setup. We find (within experimental realization and limits) background-free chiroptical images. This means that areas where no (or achiral) particles are placed, we observe no differential scattering signal, a white background on the chosen color map. It proves that there is no background chiroptical signal in all our measurements present. In case of badly aligned setups, such a chiroptical background signal could arise from misaligned optical components in the illumination or detection path of the microscope.

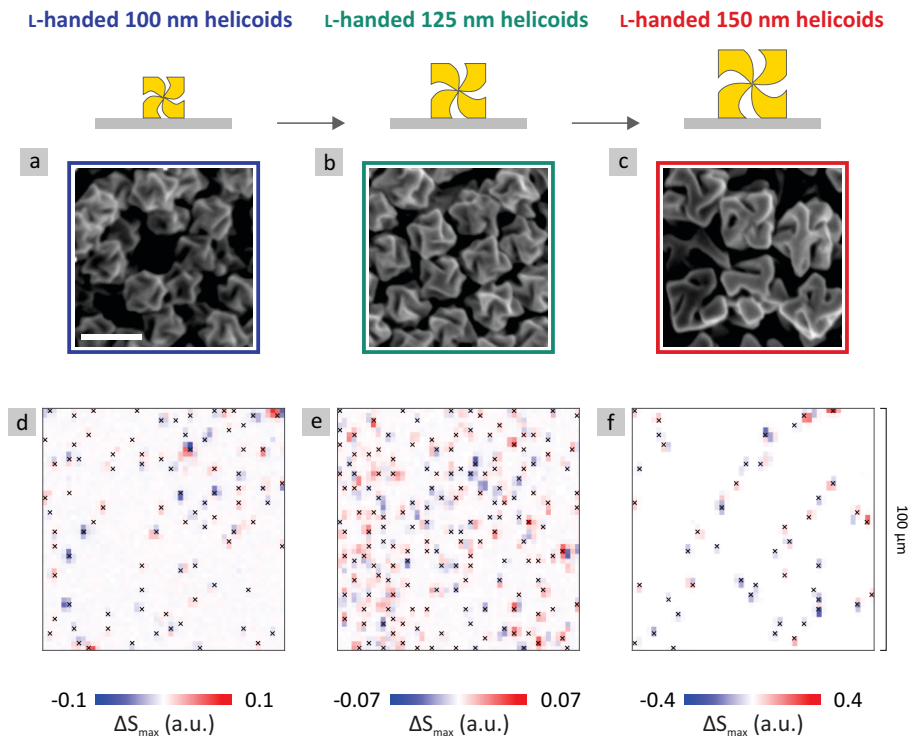


**FIGURE 4.8. Evolution of single particle chirality for differently sized helicoids - particle mapping** (a-c) SEM images of NP ensembles showing the evolution of chirality in the of L-handed helicoids. We can control the size of the helicoids via the gold precursor vs. peptide ratio to obtain different sizes of 100 nm (left panels), 125 nm (middle panels), and 150 nm (right panels). The scale bar is 200 nm and is valid for all three SEM images. (d-f) Maximum differential scattering map of an automatically scanned  $100 \times 100 \mu\text{m}^2$  area of samples containing the differently sized single helicoid NPs.

The panels a-c in Figure 4.9 depict the single NP  $g$ -factor spectra for all analyzed single helicoids with sizes of 100 nm, 125 nm, and 150 nm, respectively. The corresponding averaged single NP  $g$ -factor spectra are shown in panel d in blue, green, and red, respectively. We find that an increased size results in a red shift of the main chiral motif from 550 nm to 650 nm as well as in an increase of the absolute  $g$ -factor and thus the optical chirality of the NPs. The reason lies with the evolution of the chiral pin-wheel like morphology for larger helicoids. Additionally, at first, there seems to be a random distribution of spectral modes all over the visible spectral range with no common and dominant spectral feature. However, comparing the individual spectra to the averaged  $g$ -factor spectra in Figure 4.9d, it becomes apparent that the main chiral motifs in the range between 550 nm and 650 nm are clearly visible also in the individual spectra. Depending on the number of averaged single helicoids, the main feature becomes more and more pronounced and observable in the overlaid single particle spectra (in Figure 4.9a-c). For the large 150 nm helicoid NPs, the main chiral motif (red curve panel d) appears at 650 nm. Although averaging only 46 individual spectra, this dominant feature can already be seen in the full set of spectra in Figure 4.9c, which was not possible for the 26 single particles in Figure 4.6a.

This raises a very important question: How many individual particles are actually needed in order to reproduce the optical response from a solution ensemble measurement? To study this question, we investigate the averaged chiroptical properties in dependence of the number of particles in Figure 4.9e. The influence is determined by averaging the chiroptical response of a certain # of NPs and comparing this average to the total average of all measured NPs. In detail, we take the average  $g$ -factor spectrum of a # of NPs and subtract the average  $g$ -factor spectrum of all 163 averaged NPs (green curve in Figure 4.9d). Finally, we calculate the mean value for all wavelengths. To remove a biased selection of averaged NPs, we plot in Figure 4.9e ten different random permutations of the NP selection. We find large differences to the total average up to approximately 20-25 averaged single helicoid NPs. For a larger # of NPs the curves start to flatten until, as expected, the difference becomes 0 for 163 averaged NPs. In conclusion, this means that a representative chiroptical response for our helicoid NPs can be obtained for clusters/ensembles comprising at least 30-40 single particles. Below this value the average spectrum might strongly differ from the anticipated chiroptical response.



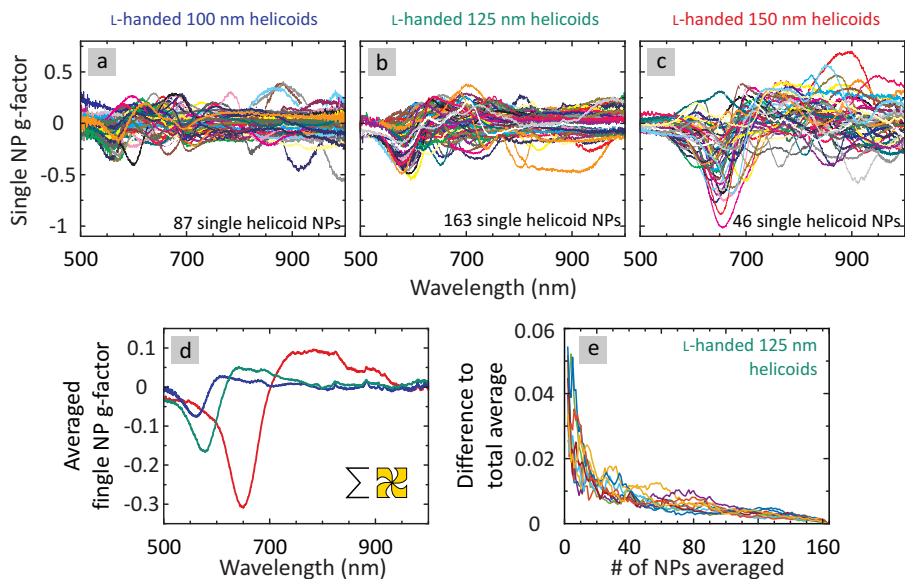


**FIGURE 4.9. Evolution of single particle chirality for differently sized helicoids - spectra** (a-c) Automatically measured  $g$ -factor spectra of 87, 163, and 46 single helicoid NPs with the different sizes of 100 nm, 125 nm, and 150 nm, respectively. (d) Average single NP  $g$ -factor of the spectra shown in (a-c). The different sizes of 100 nm, 125 nm, and 150 nm helicoids are depicted in blue, green, and red, respectively, showing the chiroptical response during the growth of the helicoid NPs. (e) Absolute  $g$ -factor difference (from total average of 163 NPs) versus the # of averaged NPs. The individual curves correspond to ten different random permutations of particle selection for averaging.

#### 4.4 CONCLUSIONS & OUTLOOK

In conclusion, we have carried out a quantitative and consistent comparison of the optical and chiroptical properties of chemically synthesized single plasmonic NPs. We used single particle chiral scatterometry in combination with scanning electron microscopy to investigate the influence of structural differences on the single particle chiroptical response. The differential scattering spectra of 26 left-handed and 26 right-handed helicoid NPs showed a huge spread in spectral positions of chiroptical features as well as in absolute values of the optical activity. Consistency was proven with an illumination of the NPs from front- and backside, where the chiroptical responses showed a very good agreement. The chiroptical response of additionally measured 26 achiral octahedral NPs was close to zero and clearly distinguishable from the chiroptical response of the two enantiomers. Focused ion beam milling allowed for a structural investigation of selected helicoid NPs and showed structural differences in terms of an over- and underdevelopment of chiral arms and cavities, which strongly influenced the single particle chiroptical response. A comparison of the averaged single NP scattering asymmetry factor to the asymmetry factor of the NPs ensemble in solution resulted in almost identical  $g$ -factor spectra. Among measured individual nanoparticles, the highest asymmetry factor was found to be  $g = 0.8$ , which is a 4-fold increase compared to the solution ensemble. Our findings clearly show there is significant potential to further increase the asymmetry of the helicoid NP ensemble solution by an appropriate refinement during synthesis or by post-fabrication purification. Consequently, the presented results have immediate implications in nanoparticle synthesis by using single particle chiral scatterometry as a feedback for the development and fabrication of high-quality chemical synthesis methods. In addition, our findings can help to develop refinement methods which ensure particles which do not only show little inhomogeneities in their structural properties but in particular in their optical response.

What is more, chiral plasmonic nanostructures have become of tremendous importance over the last decade. Several sophisticated fabrication techniques emerged, enabled by groundbreaking advances in nanofabrication. 3D chiral nanostructures with nearly arbitrary morphological and optical properties have been realized, as required for potential applications such as novel metadevices for augmented reality (AR), virtual reality (VR), optical holography, light detection and ranging (LiDAR), and others. Combinations with DNA or optically active materials even allowed to demonstrate active tuning of the chirality of plasmonic nanosystems. Further, there has been tremendous effort to investigate the contribution of the individual nanoparticle to

the chiroptical response of an ensemble of nanoparticles arranged on substrates or in solution. This research will be highly beneficial to further decrease sensing volumes in chiral sensing schemes as the detection of a single chiral molecule and its interaction with a single chiral plasmonic nanoparticle will be, in the future, of ultimately high interest. In combination with the proposed active plasmonic materials in this thesis, even ultra-sensitive actively controllable sensors could become reality.



## SYMBOLS

---

$\alpha$	absorption coefficient.
$g$	asymmetry factor.
$\omega$	angular frequency.
pKa	acid dissociation constant.
$n_{\rho}$	charge carrier density.
$\sigma$	conductivity.
$\rho$	charge.
$\mathbf{j}$	current density.
$\gamma$	damping constant.
$\Delta S$	differential scattering.
<b>D</b>	dielectric displacement.
$\epsilon$	dielectric function.
$\chi$	dielectric susceptibility.
$E$	electric field (amplitude).
$\kappa$	extinction coefficient.
<b>E</b>	electric field.
$I$	intensity.
<b>B</b>	magnetic flux density.
<b>H</b>	magnetic field.
<b>p</b>	momentum / dipole moment.
<b>M</b>	magnetization.
$m$	mass.
NA	numerical aperture.
$P_l(\cos \theta)$	legendre polynomials.
$\mu$	permeability (relative).
$\omega_p$	plasma frequency.

$\hat{\alpha}$	polarizability.
<b>P</b>	polarization.
$r$	reflection coefficient.
$\tau$	relaxation time.
$n$	refractive index.
$s$	scattering amplitude.
$\varphi$	scattering phase.
$S$	scattering.
$\lambda$	wavelength.
$\nu$	wavenumber.
<b>k</b>	wave vector.

## ACRONYMS

---

AFM	atomic force microscopy.
AR	augmented reality.
Ar	argon.
CD	circular dichroism.
DF	dark-field.
EBL	electron beam lithography.
FF	far-field.
FWHM	full width at half maximum.
H <sub>2</sub>	hydrogen.
hcp	hexagonally closed package.
IR	infrared.
ITO	indium-tin-oxide.
LCP	left-circularly polarized.
LiDAR	light detection and ranging.
Mg	magnesium.
MgH <sub>2</sub>	magnesium hydride.
MgO	magnesium oxide.
MIR	mid-infrared.
N <sub>2</sub>	nitrogen.
NF	near-field.
NIR	near-infrared.
NP	nanoparticle.
O <sub>2</sub>	oxygen.
ORD	optical rotatory dispersion.
Pd	palladium.

PEDOT:PSS	poly(3,4-ethylenedioxythiophene):polystyrene sulfonate.
PMMA	poly(methyl methacrylate).
QWP	quarter wave plate.
RCP	right-circularly polarized.
SEM	scanning electron microscopy.
SNOM	scanning nearfield optical microscopy.
sSNOM	scattering-type scanning nearfield optical microscopy.
TE	transverse electric.
TEM	transmission electron microscopy.
Ti	titanium.
TM	transverse magnetic.
VIS	visible.
VR	virtual reality.
Y	yttrium.
YH <sub>2</sub>	yttrium dihydride.



## LIST OF FIGURES

---

Figure 2.1	Theoretical dispersion in DRUDE model . . . . .	9
Figure 2.2	DRUDE model on experimental data. . . . .	11
Figure 2.3	Theoretical dispersion in LORENTZ model . . . . .	12
Figure 2.4	Excitation of localized surface plasmon in a metallic nanoparticle. . . . .	13
Figure 2.5	Sketch of a homogeneous sphere for LSPs. . . . .	14
Figure 2.6	Influence of dielectric function on resonance position of plasmonic nanoantennas. . . . .	16
Figure 2.7	Fabrication of plasmonic nanoantennas made from metallic polymer. . . . .	19
Figure 2.8	Concept of electrically switchable nanoantennas. . . . .	21
Figure 2.9	Dielectric function of poly(3,4-ethylenedioxythiophene):polystyrene sulfonate (PEDOT:PSS) upon electrical switching. . . . .	22
Figure 2.10	Optical tunability of plasmonic nanoantennas made from metallic polymers. . . . .	24
Figure 2.11	Simulation of pristine plasmonic nanoantennas from metallic polymer. . . . .	25
Figure 2.12	Electrochemical switching setup. . . . .	26
Figure 2.13	Electrical switching of plasmonic resonance. . . . .	27
Figure 2.14	Entire spectral data of electrically switchable plasmonic nanoantennas made from metallic polymers. . . . .	28
Figure 2.15	Electrical switching with 1 Hz frequency. . . . .	29
Figure 2.16	Extraction of switching time. . . . .	30
Figure 2.17	Electrical switching with video-rate frequency. . . . .	31
Figure 2.18	Concept of metallic polymer plasmonic metasurface for high-efficiency active beam steering. . . . .	32
Figure 2.19	Spectra and SEM image of the metallic polymer beam steering metasurface. . . . .	33
Figure 2.20	Pristine beam diffraction with polymer metasurface. . . . .	34
Figure 2.21	High contrast beam steering with metallic polymer metasurface. . . . .	35
Figure 2.22	Continuous active beam steering with metallic polymer metasurface. . . . .	37
Figure 2.23	Schematics of electro-active metaobjective from metalenses-on-demand. . . . .	39

Figure 2.24	Concept of electro-active metaobjective from metalenses-on-demand. . . . .	40
Figure 2.25	Metalens phase profile. . . . .	41
Figure 2.26	SEM image and plasmonic resonance of metallic polymer metalens. . . . .	42
Figure 2.27	Mapping refractive power of polymer metalens. . . . .	43
Figure 2.28	High-contrast electrical switching of a metallic polymer metalens-on-demand. . . . .	44
Figure 2.29	Continuous electrical switching of refractive power of metalens. . . . .	45
Figure 2.30	Non-volatile operation of metallic polymer metalens. . . . .	46
Figure 2.31	Schematic setup to switch the individual metalenses of the metaobjective. . . . .	47
Figure 2.32	Non-volatile electrically switchable multi-functional metaobjective. . . . .	48
Figure 3.1	Principle of scattering-type scanning nearfield optical microscopy (sSNOM) . . . . .	54
Figure 3.2	Sketches of the sSNOM configuration for different theoretical models. . . . .	55
Figure 3.3	Sketches for perfectly conducting spheroid. . . . .	56
Figure 3.4	Pseudoheterodyne detection for an sSNOM experiment. . . . .	60
Figure 3.5	Real and imaginary part of the dielectric function of magnesium (Mg). . . . .	62
Figure 3.6	Real and imaginary part of the dielectric function of magnesium hydride (MgH <sub>2</sub> ). . . . .	63
Figure 3.7	infrared (IR) spectrum of laser-ablated MgH <sub>2</sub> . . . . .	64
Figure 3.8	In-situ sSNOM principle. . . . .	68
Figure 3.9	Near-field appearance of the Mg-MgH <sub>2</sub> phase transition. . . . .	71
Figure 3.10	Near-field spectral response of Mg and MgH <sub>2</sub> . . . . .	73
Figure 3.11	Comparison of near-field (NF) contrast between measurement and calculation. . . . .	75
Figure 3.12	Measured and calculated reflectance spectra of Mg and MgH <sub>2</sub> thin films. . . . .	76
Figure 3.13	Watching nanoscale hydrogen diffusion in Mg. . . . .	78
Figure 3.14	Schematic drawing of the vertical MgH <sub>2</sub> formation in a 50 nm Mg film. . . . .	79
Figure 3.15	Dynamics of the hydride phase propagation in individual grains vs. the entire film. . . . .	81
Figure 3.16	Topography evolution of Mg during hydrogen loading. . . . .	83

Figure 3.17	Vertical expansion of Mg during hydrogen loading. . . . .	84
Figure 3.18	Change of topography during hydrogenation. . . . .	87
Figure 3.19	Average vertical expansion of Mg thin film vs. hydrogen loading time. . . . .	88
Figure 3.20	Concept of liquid hydrogenation. . . . .	91
Figure 3.21	Material investigation via thin films - proof of concept. . . . .	93
Figure 3.22	palladium (Pd) cap layer state after ethanol exposure. . . . .	94
Figure 3.23	Liquid hydrogenation of yttrium (Y) thin films with different alcohols. . . . .	95
Figure 3.24	In-situ temporal investigation of liquid hydrogenation of Y thin films. . . . .	97
Figure 3.25	Nanooptical indicator for deprotonation process - hydrogenation of plasmonic nanoantennas. . . . .	98
Figure 3.26	Plasmonic resonance tuning via ethanol, gasochromic comparison, and simulation of yttrium dihydride (YH <sub>2</sub> ) nanoantennas. . . . .	101
Figure 4.1	Automized single particle chiral scatterometry . . . . .	108
Figure 4.2	Measurement procedure for automized chiral scatterometry . . . . .	109
Figure 4.3	Single helicoid chiral nanoparticles . . . . .	112
Figure 4.4	Single helicoid chiral scattering spectra . . . . .	114
Figure 4.5	Single helicoid differential scattering spectra . . . . .	116
Figure 4.6	Detailed g-Factor analysis of helicoid chiral nanoparticles as single vs. in an ensemble. . . . .	119
Figure 4.7	Correlation between chiroptical response and morphology . . . . .	122
Figure 4.8	Evolution of single particle chirality for differently sized helicoids - particle mapping . . . . .	125
Figure 4.9	Evolution of single particle chirality for differently sized helicoids - spectra . . . . .	127



## BIBLIOGRAPHY

---

- [1] I. Kim et al., *Nanophotonics for light detection and ranging technology*, *Nature Nanotechnology* **16**, 508–524 (2021).
- [2] A. H. Dorrah, N. A. Rubin, A. Zaidi, M. Tamagnone, and F. Capasso, *Metasurface optics for on-demand polarization transformations along the optical path*, *Nature Photonics* **15**, 287–296 (2021).
- [3] G.-Y. Lee et al., *Metasurface eyepiece for augmented reality*, *Nature Communications* **9**, 4562 (2018).
- [4] J. Park et al., *All-solid-state spatial light modulator with independent phase and amplitude control for three-dimensional LiDAR applications*, *Nature Nanotechnology* **16**, 69–76 (2021).
- [5] W.-J. Joo et al., *Metasurface-driven OLED displays beyond 10,000 pixels per inch*, *Science* **370**, 459–463 (2020).
- [6] N. Yu et al., *Light Propagation with Phase Reflection and Refraction*, *Science* **334**, 333–337 (2011).
- [7] L. Huang et al., *Dispersionless phase discontinuities for controlling light propagation*, *Nano Letters* **12**, 5750–5755 (2012).
- [8] S. Sun et al., *Gradient-index meta-surfaces as a bridge linking propagating waves and surface waves*, *Nature Materials* **11**, 426–431 (2012).
- [9] A. V. Kildishev, A. Boltasseva, and V. M. Shalaev, *Planar Photonics with Metasurfaces*, *Science* **339**, 1232009 (2013).
- [10] J. Karst et al., *Electrically switchable metallic polymer nanoantennas*, *Science* **374**, 612–616 (2021).
- [11] P. C. Wu et al., *Dynamic beam steering with all-dielectric electro-optic III-V multiple-quantum-well metasurfaces*, *Nature Communications* **10**, 1–9 (2019).
- [12] J. Ratzsch et al., *Electrically switchable metasurface for beam steering using PEDOT polymers*, *Journal of Optics* **22**, 124001 (2020).

- [13] X. Chen et al., *Dual-polarity plasmonic metalens for visible light*, Nature Communications **3**, 1–6 (2012).
- [14] M. Khorasaninejad et al., *Metalenses at visible wavelengths: Diffraction-limited focusing and subwavelength resolution imaging*, Science **352**, 1190–1194 (2016).
- [15] S. Wang et al., *A broadband achromatic metalens in the visible*, Nature Nanotechnology **13**, 227–232 (2018).
- [16] M. Y. Shalaginov et al., *Reconfigurable all-dielectric metalens with diffraction-limited performance*, Nature Communications **12**, 1–8 (2021).
- [17] X. Yin et al., *Beam switching and bifocal zoom lensing using active plasmonic metasurfaces*, Light: Science & Applications **6**, e17016 (2017).
- [18] T. Badloe, I. Kim, Y. Kim, J. Kim, and J. Rho, *Electrically Tunable Bifocal Metalens with Diffraction-Limited Focusing and Imaging at Visible Wavelengths*, Advanced Science **8**, 2102646 (2021).
- [19] M. Khorasaninejad and F. Capasso, *Metalenses: Versatile multifunctional photonic components*, Science **358**, (2017).
- [20] A. She, S. Zhang, S. Shian, D. R. Clarke, and F. Capasso, *Adaptive metalenses with simultaneous electrical control of focal length, astigmatism, and shift*, Science Advances **4**, 1–8 (2018).
- [21] M. Bosch et al., *Electrically Actuated Varifocal Lens Based on Liquid-Crystal-Embedded Dielectric Metasurfaces*, Nano Letters **21**, 3849–3856 (2021).
- [22] J. Kim et al., *Tunable metasurfaces towards versatile metalenses and metaholograms: a review*, Advanced Photonics **4**, 1 (2022).
- [23] R. Kaissner et al., *Electrochemically controlled metasurfaces with high-contrast switching at visible frequencies*, Science Advances **7**, eabd9450 (2021).
- [24] P. Yu et al., *Generation of Switchable Singular Beams with Dynamic Metasurfaces*, ACS Nano **13**, 7100–7106 (2019).
- [25] J. Li, P. Yu, S. Zhang, and N. Liu, *Electrically-controlled digital metasurface device for light projection displays*, Nature Communications **11**, 3574 (2020).

- [26] Z. Li et al., *Meta-optics achieves RGB-achromatic focusing for virtual reality*, *Science Advances* **7**, eabe4458 (2021).
- [27] J. Xiong, E. L. Hsiang, Z. He, T. Zhan, and S. T. Wu, *Augmented reality and virtual reality displays: emerging technologies and future perspectives*, *Light: Science and Applications* **10**, 1–30 (2021).
- [28] J. Li et al., *Addressable metasurfaces for dynamic holography and optical information encryption*, *Science Advances* **4**, eaar6768 (2018).
- [29] S. Q. Li et al., *Phase-only transmissive spatial light modulator based on tunable dielectric metasurface*, *Science* **364**, 1087–1090 (2019).
- [30] S. Mansha et al., *High resolution multispectral spatial light modulators based on tunable Fabry-Perot nanocavities*, *arXiv preprint*, arXiv:2109.13567 (2021).
- [31] A. Arbabi, Y. Horie, M. Bagheri, and A. Faraon, *Dielectric metasurfaces for complete control of phase and polarization with subwavelength spatial resolution and high transmission*, *Nature Nanotechnology* **10**, 937–943 (2015).
- [32] D. Lin, P. Fan, E. Hasman, and M. L. Brongersma, *Dielectric gradient metasurface optical elements*, *Science* **345**, 298–302 (2014).
- [33] I. Staude and J. Schilling, *Metamaterial-inspired silicon nanophotonics*, *Nature Photonics* **11**, 274–284 (2017).
- [34] X. Ni, N. K. Emani, A. V. Kildishev, A. Boltasseva, and V. M. Shalaev, *Broadband Light Bending with Plasmonic Nanoantennas*, *Science* **335**, 427–427 (2012).
- [35] M. Lawrence et al., *High quality factor phase gradient metasurfaces*, *Nature Nanotechnology* **15**, 956–961 (2020).
- [36] G. Zheng et al., *Metasurface holograms reaching 80% efficiency*, *Nature Nanotechnology* **10**, 308–312 (2015).
- [37] G. Yoon, D. Lee, K. T. Nam, and J. Rho, *Crypto-Display in Dual-Mode Metasurfaces by Simultaneous Control of Phase and Spectral Responses*, *ACS Nano* **12**, 6421–6428 (2018).
- [38] A. M. Shaltout, V. M. Shalaev, and M. L. Brongersma, *Spatiotemporal light control with active metasurfaces*, *Science* **364**, eaat3100 (2019).

- [39] N. Jiang, X. Zhuo, and J. Wang, *Active Plasmonics: Principles, Structures, and Applications*, *Chemical Reviews* **118**, 3054–3099 (2018).
- [40] M. Wuttig, H. Bhaskaran, and T. Taubner, *Phase-change materials for non-volatile photonic applications*, *Nature Photonics* **11**, 465–476 (2017).
- [41] S. Chen et al., *Conductive polymer nanoantennas for dynamic organic plasmonics*, *Nature Nanotechnology* **15**, 35–40 (2020).
- [42] X. Duan, S. Kamin, and N. Liu, *Dynamic plasmonic colour display*, *Nature Communications* **8**, 1–9 (2017).
- [43] Q. Wang et al., *Optically reconfigurable metasurfaces and photonic devices based on phase change materials*, *Nature Photonics* **10**, 60–65 (2016).
- [44] J. Karst, M. Hentschel, F. Sterl, and H. Giessen, *Liquid Hydrogenation of Plasmonic Nanoantennas via Alcohol Deprotonation*, *ACS Photonics* **8**, 1810–1816 (2021).
- [45] J. Karst et al., *Optimizing magnesium thin films for optical switching applications: rules and recipes*, *Optical Materials Express* **10**, 1346 (2020).
- [46] J. Karst et al., *Watching In-Situ the Hydrogen Diffusion Dynamics in Magnesium on the Nanoscale*, *Science Advances* **6**, eaaz0566 (2020).
- [47] F. Sterl et al., *Magnesium as novel material for active plasmonics in the visible wavelength range*, *Nano Letters* **15**, 7949–7955 (2015).
- [48] N. Strohhfeldt et al., *Yttrium hydride nanoantennas for active plasmonics*, *Nano Letters* **14**, 1140–1147 (2014).
- [49] Y. Wang et al., *Electrical tuning of phase-change antennas and metasurfaces*, *Nature Nanotechnology* **16**, 667–672 (2021).
- [50] Y. Zhang et al., *Electrically reconfigurable non-volatile metasurface using low-loss optical phase-change material*, *Nature Nanotechnology* **16**, 661–666 (2021).
- [51] G. K. Shirmanesh, R. Sokhoyan, P. C. Wu, and H. A. Atwater, *Electro-optically Tunable Multifunctional Metasurfaces*, *ACS Nano* **14**, 6912–6920 (2020).
- [52] T. Xu et al., *High-contrast and fast electrochromic switching enabled by plasmonics*, *Nature Communications* **7**, 1–6 (2016).



- [53] D. Franklin, R. Frank, S. T. Wu, and D. Chanda, *Actively addressed single pixel full-colour plasmonic display*, *Nature Communications* **8**, 1–10 (2017).
- [54] J. Peng et al., *Scalable electrochromic nanopixels using plasmonics*, *Science Advances* **5**, eaaw2205 (2019).
- [55] Y. Leroux et al., *Tunable electrochemical switch of the optical properties of metallic nanoparticles*, *ACS Nano* **2**, 728–732 (2008).
- [56] Y. Kim et al., *Phase Modulation with Electrically Tunable Vanadium Dioxide Phase-Change Metasurfaces*, *Nano Letters* **19**, 3961–3968 (2019).
- [57] J. Karst, *Circular Dichroism Spectroscopy on Individual Plasmonic Nanoparticles*, Bachelor Thesis, University of Stuttgart, 2015.
- [58] S. A. Maier, *Fundamentals and Applications Plasmonics : Fundamentals and Applications*, Springer US, 2007.
- [59] R. W. Boyd, *Nonlinear Optics*, Academic Press, 2008.
- [60] P. B. Johnson, R. W. Christy, and R. W. C. p. b. Johnson, *Optical Constants of the Noble Metals*, *Physical Review B* **6**, 10 (1972).
- [61] Drude, *Zur Elektronentheorie der Metalle*, *Annalen der Physik*, 49–52 (1900).
- [62] C. Bohren and D. Huffman, *Absorption and scattering of light by small particles*, Wiley-VCH, 2004.
- [63] T. J. Davis and D. E. Gómez, *Colloquium: An algebraic model of localized surface plasmons and their interactions*, *Reviews of Modern Physics* **89**, 1–20 (2017).
- [64] A. J. Heeger, *Semiconducting and Metallic Polymers: The Fourth Generation of Polymeric Materials*, *The Journal of Physical Chemistry B* **105**, 8475–8491 (2001).
- [65] M. Girtan, R. Mallet, M. Socol, and A. Stanculescu, *On the Physical Properties PEDOT:PSS Thin Films*, *Materials Today Communications* **22**, 100735 (2020).
- [66] D. Neusser et al., *High Conductivities of Disordered P3HT Films by an Electrochemical Doping Strategy*, *Chemistry of Materials* **32**, 6003–6013 (2020).
- [67] M. Wieland et al., *Conductance and spectroscopic mapping of EDOT polymer films upon electrochemical doping*, *Flexible and Printed Electronics* **5**, 014016 (2020).

- [68] A. Karki et al., *Electrical Tuning of Plasmonic Conducting Polymer Nanoantennas*, *Advanced Materials* **34**, 2107172 (2022).
- [69] Y. Lin et al., *Tunable electrochromic Au nanorod-based metalenses for visible light*, *Optics Express* **29**, 43011 (2021).
- [70] A. S. Solntsev, G. S. Agarwal, and Y. Y. Kivshar, *Metasurfaces for quantum photonics*, *Nature Photonics* **15**, 327–336 (2021).
- [71] K. Xiong et al., *Video Speed Switching of Plasmonic Structural Colors with High Contrast and Superior Lifetime*, *Advanced Materials* **33**, 2103217 (2021).
- [72] R. Griessen, N. Strohfeltdt, and H. Giessen, *Thermodynamics of the hybrid interaction of hydrogen with palladium nanoparticles*, *Nature Materials* **15**, 311–317 (2016).
- [73] A. Baldi, T. C. Narayan, A. L. Koh, and J. A. Dionne, *In situ detection of hydrogen-induced phase transitions in individual palladium nanocrystals*, *Nature Materials* **13**, 1143–1148 (2014).
- [74] T. C. Narayan et al., *Direct visualization of hydrogen absorption dynamics in individual palladium nanoparticles*, *Nature Communications* **8**, 1–8 (2017).
- [75] A. Yau, R. J. Harder, M. W. Kanan, and A. Ulvestad, *Imaging the Hydrogen Absorption Dynamics of Individual Grains in Polycrystalline Palladium Thin Films in 3D*, *ACS Nano* **11**, 10945–10954 (2017).
- [76] A. Ulvestad and A. Yau, *The self-healing of defects induced by the hydriding phase transformation in palladium nanoparticles*, *Nature Communications* **8**, 1–6 (2017).
- [77] N. Liu, M. L. Tang, M. Hentschel, H. Giessen, and A. P. Alivisatos, *Nanoantenna-enhanced gas sensing in a single tailored nanofocus*, *Nature Materials* **10**, 631–636 (2011).
- [78] A. Tittl et al., *Palladium-Based Plasmonic Perfect Absorber in the Visible Wavelength Range and Its Application to Hydrogen Sensing*, *Nano Letters* **11**, 4366–4369 (2011).
- [79] N. Strohfeltdt, J. Zhao, A. Tittl, and H. Giessen, *Sensitivity engineering in direct contact palladium-gold nano-sandwich hydrogen sensors*, *Optical Materials Express* **5**, 2525 (2015).

- [80] S. Bagheri et al., *Niobium as Alternative Material for Refractory and Active Plasmonics*, *ACS Photonics* **5**, 3298–3304 (2018).
- [81] X. Duan, S. Kamin, F. Sterl, H. Giessen, and N. Liu, *Hydrogen-Regulated Chiral Nanoplasmonics*, *Nano Letters* **16**, 1462–1466 (2016).
- [82] P. Li et al., *Reversible optical switching of highly confined phonon-polaritons with an ultrathin phase-change material*, *Nature Materials* **15**, 870–875 (2016).
- [83] F. A. A. Nugroho et al., *Metal-polymer hybrid nanomaterials for plasmonic ultrafast hydrogen detection*, *Nature Materials* **18**, 489–495 (2019).
- [84] D. Rodrigo et al., *Mid-infrared plasmonic biosensing with graphene*, *Science* **349**, 165–168 (2015).
- [85] C. Wu et al., *Fano-resonant asymmetric metamaterials for ultrasensitive spectroscopy and identification of molecular monolayers*, *Nature Materials* **11**, 69–75 (2012).
- [86] F. Neubrech et al., *Resonant plasmonic and vibrational coupling in a tailored nanoantenna for infrared detection*, *Physical Review Letters* **101**, 2–5 (2008).
- [87] L. Kühner et al., *Nanoantenna-Enhanced Infrared Spectroscopic Chemical Imaging*, *ACS Sensors* **2**, 655–662 (2017).
- [88] L. Kühner et al., *Vibrational Sensing Using Infrared Nanoantennas: Toward the Noninvasive Quantitation of Physiological Levels of Glucose and Fructose*, *ACS Sensors* **4**, 1973–1979 (2019).
- [89] R. Semenyshyn et al., *In Vitro Monitoring Conformational Changes of Polypeptide Monolayers Using Infrared Plasmonic Nanoantennas*, *Nano Letters* **19**, 1–7 (2019).
- [90] X. Duan and N. Liu, *Scanning plasmonic color display*, *ACS Nano* **12**, 8817–8823 (2018).
- [91] F. Neubrech, X. Duan, and N. Liu, *Dynamic plasmonic color generation enabled by functional materials*, *Science Advances* **6**, 1–21 (2020).
- [92] J. Park, S. J. Kim, P. Landreman, and M. L. Brongersma, *An Over-Coupled Phase-Change Metasurface for Efficient Reflection Phase Modulation*, *Advanced Optical Materials* **8**, 1–8 (2020).
- [93] J. Park, J. H. Kang, S. J. Kim, X. Liu, and M. L. Brongersma, *Dynamic reflection phase and polarization control in metasurfaces*, *Nano Letters* **17**, 407–413 (2017).

- [94] E. Herkert, F. Sterl, N. Strohfeldt, R. Walter, and H. Giessen, *Low-Cost Hydrogen Sensor in the ppm Range with Purely Optical Readout*, ACS Sensors **5**, 978–983 (2020).
- [95] F. Sterl et al., *Design Principles for Sensitivity Optimization in Plasmonic Hydrogen Sensors*, ACS Sensors **5**, 917–927 (2020).
- [96] E. Miliutina et al., *Fast and All-Optical Hydrogen Sensor Based on Gold-Coated Optical Fiber Functionalized with Metal-Organic Framework Layer*, ACS Sensors **4**, 3133–3140 (2019).
- [97] A. Baldi et al., *Elastic versus Alloying Effects in Mg-Based Hydride Films*, Physical Review Letters **121**, 255503 (2018).
- [98] V. Drechsler, J. Krauth, J. Karst, H. Giessen, and M. Hentschel, *Switchable Optical Nonlinearity at the Metal to Insulator Transition in Magnesium Thin Films*, ACS Photonics **7**, 1560–1568 (2020).
- [99] H. T. Uchida et al., *Absorption kinetics and hydride formation in magnesium films: Effect of driving force revisited*, Acta Materialia **85**, 279–289 (2015).
- [100] M. Hamm et al., *In situ observation of hydride nucleation and selective growth in magnesium thin-films with environmental transmission electron microscopy*, International Journal of Hydrogen Energy **44**, 32112–32123 (2019).
- [101] S. Wagner et al., *Structural Phase Transitions in Niobium Hydrogen Thin Films: Mechanical Stress, Phase Equilibria and Critical Temperatures*, ChemPhysChem **20**, 1890–1904 (2019).
- [102] J. N. Huijberts et al., *Yttrium and lanthanum hydride films with switchable optical properties*, Nature **380**, 231–234 (1996).
- [103] A. Lewis, M. Isaacson, A. Harootunian, and A. Muray, *Development of a 500 Å spatial resolution light microscope. I. light is efficiently transmitted through  $\lambda/16$  diameter apertures*, Ultramicroscopy **13**, 227–231 (1984).
- [104] D. W. Pohl, W. Denk, and M. Lanz, *Optical stethoscopy: Image recording with resolution  $\lambda/20$* , Applied Physics Letters **44**, 651–653 (1984).
- [105] J. Wessel, *Surface-enhanced optical microscopy*, Journal of the Optical Society of America B **2**, 1538–1541 (1985).

- [106] M. Specht, J. D. Pedarnig, W. M. Heckl, and T. W. Hänsch, *Scanning plasmon near-field microscope*, *Physical Review Letters* **68**, 476–479 (1992).
- [107] Y. Inouye and S. Kawata, *Near-field scanning optical microscope with a metallic probe tip*, *Optics Letters* **19**, 159 (1994).
- [108] J. Karst, N. Strohfeldt, M. Schäferling, H. Giessen, and M. Hentschel, *Single Plasmonic Oligomer Chiral Spectroscopy*, *Advanced Optical Materials* **6**, 1800087 (2018).
- [109] N. Strohfeldt, *Hydrogen in Metal Nanoparticles: Understanding and Applying Thermodynamic Properties of Metal-hydrogen Nanostructures*, PhD Thesis, University of Stuttgart, 2017.
- [110] R. Hillenbrand, T. Taubner, and F. Keilmann, *Phonon-enhanced light-matter interaction at the nanometre scale*, *Nature* **418**, 159–162 (2002).
- [111] F. Keilmann and R. Hillenbrand, *Near-field microscopy by elastic light scattering from a tip*, *Philosophical Transactions of the Royal Society A: Mathematical, Physical and Engineering Sciences* **362**, 787–805 (2004).
- [112] F. Zenhausern, Y. Martin, and H. K. Wickramasinghe, *Scanning interferometric apertureless microscopy: Optical imaging at 10 angstrom resolution*, *Science*, ( 1995).
- [113] R. Hillenbrand and F. Keilmann, *Complex optical constants on a subwavelength scale*, *Physical Review Letters* **85**, 3029–3032 (2000).
- [114] T. Taubner, R. Hillenbrand, and F. Keilmann, *Performance of visible and mid-infrared scattering-type near-field optical microscopes*, *Journal of Microscopy* **210**, 311–314 (2003).
- [115] R. Hillenbrand and F. Keilmann, *Optical oscillation modes of plasmon particles observed in direct space by phase-contrast near-field microscopy*, *Applied Physics B: Lasers and Optics* **73**, 239–243 (2001).
- [116] R. Hillenbrand, F. Keilmann, P. Hanarp, D. S. Sutherland, and J. Aizpurua, *Coherent imaging of nanoscale plasmon patterns with a carbon nanotube optical probe*, *Applied Physics Letters* **83**, 368–370 (2003).
- [117] A. Cvitkovic, N. Ocelic, and R. Hillenbrand, *Analytical model for quantitative prediction of material contrasts in scattering-type near-field optical microscopy*, *Optics Express* **15**, 8550 (2007).

- [118] B. Knoll and F. Keilmann, *Near-field probing of vibrational absorption for chemical microscopy*, *Nature* **399**, 134–137 (1999).
- [119] J. Gersten and A. Nitzan, *Electromagnetic theory of enhanced Raman scattering by molecules adsorbed on rough surfaces*, *The Journal of Chemical Physics* **73**, 3023–3037 (1980).
- [120] A. Wokaun, J. P. Gordon, and P. F. Liao, *Radiation damping in surface-enhanced Raman scattering*, *Physical Review Letters* **48**, 957–960 (1982).
- [121] P. K. Aravind and H. Metiu, *The effects of the interaction between resonances in the electromagnetic response of a sphere-plane structure; applications to surface enhanced spectroscopy*, *Surface Science* **124**, 506–528 (1983).
- [122] B. Knoll and F. Keilmann, *Enhanced dielectric contrast in scattering-type scanning near-field optical microscopy*, *Optics Communications* **182**, 321–328 (2000).
- [123] I. S. Averbukh, B. M. Chernobrod, O. A. Sedletsy, and Y. Prior, *Coherent near field optical microscopy*, *Optics Communications* **174**, 33–41 (2000).
- [124] J. L. Bohn, D. J. Nesbitt, and a. Gallagher, *Field enhancement in apertureless near-field scanning optical microscopy*. *Journal of the Optical Society of America. A, Optics, image science, and vision* **18**, 2998–3006 (2001).
- [125] J. Renger, S. Grafström, L. M. Eng, and R. Hillenbrand, *Resonant light scattering by near-field-induced phonon polaritons*, *Physical Review B - Condensed Matter and Materials Physics* **71**, 1–7 (2005).
- [126] A. Wokaun, *Surface enhancement of optical fields mechanism and applications*, *Molecular Physics* **56**, 1–33 (1985).
- [127] W. Denk, *Near-field optics: Microscopy with nanometer-size fields*, *Journal of Vacuum Science & Technology B: Microelectronics and Nanometer Structures* **9**, 510 (1991).
- [128] N. Calander and M. Willander, *Theory of surface-plasmon resonance optical-field enhancement at prolate spheroids*, *Journal of Applied Physics* **92**, 4878–4884 (2002).
- [129] J. Jackson, *Classical electrodynamics, Classical electrodynamics*, Wiley, 1998.

- [130] N. Ocelic, A. Huber, and R. Hillenbrand, *Pseudoheterodyne detection for background-free near-field spectroscopy*, Applied Physics Letters **89**, 2004–2007 (2006).
- [131] P. Patnaik, *A Comprehensive Guide to the Hazardous Properties of Chemical Substances*, John Wiley & Sons, 2006.
- [132] M. Cazzaniga, L. Caramella, N. Manini, and G. Onida, *Ab initio intraband contributions to the optical properties of metals*, Physical Review B - Condensed Matter and Materials Physics **82**, 1–7 (2010).
- [133] J. Isidorsson, I. A. M. E. Giebels, H. Arwin, and R. Griessen, *Optical properties of MgH<sub>2</sub> measured in situ in a novel gas cell for ellipsometry/spectrophotometry*, Physical Review B - Condensed Matter and Materials Physics **68**, 1–15 (2003).
- [134] X. Wang and L. Andrews, *Infrared spectra of magnesium hydride molecules, complexes, and solid magnesium dihydride*, Journal of Physical Chemistry A **108**, 11511–11520 (2004).
- [135] G. Bauer and W. Richter, *Optical Characterization of Epitaxial Semiconductor Layers, Optical characterization of epitaxial semiconductor layers*, Springer US, 1996.
- [136] M. Imada, A. Fujimori, and Y. Tokura, *Metal-insulator transitions*, Reviews of Modern Physics **70**, 1039–1263 (1998).
- [137] L. Mooij and B. Dam, *Hysteresis and the role of nucleation and growth in the hydrogenation of Mg nanolayers*, Physical Chemistry Chemical Physics **15**, 2782 (2013).
- [138] J. R. Ares et al., *Non-isothermal desorption process of hydrogenated nanocrystalline Pd-capped Mg films investigated by Ion Beam Techniques*, International Journal of Hydrogen Energy **39**, 2587–2596 (2014).
- [139] W. P. Kalisvaart et al., *Probing the Room Temperature Deuterium Absorption Kinetics in Nanoscale Magnesium Based Hydrogen Storage Multi layers Using Neutron Reflectometry, X-ray Diffraction, and Atomic Force Microscopy*, Journal of Physical Chemistry C **116**, 5868–5880 (2012).
- [140] C. Nishimura, M. Komaki, and M. Amano, *Hydrogen permeation through magnesium*, Journal of Alloys and Compounds **293**, 329–333 (1999).

- [141] H. T. Uchida, S. Wagner, A. Bell, and A. Pundt, *In-situ XRD measurement of nanocrystalline Magnesium films during hydrogen loading*, Photon Science Annual Reports, 2–3 (2011).
- [142] H. T. Uchida, R. Kirchheim, and A. Pundt, *Influence of hydrogen loading conditions on the blocking effect of nanocrystalline Mg films*, Scripta Materialia **64**, 935–937 (2011).
- [143] X. Duan, R. Griessen, R. J. Wijngaarden, S. Kamin, and N. Liu, *Self-recording and manipulation of fast long-range hydrogen diffusion in quasifree magnesium*, Physical Review Materials **2**, 085802 (2018).
- [144] K. Appusamy, S. Blair, A. Nahata, and S. Guruswamy, *Low-loss magnesium films for plasmonics*, Materials Science and Engineering B: Solid-State Materials for Advanced Technology **181**, 77–85 (2014).
- [145] P. Yu et al., *Dynamic Janus Metasurfaces in the Visible Spectral Region*, Nano Letters **18**, 4584–4589 (2018).
- [146] R. Griessen and R. Feenstra, *Volume changes during hydrogen absorption in metals*, Journal of Physics F: Metal Physics **15**, 1013–1019 (1985).
- [147] M. Hamm and A. Pundt, *FEM simulation supported evaluation of a hydrogen grain boundary diffusion coefficient in MgH<sub>2</sub>*, International Journal of Hydrogen Energy **42**, 22530–22537 (2017).
- [148] F. Sterl et al., *Nanoscale Hydrogenography on Single Magnesium Nanoparticles*, Nano Letters **18**, 4293–4302 (2018).
- [149] P. Hruška et al., *Structural studies of thin Mg films*, Journal of Physics: Conference Series **505**, (2014).
- [150] K. Appusamy et al., *Influence of aluminum content on plasmonic behavior of Mg-Al alloy thin films*, Optical Materials Express **6**, 3180 (2016).
- [151] R. Gremaud et al., *Hydrogenography: An optical combinatorial method to find new light-weight hydrogen-storage materials*, Advanced Materials **19**, 2813–2817 (2007).
- [152] J. J. Vajo, F. Mertens, C. C. Ahn, R. C. Bowman, and B. Fultz, *Altering hydrogen storage properties by hydride destabilization through alloy formation: LiH and MgH<sub>2</sub> destabilized with Si*, Journal of Physical Chemistry B **108**, 13977–13983 (2004).



- [153] S. Barcelo and S. S. Mao, *High throughput optical characterization of alloy hydrogenation*, International Journal of Hydrogen Energy **35**, 7228–7231 (2010).
- [154] J. Čermák and L. Král, *Hydrogen diffusion in Mg-H and Mg-Ni-H alloys*, Acta Materialia **56**, 2677–2686 (2008).
- [155] F. Zenhausern, M. P. O’Boyle, and H. K. Wickramasinghe, *Apertureless near-field optical microscope*, Applied Physics Letters **65**, 1623–1625 (1994).
- [156] A. Lahrech, R. Bachelot, P. Gleyzes, and A. C. Boccara, *Infrared-reflection-mode near-field microscopy using an apertureless probe with a resolution of  $\lambda/600$* , Optics Letters **21**, 1315–1317 (1996).
- [157] I. T. Lucas et al., *IR near-field spectroscopy and imaging of single  $\text{Li}_x\text{FePO}_4$  microcrystals*, Nano Letters **15**, 1–7 (2015).
- [158] K. Brinkert et al., *Efficient solar hydrogen generation in microgravity environment*, Nature Communications **9**, (2018).
- [159] A. Baldi, M. Gonzalez-Silveira, V. Palmisano, B. Dam, and R. Griessen, *Destabilization of the Mg-H system through elastic constraints*, Physical Review Letters **102**, 1–4 (2009).
- [160] A. Baldi et al., *Quasifree Mg-H thin films*, Applied Physics Letters **95**, 7–10 (2009).
- [161] A. Baldi et al., *Mg/Ti multilayers: Structural and hydrogen absorption properties*, Physical Review B - Condensed Matter and Materials Physics **81**, (2010).
- [162] L. Chen, C. Xu, X. F. Zhang, and T. Zhou, *Raman and infrared-active modes in MgO nanotubes*, Physica E: Low-Dimensional Systems and Nanostructures **41**, 852–855 (2009).
- [163] R. A. Buchanan, H. H. Caspers, and J. Murphy, *Lattice Vibration Spectra of Mg (OH) and Ca (OH)*, Applied Optics **2**, 1147–1150 (1963).
- [164] E. F. De Oliveira and Y. Hase, *Infrared study and isotopic effect of magnesium hydroxide*, Vibrational Spectroscopy **25**, 53–56 (2001).
- [165] T. Steinle, F. Mörz, A. Steinmann, and H. Giessen, *Ultra-stable high average power femtosecond laser system tunable from 133 to 20  $\mu\text{m}$* , Optics Letters **41**, 4863 (2016).

- [166] A. A. Govyadinov, I. Amenabar, F. Huth, P. Scott Carney, and R. Hillenbrand, *Quantitative measurement of local infrared absorption and dielectric function with tip-enhanced near-field microscopy*, *Journal of Physical Chemistry Letters* **4**, 1526–1531 (2013).
- [167] S. Amarie and F. Keilmann, *Broadband-infrared assessment of phonon resonance in scattering-type near-field microscopy*, *Physical Review B* **83**, (2011).
- [168] I. Amenabar et al., *Hyperspectral infrared nanoimaging of organic samples based on Fourier transform infrared nanospectroscopy*, *Nature Communications* **8**, (2017).
- [169] F. Huth et al., *Nano-FTIR Absorption Spectroscopy of Molecular Fingerprints at 20nm Spatial Resolution*, *Nano letters* **12**, 3973–3978 (2012).
- [170] E. D. Palik, *Handbook of optical constants of solids*. Academic press, 1998.
- [171] H. Y. Tien, M. Tanniru, C. Y. Wu, and F. Ebrahimi, *Effect of hydride nucleation rate on the hydrogen capacity of Mg*, *International Journal of Hydrogen Energy* **34**, 6343–6349 (2009).
- [172] K. Nörthemann and A. Pundt, *Double-locked nucleation and growth kinetics in nb-h thin films*, *Physical Review B* **83**, (2011).
- [173] P. Spatz, H. A. Aebischer, A. Krozer, and L. Schlapbach, *The Diffusion of H in Mg and the Nucleation and Growth of MgH<sub>2</sub> in Thin Films*, *Zeitschrift für Physikalische Chemie* **181**, 393–397 (1993).
- [174] F. Mooshammer et al., *Nanoscale Near-Field Tomography of Surface States on (Bi 0.5 Sb 0.5 ) 2 Te 3*, *Nano Letters* **18**, 7515–7523 (2018).
- [175] L. Jung et al., *Quantification of carrier density gradients along axially doped silicon nanowires using infrared nanoscopy*, *ACS Photonics* **6**, 1744–1754 (2019).
- [176] M. Besson and P. Gallezot, *Selective oxidation of alcohols and aldehydes on metal catalysts*, *Catalysis Today* **57**, 127–141 (2000).
- [177] R. H. Crabtree, *Homogeneous Transition Metal Catalysis of Acceptorless Dehydrogenative Alcohol Oxidation: Applications in Hydrogen Storage and to Heterocycle Synthesis*, *Chemical Reviews* **117**, 9228–9246 (2017).
- [178] J. Muzart, *Palladium-catalysed oxidation of primary and secondary alcohols*, *Tetrahedron* **59**, 5789–5816 (2003).

- [179] J. H. Kluytmans, A. P. Markusse, B. F. Kuster, G. B. Marin, and J. C. Schouten, *Engineering aspects of the aqueous noble metal catalysed alcohol oxidation*, *Catalysis Today* **57**, 143–155 (2000).
- [180] T. Weiss, N. A. Gippius, S. G. Tikhodeev, G. Granet, and H. Giessen, *Efficient calculation of the optical properties of stacked metamaterials with a Fourier modal method*, *Journal of Optics A: Pure and Applied Optics* **11**, 114019 (2009).
- [181] J. H. Weaver and C. G. Olson, *Optical absorption of hcp yttrium*, *Physical Review B* **15**, 590–594 (1977).
- [182] A. T. van Gogh et al., *Structural, electrical, and optical properties of La<sub>1-z</sub>Y<sub>z</sub>H<sub>x</sub> switchable mirrors*, *Physical Review B - Condensed Matter and Materials Physics* **63**, 1–21 (2001).
- [183] P. Ngene et al., *Seeing hydrogen in colors: Low-cost and highly sensitive eye readable hydrogen detectors*, *Advanced Functional Materials* **24**, 2374–2382 (2014).
- [184] E. S. Kooij, A. T. M. van Gogh, and R. Griessen, *In Situ Resistivity Measurements and Optical Transmission and Reflection Spectroscopy of Electrochemically Loaded Switchable YH<sub>x</sub> Films*, *Journal of The Electrochemical Society* **146**, 2990–2994 (1999).
- [185] P. Xin et al., *Revealing the Active Species for Aerobic Alcohol Oxidation by Using Uniform Supported Palladium Catalysts*, *Angewandte Chemie* **130**, 4732–4736 (2018).
- [186] G. Bour, A. Reinholdt, A. Stepanov, C. Keutgen, and U. Kreibig, *Optical and electrical properties of hydrogenated yttrium nanoparticles*, *European Physical Journal D* **8**, 219–223 (2001).
- [187] A. L. Stepanov et al., *Synthesis of yttrium clusters*, *Vacuum* **64**, 9–14 (2001).
- [188] M. Dornheim et al., *Stress development in thin yttrium films on hard substrates during hydrogen loading*, *Journal of Applied Physics* **93**, 8958–8965 (2003).
- [189] R. Gremaud et al., *Hydrogenography of MgyNi<sub>1-y</sub>H<sub>x</sub> gradient thin films: Interplay between the thermodynamics and kinetics of hydrogenation*, *Acta Materialia* **58**, 658–668 (2010).
- [190] Y. Zhao, M. Belkin, and A. Alù, *Twisted optical metamaterials for planarized ultrathin broadband circular polarizers*, *Nature Communications* **3**, 1877 (2012).

- [191] J. Kaschke, J. K. Gansel, and M. Wegener, *On metamaterial circular polarizers based on metal N-helices*, *Optics Express* **20**, 26012 (2012).
- [192] J. K. Gansel et al., *Gold Helix Photonic Metamaterial as Broadband Circular Polarizer*, *Science* **325**, 1513–1515 (2009).
- [193] J. K. Gansel et al., *Tapered gold-helix metamaterials as improved circular polarizers*, *Applied Physics Letters* **100**, 2010–2013 (2012).
- [194] J. Kaschke et al., *A Helical Metamaterial for Broadband Circular Polarization Conversion*, *Advanced Optical Materials* **3**, 1411–1417 (2015).
- [195] K. W. Smith et al., *Exploiting Evanescent Field Polarization for Giant Chiroptical Modulation from Achiral Gold Half-Rings*, *ACS Nano* **12**, 11657–11663 (2018).
- [196] M. L. Nesterov, X. Yin, M. Schäferling, H. Giessen, and T. Weiss, *The Role of Plasmon-Generated Near Fields for Enhanced Circular Dichroism Spectroscopy*, *ACS Photonics* **3**, 578–583 (2016).
- [197] J. García-Guirado, M. Svedendahl, J. Puigdollers, and R. Quidant, *Enantiomer-Selective Molecular Sensing Using Racemic Nanoplasmonic Arrays*, *Nano Letters* **18**, 6279–6285 (2018).
- [198] R. Quidant and M. Kreuzer, *Biosensing: Plasmons offer a helping hand*, *Nature Nanotechnology* **5**, 762–763 (2010).
- [199] K. M. McPeak et al., *Ultraviolet Plasmonic Chirality from Colloidal Aluminum Nanoparticles Exhibiting Charge-Selective Protein Detection*, *Advanced Materials* **27**, 6244–6250 (2015).
- [200] N. Liu, M. Hentschel, T. Weiss, A. P. Alivisatos, and H. Giessen, *Three-dimensional plasmon rulers*, *Science* **332**, 1407–1410 (2011).
- [201] V. E. Ferry, J. M. Smith, and A. P. Alivisatos, *Symmetry Breaking in Tetrahedral Chiral Plasmonic Nanoparticle Assemblies*, *ACS Photonics* **1**, 1189–1196 (2014).
- [202] R. Schreiber et al., *Chiral plasmonic DNA nanostructures with switchable circular dichroism*, *Nature Communications* **4**, 3948 (2013).
- [203] A. Kuzyk et al., *Reconfigurable 3D plasmonic metamolecules*, *Nature Materials* **13**, 862–866 (2014).

- [204] A. Kuzyk, M. J. Urban, A. Idili, F. Ricci, and N. Liu, *Selective control of reconfigurable chiral plasmonic metamolecules*, *Science Advances* **3**, 1–6 (2017).
- [205] M. J. Urban et al., *Plasmonic toroidal metamolecules assembled by DNA origami*, *Journal of the American Chemical Society* **138**, 5495–5498 (2016).
- [206] N. Li et al., *DNA-assembled bimetallic plasmonic nanosensors*, *Light: Science & Applications* **3**, e226–e226 (2014).
- [207] E. Plum et al., *Metamaterial with negative index due to chirality*, *Physical Review B - Condensed Matter and Materials Physics* **79**, 1–6 (2009).
- [208] E. Plum et al., *Metamaterials: Optical activity without chirality*, *Physical Review Letters* **102**, 1–4 (2009).
- [209] Y. Tang and A. E. Cohen, *Optical chirality and its interaction with matter*, *Physical Review Letters* **104**, 1–4 (2010).
- [210] Z. Fan and A. O. Govorov, *Plasmonic circular dichroism of chiral metal nanoparticle assemblies*, *Nano Letters* **10**, 2580–2587 (2010).
- [211] L. Hu et al., *Long-range Plasmon-Assisted Chiral Interactions in Nanocrystal Assemblies*, *ACS Photonics* **6**, 749 (2019).
- [212] Y. Tang, L. Sun, and A. E. Cohen, *Chiroptical hot spots in twisted nanowire plasmonic oscillators*, *Applied Physics Letters* **102**, (2013).
- [213] L. V. Poulikakos et al., *Optical Chirality Flux as a Useful Far-Field Probe of Chiral Near Fields*, *ACS Photonics* **3**, 1619–1625 (2016).
- [214] L. V. Poulikakos, P. Thureja, A. Stollmann, E. De Leo, and D. J. Norris, *Chiral Light Design and Detection Inspired by Optical Antenna Theory*, *Nano Letters* **18**, 4633–4640 (2018).
- [215] K. M. McPeak et al., *Complex chiral colloids and surfaces via high-index off-cut silicon*, *Nano Letters* **14**, 2934–2940 (2014).
- [216] V. K. Valev, J. J. Baumberg, C. Sibilia, and T. Verbiest, *Chirality and chiroptical effects in plasmonic nanostructures: Fundamentals, recent progress, and outlook*, *Advanced Materials* **25**, 2517–2534 (2013).
- [217] M. Hentschel, M. Schäferling, X. Duan, H. Giessen, and N. Liu, *Chiral plasmonics*, *Science Advances* **3**, e1602735 (2017).

- [218] B. Frank et al., *Large-area 3D chiral plasmonic structures*, *ACS Nano* **7**, 6321–6329 (2013).
- [219] A. G. Mark, J. G. Gibbs, T. C. Lee, and P. Fischer, *Hybrid nanocolloids with programmed three-dimensional shape and material composition*, *Nature Materials* **12**, 802–807 (2013).
- [220] J. G. Gibbs, A. G. Mark, S. Eslami, and P. Fischer, *Plasmonic nanohelix metamaterials with tailorable giant circular dichroism*, *Applied Physics Letters* **103**, 98–102 (2013).
- [221] C. Song et al., *Tailorable plasmonic circular dichroism properties of helical nanoparticle superstructures*, *Nano Letters* **13**, 3256–3261 (2013).
- [222] A. Kuzyk et al., *DNA-based self-assembly of chiral plasmonic nanostructures with tailored optical response*, *Nature* **483**, 311–314 (2012).
- [223] B. Hopkins, A. N. Poddubny, A. E. Miroshnichenko, and Y. S. Kivshar, *Circular dichroism induced by Fano resonances in planar chiral oligomers*, *Laser and Photonics Reviews* **10**, 137–146 (2016).
- [224] M. Hentschel, M. Schäferling, T. Weiss, N. Liu, and H. Giessen, *Three-dimensional chiral plasmonic oligomers*, *Nano Letters* **12**, 2542–2547 (2012).
- [225] M. Hentschel, V. E. Ferry, and A. P. Alivisatos, *Optical Rotation Reversal in the Optical Response of Chiral Plasmonic Nanosystems: The Role of Plasmon Hybridization*, *ACS Photonics* **2**, 1253–1259 (2015).
- [226] N. Liu et al., *Three-dimensional photonic metamaterials at optical frequencies*, *Nature Materials* **7**, 31–37 (2008).
- [227] V. E. Ferry, M. Hentschel, and A. P. Alivisatos, *Circular Dichroism in Off-Resonantly Coupled Plasmonic Nanosystems*, *Nano Letters* **15**, 8336–8341 (2015).
- [228] H.-E. Lee et al., *Amino-acid- and peptide-directed synthesis of chiral plasmonic gold nanoparticles*, *Nature* **556**, 360–365 (2018).
- [229] N. H. Cho et al., *Cysteine Induced Chiral Morphology in Palladium Nanoparticle*, *Particle and Particle Systems Characterization* **1900062**, 1–5 (2019).
- [230] H.-E. Lee et al., *Identifying peptide sequences that can control the assembly of gold nanostructures*, *Molecular Systems Design & Engineering* **3**, 581 (2018).

- [231] J. Sachs, J. P. Günther, A. G. Mark, and P. Fischer, *Chiroptical spectroscopy of a freely diffusing single nanoparticle*, *Nature Communications* **11**, 1–7 (2020).
- [232] K. W. Smith et al., *Chiral and Achiral Nanodumbbell Dimers: The Effect of Geometry on Plasmonic Properties*, *ACS Nano* **10**, 6180–6188 (2016).
- [233] P. Banzer, P. Wozniak, U. Mick, I. De Leon, and R. W. Boyd, *Chiral optical response of planar and symmetric nanotrimers enabled by heteromaterial selection*, *Nature Communications* **7**, 13117 (2016).
- [234] L. Y. Wang et al., *Circular Differential Scattering of Single Chiral Self-Assembled Gold Nanorod Dimers*, *ACS Photonics* **2**, 1602–1610 (2015).
- [235] W. Ma et al., *Chiral plasmonics of self-assembled nanorod dimers*. *Scientific reports* **3**, 1934 (2013).
- [236] L. S. Slaughter et al., *Single-particle spectroscopy of gold nanorods beyond the quasi-static limit: Varying the width at constant aspect ratio*, *Journal of Physical Chemistry C* **114**, 4934–4938 (2010).
- [237] N. H. Cho et al., *Uniform Chiral Gap Synthesis for High Dissymmetry Factor in Single Plasmonic Gold Nanoparticle*, *ACS Nano* **14**, 3595–3602 (2020).





## CURRICULUM VITAE

---

### Julian Philipp Karst

born October 28, 1992 in Stuttgart (Germany)

E-MAIL julian-karst@outlook.com

PHONE +49 171 1469026

#### ACADEMIC EDUCATION

- SINCE 2019 **PhD Candidate Physics | University of Stuttgart | Germany**  
Group of Prof. Dr. Harald Giessen  
Title: *Functional & active plasmonic systems and metasurfaces*
- 2015 - 2018 **M.Sc. Physics | University of Stuttgart | Germany**  
Focus subject: Advanced optics  
Thesis: *Magnesium thin film crystallinity and nanoscale hydrogenography*
- 2012 - 2015 **B.Sc. Physics | University of Stuttgart | Germany**  
Thesis: *Circular dichroism spectroscopy on individual plasmonic nanoparticles*
- 2003 - 2012 **Secondary School | FPGZ Zuffenhausen | Germany**  
Focus subjects: Physics, Music  
Optional course: Natural sciences and technology

#### WORK AND PROFESSIONAL EXPERIENCE

- SINCE 04/2017 **Research Scientist | University of Stuttgart | Germany**  
4th Physics Institute and Research Center SCoPE with Prof. Dr. Harald Giessen
- 10/2018 **Visiting Researcher | ETH Zuerich | Switzerland**  
Group of Prof. Dr. David Norris
- 09/2016 -  
02/2017 **Intern | TRUMPF Photonics Inc. | Cranbury | USA**  
Technology development of high-power diode lasers and automated data analysis
- 03/2015 -  
09/2015 **Student Researcher | MPI Intellig. Systems | Stuttgart | Germany**  
Research with Prof. Dr. Laura Na Liu (collaboration)

- 12/2013 - **Student Researcher | University of Stuttgart | Germany**  
08/2016 4th Physics Institute and Research Center SCoPE with Prof. Dr. Harald Giessen
- 04/2012 **Intern | MPI Solid State Research | Stuttgart | Germany**  
Stuttgart Center for Electron Microscopy with Prof. Dr. Peter A. van Aken

## TEACHING

- SINCE 04/2017 **Supervision of B.Sc. and M.Sc. Thesis Projects**  
Supervising independent research projects in field of physics and photonic engineering.
- 04/2019 - **Organizer and Tutor Advanced Practical Course "Nonlinear Optics"**  
04/2022 For graduate (M.Sc.) students of major physics and photonic engineering.
- 10/2019 - **Tutor for Experimental Physics III - Optics**  
03/2020 Teaching fundamental and advanced optics.

## ACKNOWLEDGMENTS

---

The realization of this thesis would not have been possible without the help of several people inside and outside the PI4.

I would especially like to thank:

- Prof. Dr. Harald Giessen for giving me the opportunity to work on my PhD thesis at the 4th Physics Institute. I thank you for all your support throughout my entire time at the PI4 and for making it possible to work on such exciting projects.
- Prof. Dr. Laura Na Liu and Prof. Dr. Thomas Zentgraf for being my co-examiners.
- Prof. Dr. Maria Daghofer for being the head of my examination committee.
- Dr. Mario Hentschel for all your support, help, and fruitful discussions as well as for being a good friend throughout all my years at the PI4. I benefited a lot from all your theoretical knowledge and skills in nanofabrication.
- Dr. Christine von Rekowski for being a great help with all my administrative matters and being the place to go for everything concerning university.
- Lucca Kühner for all the motivating discussions and for being my best friend.
- Moritz Flöss for being a great colleague and friend as well as for all the fruitful discussions and good laughs in the lab or after work.
- Moni Ubl (aka "Ubl") and Philipp Flad for their great support in the MSL.
- Dr. Florian Sterl and Dr. Nik Strohfeldt for being great colleagues and supervisors during earlier days at the PI4.
- Dominik Ludescher and Dr. Yohan Lee for a short but fun time during our shared projects (although they were quite frustrating sometimes).
- Annika Neubauer for being a great office mate.
- All my colleagues at PI4, who made the last years not only incredibly interesting but also incredibly fun.

Furthermore, I want to thank all my friends outside the institute distracting me from my everyday life working on my PhD thesis. My deepest thanks go to my mother, my fiancée Anna, and to my entire family. Without your support, encouragement, and patience this thesis would not have been possible.